Applications of NODDI for imaging in vivo white matter pathology in neurodegenerative diseases

Jiaying Zhang

A dissertation submitted in partial fulfillment

of the requirements for the degree of

Doctor of Philosophy

of

University College London.

Department of Computer Science & Centre for medical image computing

University College London

Feburary 2019

I, Jiaying Zhang, confirm that the work presented in this thesis is my own. Where information has been derived from other sources, I confirm that this has been indicated in the work.

Abstract

This thesis aims to evaluate: 1) the feasibility of advanced diffusion Magnetic Resonance Imaging (MRI) technique − Neurite orientation dispersion and density imaging (NODDI) for providing *in vivo* imaging evidence of white matter (WM) pathology at both preclinical and clinical stages of neurodegenerative diseases; 2) the added value of this advanced technique - NODDI over the standard diffusion MRI technique - Diffusion Tensor Imaging (DTI).

Monitoring WM pathology is vital in coping with this challenge brought by neurodegenerative diseases as abnormal axonal transport has been identified in neurodegenerative diseases. *In vivo* imaging evidence using DTI suggests that patients with neurodegenerative diseases have abnormal WM microstructure compared to normal controls. Whilst sensitive, DTI metrics lack tissue specificity to biological features due to the simplicity of the model, therefore could not inform more on the disease pathology. In contrast, NODDI could provide biologically meaningful metrics that have been validated with histological measures in human neural tissue. Therefore, investigating the potential of NODDI in clinical studies of neurodegenerative diseases could greatly increase our knowledge and benefit our understanding of the disease pathology.

In this thesis, we chose pre-manifest Huntington′s disease and young onset Alzheimer′s disease as the disease models to represent the preclinical and clinical stages respectively. We demonstrated the feasibility of NODDI in not only detecting WM abnormalities at both preclinical and clinical stages of neurodegenerative diseases but also tracking the longitudinal progression of WM microstructural deficits at the clinical stage. We also demonstrated the clinical relevance of NODDI by

evaluating the correlations between the clinical assessments and NODDI metrics. Compared with DTI, we found that NODDI could provide more information on disease-specific WM pathology.

Impact Statement

Neurodegenerative diseases have become a global challenge for healthcare. Recent advances in medical imaging techniques, especially MRI, enable us to broaden and deepen our understanding of the pathology in neurodegenerative diseases.

During my PhD, together with my collaborators, I have designed a series of experiments to evaluate the translational feasibility of an advanced quantitative MRI technique - NODDI on revealing a detailed picture of the *in vivo* white matter pathology in neurodegenerative diseases. These studies, for the first time, have not only demonstrated that this technique is viable for clinical studies on neurodegeneration, but also provided evidence on its added value over the standard clinical technique - DTI. My work could strengthen the connections between the imaging scientists and the clinicians, and inspire more collaborations between these two communities to enlarge our knowledge of the disease pathology. The deep understanding of the disease pathology could benefit the whole society in future as it could aid in developing effective therapeutic plans to delay or prevent the disease onset in neurodegenerative diseases.

So far, I have presented all these studies to both the communities of clinicians and imaging scientists at international conferences - AAIC and ISMRM. All of my presentations were well received and had drew a lot of attention. Especially, my abstract on young onset AD study was selected as a top 5% abstract at ISMRM in 2016. Moreover, my work on comparisons of model fitting procedures - using AMICO and original NODDI toolbox using HCP lifespan data was selected as a talk at the biggest international conference on MRI - ISMRM in 2016.

Moreover, I have published both cross-sectional studies on high-impact jour-

nals, pre-manifest HD study on Annals of Neurology (ranking 8 out of 197 journals on clinical neurology) earlier this year and young onset AD study on Neurobiology of Aging (ranking 22 out of 197 journals on clinical neurology) last year. Since the publication of our young onset AD paper, it has already been cited for 9 times according to the counts on google scholar.

My work on the longitudinal progression of white matter pathology in young onset AD patients was discussed in the panel meeting of the biggest global study on AD - ADNI, and they decided to include the multi-shell diffusion MRI scan for NODDI analysis in future at their 3rd time visit.

My work on the characterisation of the in vivo white matter pathology in pre-manifest HD subjects has been presented in HD-specific seminars at UCL, and also have supported the successful funding application of an exciting study “Treat-HD: targeting neurodegeneration in Huntington’s disease”.

Publications

Journal papers (* joint first-author)

- **Zhang J***, Gregory S*, Scahill RI, Durr A, Thomas DL, Lehericy S, et al. In vivo characterization of white matter pathology in pre-manifest Huntington′s disease. Ann Neurol. 2018 (* joint 1st author).

- Parker TD, Slattery CF, **Zhang J**, Nicholas JM, Paterson RW, Foulkes AJM, et al. Cortical microstructure in young onset Alzheimer′s disease using neurite orientation dispersion and density imaging. Hum Brain Mapp. 2018.

- Slattery CF*, **Zhang J***, Paterson RW, Foulkes AJM, Carton A, Macpherson K, et al. ApoE influences regional white-matter axonal density loss in Alzheimer′s disease. Neurobiol Aging. 2017 (* joint 1st author).

- Alexander DC, Zikic D, Ghosh A, Tanno R, Wottschel V, **Zhang J**, et al. Image quality transfer and applications in diffusion MRI. NeuroImage. 2017.

- Gregory S, Scahill RI, Seunarine KK, Stopford C, Zhang H, **Zhang J**, et al. Neuropsychiatry and White Matter Microstructure in Huntington′ Disease. Journal of Huntington′s Disease. 2015.

Conference abstracts and papers

- Wen J, Zhang H, Alexander D, Durrleman S, Routier A, Rinaldi D, Houot M, **Zhang J**, et al., NODDI highlights promising new markers in presymptomatic C9orf72 Carriers, The organization of human brain mapping, 2018

- **Zhang J**, Slattery CF, Paterson RW, Foulkes AJM, Carton A, Macpherson K, et al. Longitudinal progression of white matter deficits in Young Onset Alzheimer's Disease and Its Syndromic Variants using NODDI, International Society for Magnetic Resonance in Medicine, 2017

- **Zhang J**, The lifespan trajectory of white matter microstructure detected by NODDI, International Society for Magnetic Resonance in Medicine, 2016 (Talk)

- **Zhang J**, Slattery CF, Paterson RW, Foulkes AJM, Carton A, Macpherson K, et al. Neurite Orientation Dispersion and Density Imaging (NODDI) in Young Onset Alzheimer's Disease and Its Syndromic Variants, International Society for Magnetic Resonance in Medicine, 2016 (Talk)

- **Zhang J**, Gregory S, Scahill RI, Durr A, Thomas DL, Lehericy S, et al. Reduced Neurite Density in Pre-manifest Huntington?s Disease Population detected by NODDI, International Society for Magnetic Resonance in Medicine, 2015

- Alexander DC, Zikic D, Ghosh A, Tanno R, Wottschel V, **Zhang J**, et al. Image quality transfer via random forest regression: Applications in diffusion MRI. The international conference on medical image computing and computer-assisted intervention, 2014

Journal papers in preparations

- **Zhang J**, Slattery CF, Paterson RW, Foulkes AJM, Carton A, Macpherson K, et al. Longitudinal progression of in-vivo white matter pathology in Young onset Alzheimer′s disease

Acknowledgements

The last few years have been a real challenge for me. I am just so happy that it is coming to an end. And it is time for me to express my sincere gratitude to all the people who have helped me survive.

First, I would like to thank my supervisors - Dr. Gary Hui Zhang and Prof. Daniel Alexander for their advice and support. I am also thankful to my advisors from the clinical side - Prof. Sarah Tabrizi and Dr. Jonathan Schott for their invaluable advice on all my work.

I am also thankful to my collaborators from the Huntington's disease research group in both queen square at UCL and hospitals in Paris as well as the young onset AD research team in the dementia research centre at UCL, especially to Dr. Sarah Gregory, Dr. Rachael Scahill, Prof. Geraint Ress, Dr. David Thomas, Dr. Catherine Slattery, and Prof. Nick Fox (the order of the list does not mean anything :)).

I am very grateful to the funding bodies and all the participants. Without them, none of the studies would have happened.

I would like to thank my examiners - professor Claudia Wheeler-Kingshott and professor Mara Cercignani for their thoughtful suggestions on my thesis.

I am also grateful to the reviewers of my papers for their thoughtful comments and their help with improving the quality of these papers.

I also would like to say thanks to all my friends in and outside my research life. Words are certainly never enough to express my gratitude. You are all so lovely and so dear to me. Without you, I would have run away from my PhD a long time ago.

I also would like to give many thanks to the perinatal brain injury group at St Thomas's Hospital in KCL. I am very grateful that you have given me a chance to

work in a challenging project. I am very touched by all your support and trust.

A special thanks goes to both families of Shrestha and Kakkar for your unconditional support when I was so lost. In the last few years, I have had so many laughs and amazing memories as well as great food together with you guys. You will always have a special place in my heart.

Finally, I am in debt to my family, especially my dear grandfather, my dear mum and my dear dad. Your love makes me a better person. I am also thankful to my brother and his wife for all their support whenever I am down. I am also very grateful for my cousin brother Mr. Lianpu Ding, for his support and encouragements, and for him to have my back all the time.

I would like to end this acknowledgement with one of my favourite poems by Mr. Aleksandr Pushkin.

If by life you were deceived,
Don't be dismal, don't be wild.
In the day of grief, be mild.
Merry days will come, believe.
Heart is living in tomorrow.
Present is dejected here.
In a moment, passes sorrow.
That which passes will be dear.

Contents

1 MOTIVATION **25**

1.1 The context 25

1.2 Problem statement 27

1.3 Aims of PhD projects 28

1.4 Structure of the thesis 28

2 Diffusion Magnetic Resonance Imaging **31**

2.1 Water Diffusion 31

2.1.1 Molecular diffusion and Einstein equation 31

2.1.2 Water diffusion probes the brain microstructure non-invasively 32

2.1.3 Water diffusion in the brain 32

2.2 Measuring water diffusion in the tissue using MRI 34

2.2.1 Introduction to MRI 34

2.2.1.1 Basics of nuclear magnetic resonance 34

2.2.1.2 Manipulating the system to detect the net magnetization 35

2.2.1.3 MR image formation 36

2.2.1.4 MRI pulse sequences 37

2.2.2 Encoding diffusion using MRI 42

2.2.2.1 Measuring water diffusion using MRI 42

2.2.2.2 Artifacts and distortions in diffusion MR images . 44

2.3 Inferring white matter microstructural configurations using diffusion MRI 46
2.3.1 Diffusion tensor imaging (DTI) 49
2.3.1.1 Mathematical descriptions of DTI 49
2.3.1.2 Tensor fitting 50
2.3.1.3 Computing DTI metrics 50
2.3.2 Neurite orientation dispersion and density imaging (NODDI) 51
2.3.2.1 Mathematical descriptions of NODDI 51
2.3.2.2 NODDI fitting 53
2.3.2.3 NODDI metrics 54
2.4 Diffusion MR Image Analysis 55
2.4.1 Voxel-based analysis 55
2.4.2 Tract-based spatial statistics (TBSS) 56
2.4.3 Tractography 57
2.4.4 ROI analysis 58

3 White matter in neurodegenerative diseases: An overview 61
3.1 White matter in the human brain 61
3.1.1 White matter microstructure 61
3.1.1.1 Axons 61
3.1.1.2 The intra-axonal space 63
3.1.1.3 Myelin 63
3.1.1.4 Glial cells 63
3.1.1.5 Extra-cellular space 64
3.1.1.6 Vascular system 64
3.1.2 White matter tracts 64
3.1.2.1 Commissural fibers 64
3.1.2.2 Association fibers 64
3.1.2.3 Projection fibers 65
3.2 White matter pathology in neurodegenerative diseases 65
3.2.1 Neurodegenerative diseases 65

3.2.1.1 Huntington′s disease 66
3.2.1.2 Young onset Alzheimer′s disease 67
3.2.2 White matter pathology in neurodegenerative diseases . . . 68
3.2.3 Diffusion MRI in studying the white matter abnormalities in neurodegenerative diseases 69

4 Image acquisition, preprocessing, image analysis in a clinical study using diffusion MRI 71
4.1 Image acquisition 71
4.1.1 Protocol design 71
4.1.2 Pre-testing MRI scans 73
4.2 Image processing 74
4.2.1 Quality control 74
4.2.2 Motion and eddy-current distortion correction 75
4.2.3 Eliminating the non-brain tissue 76
4.2.4 Model fitting 77
4.2.5 Spatial normalisation 77
4.2.6 Quantitative analysis 79

5 NODDI in the pre-manifest stage of Huntington′s Disease 81
5.1 Introduction 81
5.2 Research dissemination 83
5.3 Methods 84
5.3.1 Participants 84
5.3.2 Diffusion MR image acquisition 84
5.3.2.1 The NODDI acquisition 84
5.3.2.2 The DTI acquisition 84
5.3.3 Preparations of NODDI and DTI metric maps 85
5.3.4 Statistical analysis 85
5.3.4.1 The general linear model for group comparison . 85
5.3.4.2 TBSS Analysis 85

5.3.4.3 ROI Analysis 86
5.4 Results 87
5.4.1 Demographics, Number of CAG Repeats and Clinical Scores of HD Disease Progression 87
5.4.2 Group differences detected by NODDI using TBSS analysis 88
5.4.3 Group differences detected by DTI using TBSS analysis . . 89
5.4.4 Group differences detected by NODDI using ROI analysis . 90
5.4.5 Correlations between clinical scores of disease progression and NODDI metrics in selected white matter ROIs 92
5.4.6 The estimated sample sizes for selected ROIs using NODDI 92
5.5 Discussion 93
5.6 Conclusions 98

6 NODDI in young onset Alzheimer's disease 101
6.1 Introduction 101
6.2 Research dissemination 103
6.3 Methods 103
6.3.1 Participants 103
6.3.2 Assessing APOE $\varepsilon 4$ genotype 104
6.3.3 Diffusion MR image acquisition 104
6.3.3.1 The NODDI acquisition 104
6.3.3.2 The DTI acquisition 105
6.3.4 Preparations of NODDI and DTI metric maps 105
6.3.5 Statistical analysis 105
6.3.5.1 The statistics of clinical characteristics and neuropsychology scores 105
6.3.5.2 The general linear model for group comparison . 106
6.3.5.3 TBSS Analysis 106
6.3.5.4 ROI Analysis 107
6.4 Results 107
6.4.1 Demographics, genetic and clinical characteristics 107

6.4.2 Neuropsychological profiles 108
6.4.3 Whole brain white matter microstructural damage in YOAD 108
6.4.3.1 Group differences detected by NODDI using TBSS analysis 108
6.4.3.2 Group differences detected by DTI using TBSS analysis 108
6.4.4 White matter microstructural damage in YOAD with different APOE ε4 genotypes 109
6.4.4.1 Group differences detected by NODDI using TBSS analysis 109
6.4.4.2 Group differences detected by DTI using TBSS analysis 109
6.4.5 ROI analysis with NODDI metrics 110
6.4.5.1 Group differences in NODDI metrics of ROIs on the white matter skeleton 110
6.4.5.2 The correlations between NODDI metrics and cognitive function in patients 110
6.5 Discussion 110
6.6 Conclusion 113

7 NODDI in longitudinal young onset AD 127
7.1 Introduction 127
7.2 Research dissemination 129
7.3 Methods 129
7.3.1 Participants 129
7.3.2 Assessing APOE ε4 genotype 130
7.3.3 MRI acquisition 130
7.3.4 Preparations of NODDI metric maps 130
7.3.5 Statistical analysis 130
7.3.5.1 The statistics of clinical characteristics 130
7.3.5.2 The general linear model for group comparison . 131

7.3.5.3 TBSS analysis 131
7.4 Results 132
7.4.1 Demographic 132
7.4.2 Group differences between YOAD patients and controls . . 132
7.4.3 Group differences between YOAD genotypes and controls . 135
7.5 Discussion 136
7.6 Conclusion 138

8 Conclusions and Discussions **145**
8.1 The summary 145
8.2 Discussions and future work 147
8.2.1 Image quality control 147
8.2.2 The potential confounding impact of motion 147
8.2.3 Strategies for correcting eddy-current distortion and motion 148
8.2.4 Strategies for NODDI fitting 148
8.2.5 The time-dependence of NODDI metrics 151
8.2.6 The limitations of NODDI model 152
8.2.7 The reproducibility of NODDI metrics 152

Bibliography **153**

List of Figures

2.1 Water diffusion in the brain 33

2.2 The framework of single echo PGSE sequence 39

2.3 An example of Fourier transform between k space and image space . 40

2.4 Common k-space sampling trajectories. A The cartesian scheme; B The radial scheme; C The spiral scheme. 41

2.5 Echo Planar Imaging in k space. A single shot k-space trajectory; B multi-shot k-space trajectory 42

2.6 The scheme framework of pulse gradient spin echo sequence 43

2.7 An example of signal dropout in multiple slices in DW images . . . 44

2.8 An example of EPI distortion 45

2.9 An example of chemical shifting in the brain 46

2.10 Microstructure imaging using diffusion MRI. Illustration adapted from previous work [14, 48] 47

2.11 An illustration of the single tensor model in DTI 50

2.12 An illustration of NODDI model 52

2.13 Popular image analysis methods in diffusion MRI. Figure B and C were adapted from Lebel et al., 2008 [112] 55

3.1 An illustration of the microstructure in a voxel of human brain white matter from a view of MR imaging. Elements were adapted from [136] and [137] 62

3.2 The clinical history of Huntington′s disease (adapted from [167]) . . 67

3.3 The clinical history of Alzheimer′s disease (adapted from [189]) . . 68

4.1 The flowchart of the steps in an imaging study 72

4.2 An illustration of the image processing pipeline 74

4.3 The flowchart of spatial normalisation using DTI-TK. A. Constructing the study-specific tensor template for cross-sectional studies; B. Constructing the study-specific tensor template for longitudinal studies. 78

5.1 White matter ROIs defined in the ICBM-81 white matter atlas. A. Genu of the corpus callosum; B. Body of the corpus callosum; C. Splenium of the corpus callosum; D. Anterior limb of the internal capsule; E. The posterior limb of the internal capsule; F. The external capsule. 86

5.2 Whole brain white matter abnormalities in pre-manifest HD detected by NDI using TBSS, TFCE corrected, $p<0.05$ 88

5.3 Whole brain white matter abnormalities in pre-manifest HD detected by ODI using TBSS, TFCE corrected, $p<0.05$ 89

5.4 Whole brain white matter abnormalities in pre-manifest HD detected by NDI using TBSS, TFCE corrected, $p<0.01$ 90

5.5 Whole brain white matter abnormalities in pre-manifest HD detected by FA using TBSS, TFCE corrected, $p<0.05$ 91

5.6 Whole brain white matter abnormalities in pre-manifest HD detected by MD using TBSS, TFCE corrected, $p<0.05$ 92

5.7 Whole brain white matter abnormalities in pre-manifest HD detected by AxD using TBSS, TFCE corrected, $p<0.05$ 93

5.8 Whole brain white matter abnormalities in pre-manifest HD detected by RD using TBSS, TFCE corrected, $p<0.05$ 94

5.9 Correlations between clinical scores of disease progression and NODDI metrics 94

6.1 The 4 quadrant ROIs we defined on the white matter skeleton. . . . 106

6.2 Group differences in NODDI metrics between YOAD and controls on the white matter skeleton, tfce corrected p<0.05. A. NDI; B. ODI; C. FISO. 115

6.3 Group differences in DTI metrics between YOAD and controls on the white matter skeleton, tfce corrected p<0.05. A. FA; B. MD; C. AD; D. RD. 116

6.4 Group differences in NDI between YOAD genotypes and controls on the white matter skeleton, tfce corrected p<0.05. A. APOE ε4-; B. APOE ε4+. 117

6.5 Group differences in ODI between YOAD genotypes and controls on the white matter skeleton, tfce corrected p<0.05. A. APOE ε4-; B. APOE ε4+. 118

6.6 Group differences in FISO between YOAD genotypes and controls on the white matter skeleton, tfce corrected p<0.05. A. APOE ε4-; B. APOE ε4+. 119

6.7 Group differences in FA between YOAD genotypes and controls on the white matter skeleton, tfce corrected p<0.05. A. APOE ε4-; B. APOE ε4+. 120

6.8 Group differences in MD between YOAD genotypes and controls on the white matter skeleton, tfce corrected p<0.05. A. APOE ε4-; B. APOE ε4+. 121

6.9 Group differences in AD between YOAD genotypes and controls on the white matter skeleton, tfce corrected p<0.05. A. APOE ε4-; B. APOE ε4+. 122

6.10 Group differences in RD between YOAD genotypes and controls on the white matter skeleton, tfce corrected p<0.05. A. APOE ε4-; B. APOE ε4+. 123

6.11 The correlations between NODDI metrics and cognitive function in YOAD patients (adapted from [271]) 125

6.12 The t statistic map of the direct comparison between APOE ε4+ YOAD patients and APOE ε4- YOAD patients, warm color APOE ε4+ YOAD patients < APOE ε4- YOAD patients, cool color APOE ε4+ YOAD patients > APOE ε4- YOAD patients 125

7.1 Group differences in annualised rate of change of NODDI metrics on the white matter skeleton, tfce corrected p<0.05. A. Faster decreasing rate of NDI in YOAD than controls in temporal, parietal and occipital white matter, fornix, the splenium of corpus callosum, and the cerebellar white matter; B. No group differences in the annualised rate of change in ODI between YOAD patients and controls; C. Faster increasing rate of FISO in YOAD patients than controls in mainly involving the temporal white matter, cerebellar white matter, fornix, and brainstem. 133

7.2 Group differences in NODDI metrics at the baseline on the white matter skeleton, tfce corrected p<0.05. These group differences in NODDI metrics between YOAD patients and controls showed a similar pattern as what we have found in Chapter 6.3.3.1. 134

7.3 Group differences in annualised rate of change of NDI in YOAD genotypes on the white matter skeleton, tfce corrected p<0.05. . . . 139

7.4 Group differences in annualised rate of change of FISO in YOAD genotypes on the white matter skeleton, tfce corrected p<0.05. . . . 140

7.5 Group differences in NDI in YOAD genotypes at the baseline on the white matter skeleton, tfce corrected p<0.05. 141

7.6 Group differences in ODI in YOAD genotypes at the baseline on the white matter skeleton, tfce corrected p<0.05. 142

7.7 Group differences in FISO in YOAD genotypes at the baseline on the white matter skeleton, tfce corrected p<0.05. 143

8.1 The lifespan trajectory of NODDI metrics in white matter with AMICO fitting and the standard fitting. 149

8.2 The Bland-Altman plots of NODDI metrics in white matter with AMICO fitting and the standard fitting. 150

List of Tables

5.1 The demographic summary of Controls and Pre-manifest HD individuals. N/A = non applicable. n.s. = not significant. 87
5.2 NODDI metrics of white matter ROIs selected in pre-manifest HDs and controls (FDR corrected, $p<0.05$), specifically a) ROIs with NDI group differences; b) ROIs with ODI group differences. 91

6.1 The Demographic and Clinical Characteristics. 114
6.2 NODDI metrics of all quadrant white matter ROIs on the white matter skeleton in YOAD and controls. 124

7.1 The Demographic of YOAD patients and controls. 132
7.2 The Demographic of controls and YOAD genotypes of patients. . . 132

Chapter 1

MOTIVATION

1.1 The context

Neurodegenerative diseases pose great challenges to the global healthcare. Since last century, life expectancies have greatly increased across the world, and the ageing population is becoming larger and larger. Age is one of the biggest risk factors of neurodegenerative diseases, and these diseases cause great financial and physical burden for patients themselves and their families as well as the whole society. However, there are still not many effective therapeutic plans against these diseases. This is in part due to the lack of the knowledge of the brain pathology in neurodegenerative diseases.

The traditional way of gaining the knowledge of the disease pathology is via post-mortem studies. However, this method has quite a few limitations. Firstly, most of post-mortem studies include relatively very few samples, and it is difficult to reproduce the findings. Secondly, it is impossible to study the relationship between the structure and function using this approach.

Powerful and sensitive neuroimaging techniques have been developed as windows to access the disease pathology *in vivo* and non-invasively. Especially, the recent advances in Magnetic Resonance Imaging (MRI) have provided compelling evidence and therefore greatly enlarged our knowledge of brain pathologies in neurodegenerative diseases [1]. Among the available MRI techniques, diffusion MRI is of particular interest as it could provide *in vivo* microstructural information on

biological tissue non-invasivly and has been successfully applied in studying white matter abnormalities in neurodegenerative diseases.

Monitoring white matter is vital in coping with the challenge brought by neurodegenerative diseases. White matter is the structural basis of functional integrations between brain regions, and the intertwining structure-function relationship suggests that white matter could provide invaluable insights into understanding the behavioral and cognitive impairments in patients with neurodegenerative diseases. Moreover, the atrophy of white matter has been recognized as a potential imaging biomarker for aiding clinical diagnosis of neurodegenerative diseases. And tracking the evolution of white matter atrophy might aid us to understand the progression of brain pathology in neurodegeneration. At present, the available MRI measures of white matter atrophy include volumetric metrics from T1-weighted MRI and microstructural metrics from diffusion-weighted MRI and other quantitative MRI methods. Changes at the microstructural level are likely to be the earliest sign of neurodegeneration, i.e., preceding volumetric losses and functional deficits. Detecting such microstructural abnormalities in white matter might benefit not only the understanding of abnormal functional activities, but also the earliest detection of neurodegeneration.

White matter microstructure configurations become accessible by measuring water molecule diffusion using diffusion MRI. Among the diffusion MRI techniques, Diffusion Tensor Imaging (DTI) is the first that has drawn great attention and has been widely used to study white matter microstructure in neurodegenerative diseases [2, 3]. White matter in patients with neurodegenerative diseases has been found to have abnormal DTI metrics (increased diffusivity and decreased fractional anisotropy (FA)) compared with normal controls (see [4,5] for reviews). Whilst sensitive to white matter microstructural changes in neurodegenerative diseases, due to the simplicity of the single tensor model in DTI, DTI metrics lack tissue specificity to biological features. For example, a decrease in FA of white matter in patients with neurodegenerative diseases might be caused by a decrease of axon density, an increase of free water contamination, or a combination of both. In addition, DTI

metrics are prone to free water contamination, which has been found to confound DTI findings of white matter abnormalities in clinical studies of neurodegenerative disease [6].

To provide biologically meaningful features that are free from free-water contamination, a set of biophysical diffusion MRI models have been proposed. One simple multi-compartment model - Neurite Orientation Dispersion and Density Imaging (NODDI) [7] has drawn our particular attention because of its simplicity and feasibility in clinical settings. With a multi-compartment model incorporating the isotropic diffusion contributed by free water, NODDI provides quantitative compartment-specific metrics that are of biological meaning and clinical interest in neurodegenerative diseases, including the neurite density index (NDI), providing an estimate of axonal density in white matter; the orientation dispersion index (ODI), quantifying the extent of axonal dispersion in white matter.

1.2 Problem statement

Given the theoretical advantages of NODDI, is NODDI feasible in studying white matter changes of neurodegenerative diseases? What benefit will it bring compared with the conventional DTI technique?

We are interested in evaluating the feasibility of NODDI and its added value over DTI in different stages of neurodegenerative diseases, i.e., preclinical and clinical, before and after disease onset. The feasibility here refers to:

- the sensitivity of NODDI to detecting abnormal white matter microstructural changes before and after disease onset;
- the sensitivity of NODDI to track longitudinal white matter microstructural changes after disease onset.

The preclinical neurodegenerative disease model we chose is pre-manifest Huntington′s disease (pre-HD, a full penetrant genetic disease), individuals of which could be identified many years before clinical onset by predictive genetic testing. The after-onset neurodegenerative disease model we chose is Alzheimer′s disease (AD), which is the commonest type of dementia.

1.3 Aims of PhD projects

An evaluation of the feasibility of translating NODDI in clinical studies of neurodegenerative diseases:

- its sensitivity to white matter abnormalities in different stages of neurodegenerative diseases - before and after clinical onset;
- its capability to track longitudinal white matter changes in neurodegenerative diseases;
- its clinical relevance by accessing the relationship of NODDI metrics with the clinical assessments;
- A comparative evaluation of NODDI and conventional DTI in clinical studies of neurodegenerative diseases cross-sectionally.

1.4 Structure of the thesis

The rest of this thesis is organised as below:

Chapter 2 - this chapter provides a general description of diffusion MRI technique, including the basic of water diffusion, how to measure water diffusion using MRI, how to infer white matter microstructural configurations using diffusion MRI, and how to analyse diffusion MRI images.

Chapter 3 - this chapter gives an overview of white matter pathology in neurodegenerative diseases. It first describes the white matter microstructure in the human brain, and then gives a general introduction of neurodegenerative disease and the two disease models selected to represent the preclinical and clinical stages of neurodegenerative diseases (pre-manifest HD and young onset AD). For these two selected disease models, this chapter also covers our understanding of the white matter pathology and what diffusion MRI techniques tells us about the white matter abnormalities in these two diseases.

Chapter 4 - this chapter describes all the key imaging factors that we need to think about when we design a clinical study using diffusion MRI, including image acquisition and image analysis.

Chapter 5 - this chapter establishes the feasibility of NODDI in depicting the *in vivo* white matter pathology at the pre-manifest stage of neurodegenerative diseases and its advantages over standard DTI. We applied both NODDI and DTI to study the white matter microstructural abnormalities in the pre-manifest Huntington's disease.

Chapter 6 - this chapter demonstrates the feasibility of NODDI in providing the details of *in vivo* white matter pathology at the clinical stage of neurodegenerative diseases and its advantages over standard DTI. Both NODDI and DTI were applied to assess the white matter microstructural changes in young onset Alzheimer's disease.

Chapter 7 - this chapter explores the feasibility of NODDI in tracking the longitudinal progression of white matter pathology in neurodegenerative diseases. We applied NODDI to detect the longitudinal progression of white matter microstructural abnormalities in a cohort of young onset AD and normal controls that we followed up at an interval of one year.

Chapter 8 - this chapter summaries all the key findings, discusses about the potential limitations of our studies and describes potential work in future.

Chapter 2

Diffusion Magnetic Resonance Imaging

This chapter aims to give an introduction to the basic principles behind diffusion MRI. It starts with subchapter 2.1, which introduces water diffusion - the basic physical phenomenon measured by diffusion MRI and its potential to infer biological tissue microstructure. Then in subchapter 2.2, it covers the principles of how MRI works and how to measure water diffusion in the tissue using diffusion MRI. The last subchapter 2.3 covers how to computationally infer tissue microstructural information by diffusion MRI models.

2.1 Water Diffusion

2.1.1 Molecular diffusion and Einstein equation

Molecular diffusion refers to the translational movements of molecules when the temperature is above 0 Kelvin [8]. This translational motion of molecules is also known as Brownian motion, which was first discovered by the botanist Robert Brown in 1827 when he observed the movements of pollen grains via a microscope [9]. The classical descriptions of the diffusion macroscopically are Fick's laws [10](Equations 2.1 and 2.2 for the first and second Fick's law respectively, where J is the flux of the particles and D is the diffusion coefficient and C is the concentration).

$$\vec{J}(r,t) = -D\nabla C(\vec{r},t) \tag{2.1}$$

$$-\nabla \cdot \vec{J} = \frac{\partial C(\vec{r},t)}{\partial t} \tag{2.2}$$

Einstein linked the Fick's laws to self-diffusion phenomenon in order to describe the molecular diffusion [11] (Equation 2.3).According to Einstein equation, in a self-diffusion process, the mean squared displacement of molecules r^2, after a time interval t, is proportional to the diffusion coefficient D. The diffusion coefficient D depends on not only the size of the molecules, but also the temperature and the viscosity of the medium in which the molecules exist and diffuse [12].

$$< r^2 >= 6Dt \tag{2.3}$$

2.1.2 Water diffusion probes the brain microstructure non-invasively

Molecular diffusion is useful to probe the microstructure non-invasively in a sampled material. In a free space, the thermal energy drives the molecules to diffuse freely and randomly along any direction. In contrast, in a sampled material, when the molecules come across any barriers, the motion slows down. That is to say, the diffusion of the molecules is more free in the direction along the barriers than that in the direction perpendicular to the barriers. Therefore, given an appropriate time interval, the distribution of molecule displacements in diffusion could reflect the microstructural configurations of a sampled material.

In diffusion MR imaging, water molecules are the target due to its abundance in biological tissue. The diffusion displacement of water molecules is affected by the biological barriers, e.g., the cell membranes, and the respective distribution of water diffusion could reflect the underlying microstructural configurations of the tissue [13, 14]. Therefore, by measuring water diffusion, we could infer the *in vivo* microstructural information of the biological tissue non-invasively.

2.1.3 Water diffusion in the brain

The brain can be roughly classified into three tissue types, including **cerebrospinal fluid (CSF)**, **grey matter (GM)** and **white matter (WM)**. Each type has its unique

configurations of the barriers for water diffusion. Therefore, the distribution of water molecule displacements shows unique patterns across the brain.

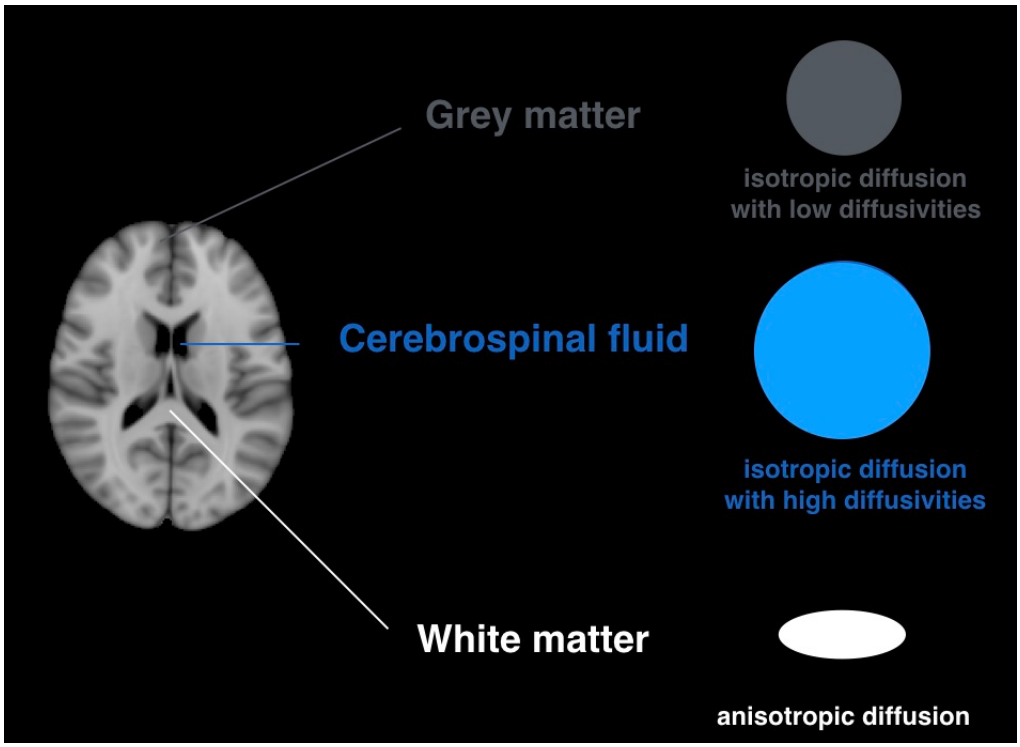

Figure 2.1: Water diffusion in the brain

A simple illustration is described in Figure 1. In CSF, as there is no obstacle, water molecules diffuse freely along any direction. Therefore, the water diffusion in CSF is isotropic and has a high diffusivity. GM mainly consists of neuronal cell bodies and dendrites. Due to the membrane obstacles of cell membranes, water diffusion in GM often has no orientation preferences and is still isotropic but much less than in CSF. Therefore, GM has a lower diffusivity than that in CSF. WM is sometimes referred to as the fiber tracts, and includes mainly the myelinated axons. In WM, water molecules diffuse freely along the fiber but highly restricted in the perpendicular direction, which results in anisotropic water diffusion in WM.

2.2 Measuring water diffusion in the tissue using MRI

This part explains how to measure water diffusion in the tissue using MRI, and has two parts: the first part introducing how MRI works (subsection 2.2.1) and the second part explaining how to encode diffusion with MRI (subsection 2.2.2).

2.2.1 Introduction to MRI

MRI is rooted in the quantum phenomenon **Nuclear Magnetic Resonance (NMR)**. This phenomenon refers to the process of absorbing and re-emitting the energy of protons, and was first reported in an experiment of measuring the magnetic momentum of chemical elements by Rabi et al in 1938 [15]. NMR was further described in the experiments of Bloch and Purcell in materials in 1946 [16]. The framework of spatial encoding using magnetic field gradients was the key invention that enabled the successful implementation of MRI systems. It was introduced by Lauterbur et al [17], which translated the physical phenomenon - NMR into the modern MRI systems we are using in both clinical practice and scientific research today.

In the following, we introduce the basics of nuclear magnetic resonance and the principles to form a MR image. Subsection 2.2.1.1 first describes the behaviour of protons in a magnetic field, and then covers how to measure the magnetic moments of protons. The subsection 2.2.1.2 describes how to form a MR image.

2.2.1.1 Basics of nuclear magnetic resonance

A charged proton rotates around its own axis and forms a **spin** - $\vec{J}$. The magnetic moment $\vec{\mu}$ is a property of nuclei that is related with $\vec{J}$, and is determined by $\vec{\mu}=\gamma\vec{J}$ where γ is the gyromagnetic ratio of the nucleus. After adding a strong external magnetic field $\vec{B_0}$, a torque from the external magnetic field causes magnetic moments $\vec{\mu}$ to precess and form a **non-zero net magnetization** $\vec{M}$ along with the direction of $\vec{B_0}$. Conventionally, we define z-axis as the orientation of the external static magnetic field $\vec{B_0}$ and we use “longitudinal” and “transverse” to describe quantities along z-axis and in *xy* plane. If we put the spins long enough in the external magnetic field, the sample will be fully “magnetized” and the net magnetization $\vec{M}$ will

fully align with $\vec{B_0}$ (i.e., the longitudinal magnetization reaches its maximum and the transverse magnetization in the *xy* plane is zero).

The frequency ω at which the magnetic moments precess is called as **Larmor frequency** [18], and is determined by

$$\omega = \gamma|\vec{B}| \tag{2.4}$$

, where $\vec{B}$ is the external field. Equation 2.4 suggests that the Larmor frequency is determined by the strength of the magnetic field $|\vec{B}|$ and the gyromagnetic ratio γ of the nucleus of a particle. For hydrogens of water molecules in a 3T magnetic field, the Larmor frequency is 128MHz.

2.2.1.2 Manipulating the system to detect the net magnetization

The signal contributed by this non-zero net magnetization $\vec{M}$ is too small to be detectable along z-axis (the direction of the main field). Therefore, we have to rotate $\vec{M}$ away from z-axis. To achieve this, we can apply a radiofrequency (RF) pulse to transfer energy to the protons [19]. After we terminate the RF pulse, $\vec{M}$ rotates back to the z-axis. During this process, the changing magnetization induces electric currents and a measurable signal arises. The angle we rotate is termed as flip angle [20], and a 90^o flip angle is often chosen.

After the excitation, the protons start losing the energy gradually and the net magnetization rotates back towards z-axis. The temporal evolution of the net magnetization introduces two mechanisms of relaxation. One is called as **the spin−lattice relaxation (longitudinal relaxation)** along the direction of $\vec{B_0}$ while the other is called as the **spin−spin relaxation** at the transverse plane.

The relaxation can be mathematically described by Bloch equations [21, 22]:

$$\frac{d\vec{M}}{dt} = \gamma\vec{M} \times \vec{B} - \frac{M_x\vec{i} + M_y\vec{j}}{T_2} - \frac{M_z - M_0\vec{k}}{T_1} \tag{2.5}$$

In equation 2.4, M_0 is the equilibrium value of M_z, $\gamma\vec{M} \times \vec{B}$ describes the precession, T_1 is the *spin-lattice* relaxation time and $T2$ is the *spin-spin* relaxation time. Notably, different types of tissue have different time constants of T_1 and T_2, determined

by the chemical and cellular structure in the tissue as well as the external magnetic field strength.

Spin-lattice relaxation, known as longitudinal relaxation, describes the exponential recovery process of the longitudinal component of the net magnetization [23]. The protons release energy into the environment via thermal interactions, which increases the temperature of the sample. This relaxation can be mathematically written as:

$$\frac{d\vec{M}_z}{dt} = \frac{M_0 - M_z}{T_1}\hat{z} \tag{2.6}$$

Spin-spin relaxation is also known as transverse relaxation [21]. The interactions between spins cause variations of the local magnetic field. This causes spins to rotate at different frequencies, and after a while the phases of spins become incoherent. If the main field B_0 is homogeneous, this relaxation can be mathematically written as:

$$\frac{d\vec{M}_{xy}}{dt} = \gamma\vec{M} \times \vec{B} - \frac{\vec{M}_{xy}}{T_2} \tag{2.7}$$

However, in practical MRI system, the external magnetic field is inhomogeneous, and this inhomogeneity introduces an additional dephasing mechanism. In reality, the decay of transverse magnetization is determined by a time constant T_2^*, which is short than T_2. If we use $T_2^{'}$ to describe the relaxation time of the extra dephasing mechanism, T_2^* can be mathematically described as:

$$\frac{1}{T_2^*} = \frac{1}{T_2} + \frac{1}{T_2^{'}} \tag{2.8}$$

2.2.1.3 MR image formation

For a 3-D object, the aim of spatial encoding is to produce a signal with the location information [24, 25]. And its framework consists of two parts: 1) the selection of a slice; 2) the within-slice localization [17].

Slice selection

As we described in Subsection 2.2.1, for a certain proton, the Larmor frequency has a linear relationship with the strength of the external magnetic field. If we

apply a gradient $\vec{G}_z$ along z-axis, the Larmor frequency of protons in each slice is determined by:

$$\omega = \gamma(B_0 + z|\vec{G}_z|) \tag{2.9}$$

By tuning the frequency of the RF pulse, we can decide which slice to be excited.

Spatial encoding within slice

An efficient way to encode locations within a slice is combining "frequency encoding" and "phase encoding" using pulsed gradients. Frequency encoding is similar as slice selection while phase encoding is to encode protons at different positions with characteristic phases by applying a phase-encoding gradient. Usually the phase encoding gradient is applied between slice selection and frequency encoding while the frequency encoding gradient is applied at the time we measure the signal.

After the excitation RF pulse, if we apply a gradient $\vec{G}_y$ along y-axis for a time duration of τ, the phase of the magnetization φ varies along y axis and stays as a unique constant value when we switch off this phase-encoding gradient $\vec{G}_y$ (Equation 2.10).

$$\varphi = \gamma|\vec{G}_y|y\tau \tag{2.10}$$

If we apply a gradient $\vec{G}_x$ along x-axis, the Larmor frequency varies along x axis and is determined by:

$$\omega = \gamma|\vec{G}_x|x \tag{2.11}$$

2.2.1.4 MRI pulse sequences

A MRI pulse sequence is a sequence of RF pulses and turn-on/turn-off magnetic gradients as programmed. The key parameters of a MRI pulse sequence are: echo time (TE)/repetition time (TR), flip angle, Field Of View (FOV), matrix size, inversion pulses, the spatial acquisition strategy of k-space (the space in which we acquire the signal, and see page 41 for more information), diffusion weighting factor b (for diffusion MRI). The most common pulse sequence used in diffusion MRI is the **pulsed gradient spin echo (PGSE) sequence** [26].

Spin echo was developed by Dr. Erwin Hahn [27] in 1949 to 1) measure the maximum of the signal from the net magnetization and 2) avoid potential artefacts due to the susceptibility of the signal to the inhomogeneity of the local magnetic field. When we remove the 90^o RF pulse, the signal detected starts to decay rapidly. Therefore, a very fast detection is requried [28]. However, this demands high performances of hardware. The first spin echo scheme proposed by Han was a combination of two 90^o RF pulses [27]. By utilizing the refocusing of the second RF pulse, the spin echo scheme recovers part of the signal of interest. Carr and Purcell [29] improved it using a combination of one 90^o RF pulse and a 180^o RF pulse. The flip angle of the second RF pulse could be arbitrarily chosen but the 90^o-180^o RF pulses provide the maximum of the echo signal magnitude, which is as twice as the initial 90^o-90^o RF pulses. Therefore, this 90^o-180^o RF pulses is widely used in diffusion MRI today and is described in detail next.

Spin Echo

When we apply the 90^o RF pulse, the selected protons are "excited" and the transverse component of the net magnetization increases rapidly. Once we remove this RF pulse, the relaxation process starts. The spin-spin relaxation makes spins rotate at different frequencies and therefore forms a phase incoherence (i.e., dephasing). This dephasing of spins results in the decreasing of the transverse component of the net magnetization.

Spin Echo (SE) works by refocusing the phases of spins by applying an 180^o RF pulse for a time twice of the duration of the first 90^o RF pulse. The time between the 90^o RF pulse and the signal read-out pulse is TE. The 180^o RF pulse is applied at half of TE, i.e., TE/2, and has an area as twice as the 90^o RF pulse. Once the 180^o RF pulse is applied, the spins rotate by 180^o and continue their precessions but in the opposite direction. Spins that precess faster after the 90^o RF pulse now fall behind. As they precess faster, they gradually catch up with the spins that precess slower after the 90^o RF pulse. The more coherent the phases of spins become, the more the transverse magnetization is recovered. This SE scheme diminishes the phase differences caused by $T2^*$ effect, and the signal measured using SE scheme

is referred to as the SE signal. Notably, the SE signal after refocusing is smaller than that of the signal at the time when we remove the 90^o RF pulse. This is due to factors such as the thermal relaxation.

A perfect refocusing by the 180^o RF pulse could not be achieved at cases: 1) the local field distortion changes; 2) the spin moves to a different place. The second case is invaluable for measuring diffusion with MRI, which is discussed later in Section 2.2.2. described in detail next.

The Pulsed Gradient Spin Echo Sequence

The three common RF pulses in all PGSE sequences are 90^o RF pulse and 180^o RF pulse as well as the signal readout pulse (echo). The PGSE sequence is repeated at a time interval of TR to sample the k-space (see the next subsection for details) to reconstruct the image.

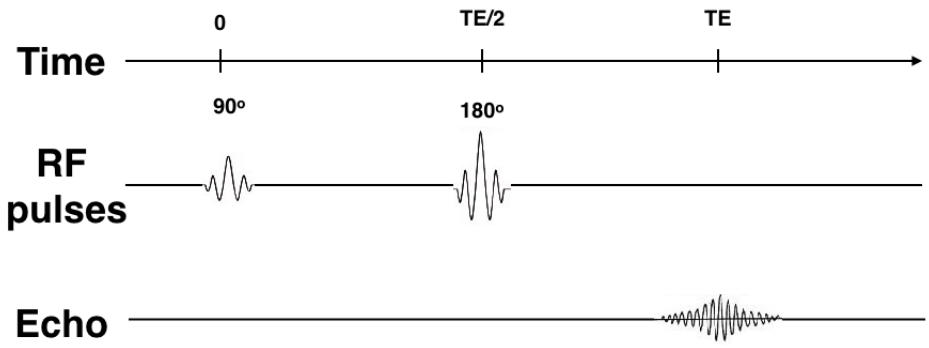

Figure 2.2: The framework of single echo PGSE sequence

The conventional PGSE sequence is single echo PGSE, which only includes one 180^o RF pulse after 90^o RF pulse and one readout (i.e., one "echo"). This single echo PGSE sequence (Figure 2.2) produces images with very good signal-to-noise rate (SNR) but is time consuming because this sequence sample each line in k-space with a time of one TR.

K-space

K-space is the frequency domain of image space [30], introduced into MRI by likes in 1979 [31] and Ljunggren and Twieg in 1983 [32, 33]. In MRI, we measure the

signals in k-space and reconstruct images using Fourier transform (see Figure 2.3 for an example).

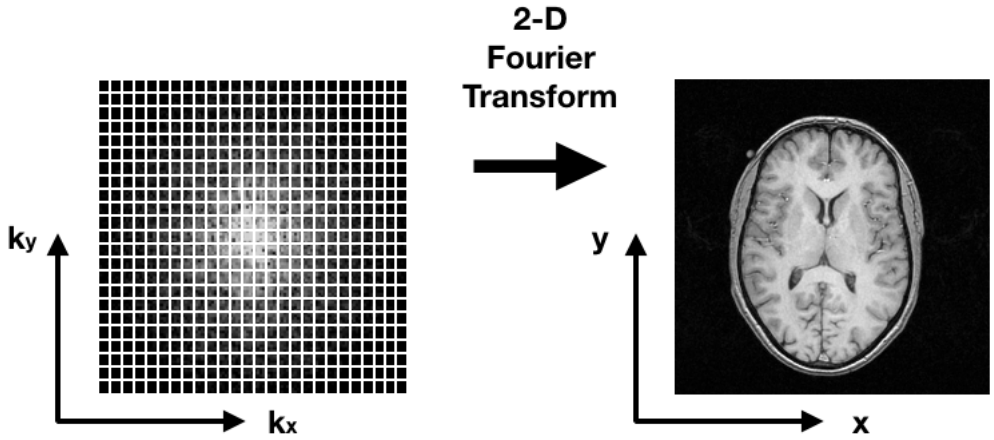

Figure 2.3: An example of Fourier transform between k space and image space

In k-space, low values around the origin carry the information at low spatial frequencies while high values carry the information at high spatial frequencies. Sampling along the x-axis in the k space represent sampling the spatial frequencies along x axis in the image space. It is the same with sampling along the y axis. The center in K-space determines the overall image contrast, brightness and shapes [30]. $\frac{1}{\Delta k}$ determines FOV, and the number of Δk defines the matrix size.

If we define the vector $\vec{k} = \gamma \int \vec{G} dt$ and leave out the constant phase caused by the static magnetic field B_0, we can rewrite the signal as

$$\vec{S}(\vec{k}) = \int \vec{M}_{xy}(\vec{r}) e^{i(\vec{k}\cdot\vec{r})} d\vec{r} \tag{2.12}$$

Sampling in K-space

K-space has an infinite number of points, and it's not possible to sample completely in k space. Practical k-space sampling is discrete, and forms "grid" or "matrix". A "grid" that is evenly distributed in k-space makes the data acquisition and image reconstruction faster, easier and much more efficient.

There are several k-space sampling trajectories in MRI acquisition, and cartesian scheme is the most widely used one in clinical scanners. In cartesian scheme,

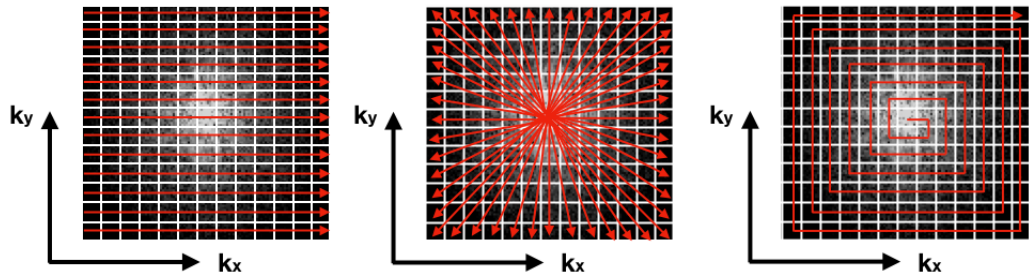

Figure 2.4: Common k-space sampling trajectories. A The cartesian scheme; B The radial scheme; C The spiral scheme.

the frequency encoding gradient and phase encoding gradient are separately applied at the signal read-out and in the interval between RF pulse and read-out pulses. After applying phase encoding gradient for a time τ , we apply frequency encoding gradient for a time t and read out the signal at the periodic intervals until the line is filled, then move to the next, and repeat this process until the sampling designed in k-space is finished. Therefore, this Cartesian method results in a line-by-line trajectory in k-space (Figure 2.4 A). Notably, there are other k-space sampling methods, such as radially (Figure 2.4 B) and spirally (Figure 2.4 C) oriented trajectories. However, they are much less accessible for clinical scanners.

Echo Planar Imaging

Echo Planar Imaging (EPI) is a fast k-space sampling method [34], and was proposed in 1977 by Mansfield [35] but became popular after 1980s. Since then, EPI has been the most common pulse sequence used in MRI. EPI works by recording signals multiple times after each excitation, covering line by line in k-space without going back to the origin. This results in a "zig-zag" sampling trajectory in k-space. Notably, with different settings, EPI can be 2D and 3D, either spin-echo or gradient-echo, and single-shot or multi-shot.

The time efficiency of EPI makes the fast image acquisition realistic for diffusion MRI. For single-shot EPI, there is only one excitation for the whole k-space sampling (Figure 2.5. A). In contrast, for multi-shot EPI, only part of the k-space is sampled after one excitation and therefore the k-space sampling requires multiple

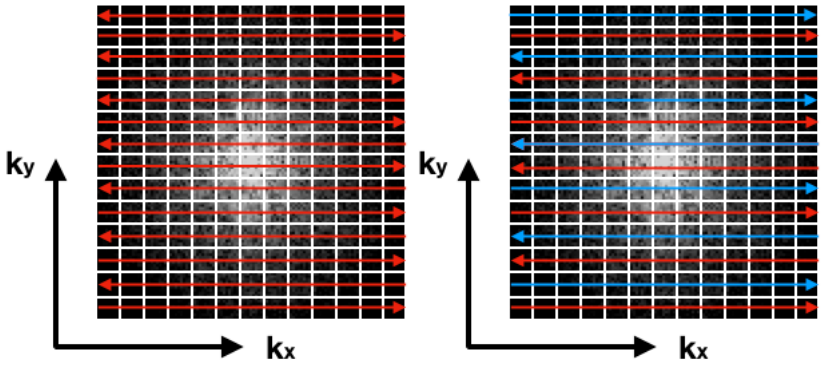

Figure 2.5: Echo Planar Imaging in k space. A single shot k-space trajectory; B multi-shot k-space trajectory

excitations. Figure 2.5 B is an example of multi-shot EPI, which illustrates that only odd-numbered or even-numbered slices are recorded in each shot. Despite of its time efficiency, EPI has its limitations and results in unique MRI image artifacts (See **section 2.2.2.2** artifacts in diffusion MRI images for further details).

2.2.2 Encoding diffusion using MRI

2.2.2.1 Measuring water diffusion using MRI

The sensitivity of MRI to self-diffusion was first reported by Hahn in 1950 when he observed a signal reduction using the SE sequence [27]. He also proposed that the diffusion coefficient is measurable. But it was until 1954 that Carr and Purcell [29] came up with a framework using Hann's spin-echo sequence to measure such phenomenon. Carr and Purcell found that the magnitude of SE signal is highly sensitive to random molecular diffusion. A decade later, Stejskal and Tanner [26] designed the Pulsed Gradient Spin Echo (PGSE) sequence (Figure 2.6) using short-duration gradient pulses.

In PGSE, the gradient pulse duration δ is much shorter than Δ (the spacing between the two gradients $\vec{G_D}$), and the net phase difference for spins betweens the two gradients is determined by their positions at two time points. If spins diffuse during the time between the two gradient pulses, the signal is smaller than that when the spins stay at the same place. In diffusion MRI, the signal measured by PGSE

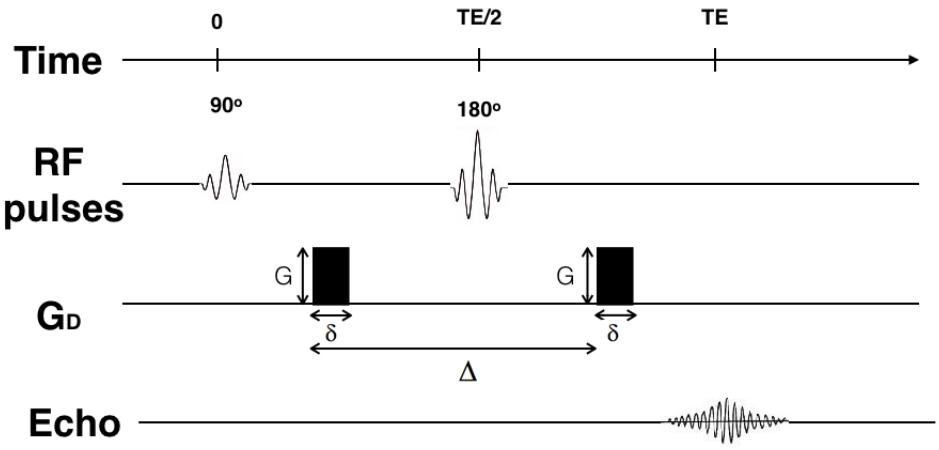

Figure 2.6: The scheme framework of pulse gradient spin echo sequence

sequence could be expressed as:

$$S(\vec{q}) = S(0) \int p(\vec{r}) e^{-i\vec{q}\cdot\vec{r}} d\vec{r} \tag{2.13}$$

where $S(\vec{q})$ and S_0 are the signals acquired with or without the diffusion weighting gradients respectively, $p(\vec{r})$is the probability density distribution of water molecule displacements, $\vec{q} = \gamma\delta\vec{G}$, and $\vec{r}$ is the diffusion displacement between the two diffusion-encoding gradient pulses.

The sensitivity of MRI to diffusion is characterized by the well-known "b-value" or "b factor" [36, 37], which is also known as the diffusion weighting factor, is given by:

$$b = q^2(\Delta - \frac{\delta}{3}) = (\gamma\delta G)^2(\Delta - \frac{\delta}{3}) \tag{2.14}$$

Notably, this only stands when $\delta << \Delta$ with single diffusion encoding. The general definition of b value is:

$$b = \gamma^2 \int_0^t |\int_0^{t'} G^*(t'')dt''|^2 dt' \tag{2.15}$$

where G^* is the effective diffusion gradient (see [38] for more details on the relevant physics).

2.2.2.2 Artifacts and distortions in diffusion MR images

Artifacts in MRI images refer to those signals that do not represent the signal from the tissue in the respective voxel but occur due to the way the scan is performed. And MRI images are prone to artifacts. Some of the artifacts are irreversible but some can be avoided or minimised by carefully selecting the acquisition parameters of the protocol and/or giving proper instructions for both the radiologists and the participants. Therefore, a good knowledge of the MRI artifacts and their causes is essential in setting up the MRI acquisition protocol and performing image acquisition and analysis. The following describes some of the artifacts that people often see in diffusion MR images.

The motion artifacts

For the clinical scanner, it takes about 5 to 10 mins for a typical single-shell data acquisition and about 12 to 20 mins for a multi-shell data acquisition. Such a long time can be very difficult for human to stay still throughout the whole scan, especially for patients with movement disorders or children. The bulk head movement introduces an inconsistency of head position, and lead to mismatching of brain structures throughout the scan. For example, a common motion-induced artifact in clinical data is signal dropout in one or more Diffusion Weighted Images (DWI) volumes (Figure 2.7). In such cases, the diffusion-weighted MRI signal acquired is either not from the same voxel or incomplete. This brings confounding factors into estimating diffusion MRI metrics and the further image analysis.

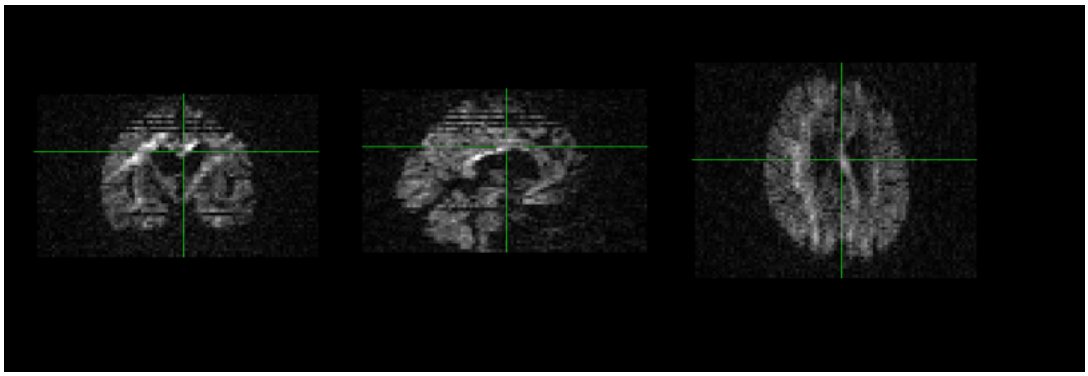

Figure 2.7: An example of signal dropout in multiple slices in DW images

The distortions of brain anatomy caused by eddy currents

The rapid on-and-off gradients for imaging results in time-varying eddy currents. According to Faraday′s law of induction, these currents introduce time-varying magnetic fields. These magnetic fields are in general small, but still introduce bias to the spatial-encoding gradients we use, and consequently distort the geometry of the brain [39].

The EPI distortion

EPI is very sensitive to the inhomogeneity of the static external magnetic field. The distortions in EPI are pronounced most in the air-tissue interfaces and in the ventral portions of the temporal and frontal lobes (Figure 2.8). Various methods have been proposed to correct this distortion [40,41] and one of the popular method is to estimate the inhomogeneity of the field strength with images acquired at two opposite phase-encoding directions [42]. However, this doubles the scan time and may not be appropriate for clinical studies.

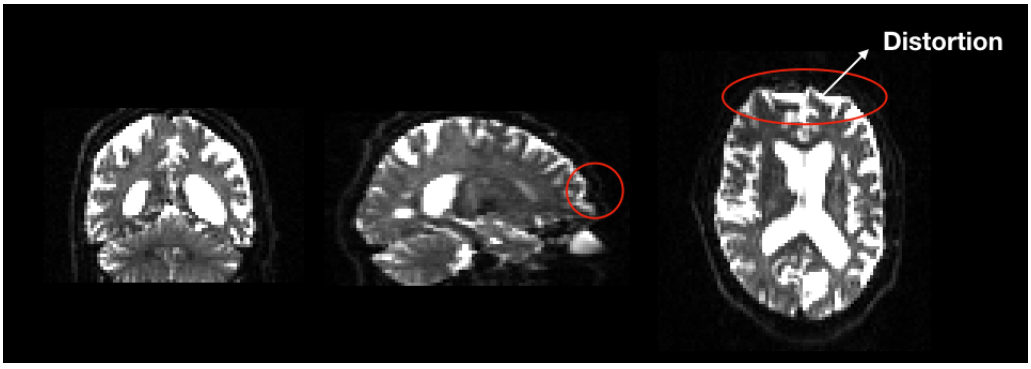

Figure 2.8: An example of EPI distortion

In addition to those artifacts we mentioned above, there are some other common artifacts in MR images such as chemical shifting (Figure 2.9), ghosting, ringing, stripping, blurring, spiking (due to a failure of sampling in k-space) and wrapping (due to the too small FOV) (See [43] for further details).

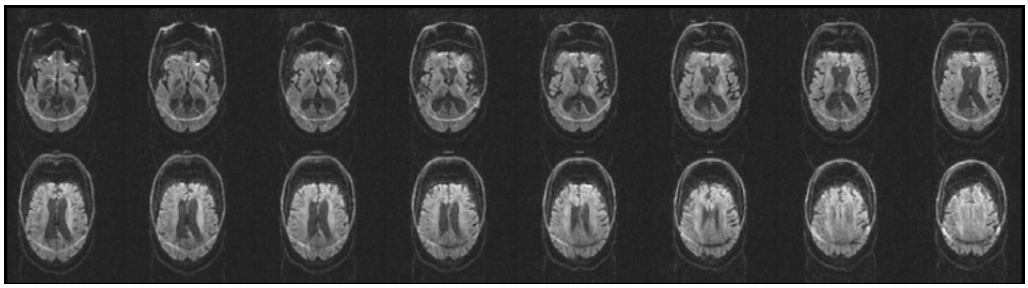

Figure 2.9: An example of chemical shifting in the brain

2.3 Inferring white matter microstructural configurations using diffusion MRI

The goal of microstructural imaging in biomedicine is to provide quantitative imaging biomarkers that reflect tissue properties of interest (Figure 2.10). Among the available techniques, diffusion MRI is unique in a way that it not only is sensitive to the microstructural configurations at a much finer scale than other imaging techniques available but also is non-invasive, relatively cheap and easy accessible. Since the successful implementations of acquiring diffusion MRI images of the *in vivo* human brain [36, 44, 45], various diffusion MRI models have been proposed (see [14, 46] for a review) and can be categorised into 3 groups according to the target the model is designed to describe [47]: 1) models of the tissue; 2) models of the signal; 3) models that describe both the tissue and the signal .

Models of the tissue in group 1 are often referred to as biophysical models, and utilise multi-compartment approaches [49–51] to explicitly describe the tissue microstructure based on realistic assumptions [7, 52–61]. Models of the signal in group 2 use mathematical models to describe the diffusion weighted MRI signals without any hypotheses on the impact of tissue microstructure on the diffusion MRI signals [62–70]. Models in group 3 share certain characteristics in Group 1 & 2, which describe the signals from fiber populations but only capture very few tissue microstructural features (e.g., fiber orientation distribution function) [71–81].

The simplest model of all is Apparent Diffusion Coefficient (ADC), which was proposed at the same time as the first diffusion MRI images of the human brain were generated [37]. ADC models the signal according to Einstein's equation and

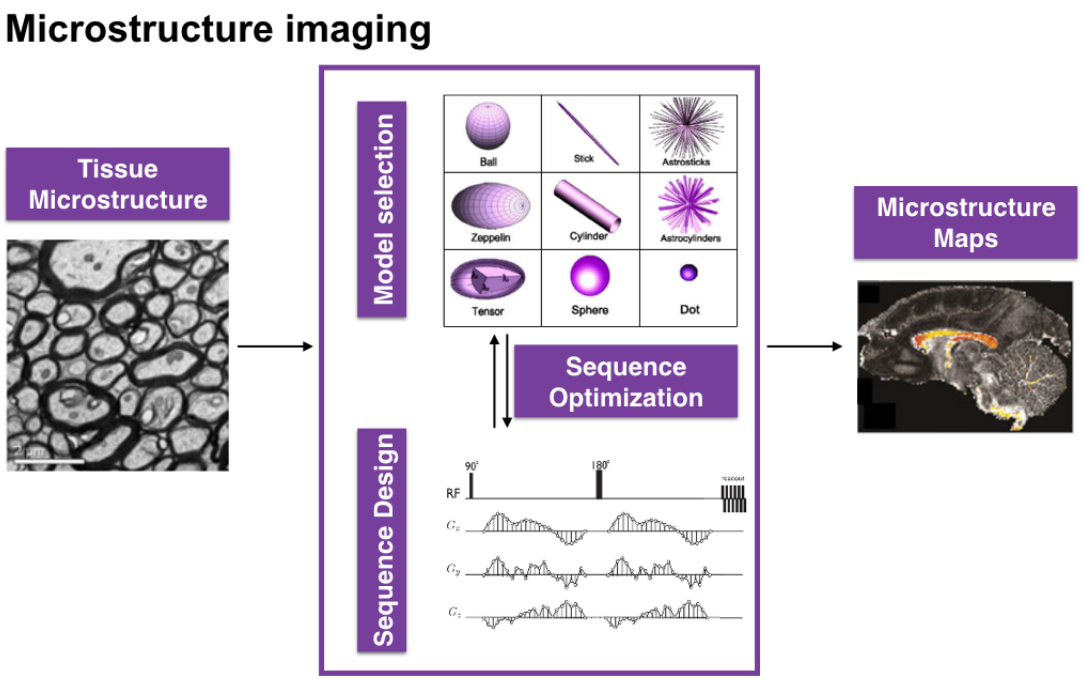

Figure 2.10: Microstructure imaging using diffusion MRI. Illustration adapted from previous work [14, 48]

provides a global and statistical metric (often referred to as ADC too). Therefore, diffusion weighted signal we acquire can be mathematically written as:

$$S = S_0 e^{-bADC} \tag{2.16}$$

ADC provides relatively good tissue contrast when b value is not too high, and it has been widely used in various conditions [82]. However, the actual value of ADC depends greatly on the direction of the diffusion gradient. Therefore, ADC values are relatively less comparable across studies.

The most popular diffusion MRI model in the last 20 years is DTI. DTI utilizes a second-order tensor **D** model to describe the distribution of water diffusion in 3D space [2, 3], and has been widely used in clinical and neuroscientific studies to study white matter microstructure (see [83] for a review). Under abnormal conditions, DTI has been demonstrated to be sensitive to white matter microstructural changes, such as mild cognitive impairment and Alzheimer's disease (AD) (see [84] for a review), brain tumor (see [85] for a review), Parkinson's disease (see [86] for

a review), traumatic brain injury (see [87–89] for reviews) and so on. However, the single tensor model in DTI assumes a single Gaussian distribution of water diffusion, and is too simple to provide more information on complex paradigms of fiber configurations [90]. That is to say, DTI metrics lack specificity to properties of tissue microstructure. For example, the popular DTI metric - fractional anisotropy (FA) can be affected by multiple factors, such as myelination, the permeability of axonal membranes, axonal orientation dispersion, the packing density of axons and so on. Therefore, changes in FA could not directly be attributed to changes in specific tissue features. Changes in other popular DTI metrics - Axial Diffusivity (AxD) and Radial Diffusivity (RD) are widely accepted to be sensitive to changes in axon density and demyelination (see [91] for a review). However, this interpretation does not always hold. For example, using simulations, Wheeler-Kingshott et al. [92] has demonstrated that in crossing fibers, AxD and RD are mutually dependant on each other. Whenever one of them changes, it causes changes in the other. They also showed that under abnormal conditions, the changes in RD might be related to the change of the principal direction of the tensor in those voxels. Therefore, one should always be very careful to directly link the AxD/RD findings with changes in the underlying tissue microstructure. In addition, DTI also suffers from partial volume effect and DTI metrics are prone to free water contamination [6].

With recent advances in MRI hardware and sequences, diffusion MRI datasets with richer information (multiple diffusion weighted gradient directions and higher diffusion weightings (i.e., b values)) have become more and more accessible in clinical scanners, and various models have been proposed based on these datasets. One example of signal models in group 2 is Diffusion Kurtosis Imaging (DKI) [64]. DKI estimates the kurtosis (i.e., the non-Gaussianity of the diffusion probability distribution function), and has been applied in studying aging [93, 94], epilepsy [95, 96], tumor [97, 98] and so on. Whilst extending to characterise the non-gaussian water diffusion, DKI metrics still lack in tissue specificity as other advanced diffusion MRI signal models in group 2.

Models in group 1 describe the diffusion weighted MRI signal as a linear com-

bination of signals contributed by different tissue compartments. Each compartment represents specific pools of water molecules in different environments and each water pool has a unique pattern of water diffusion that can be represented by simple geometrical shapes. Stanisz et al for the first time found that the diffusion process in neural tissue could be represented by a three-compartment model [50]. The recent multi-compartment biophysical models were designed to capture various properties of tissue microstructure, including: 1) axon diameter - CHARMED [54, 99], AxCaliber [100, 101] and ActiveAx [57, 102]; 2) axon density or the volume fraction of intra-cellular water - CHARMED, AxCaliber, NODDI, DIAMOND [60], Bingham-NODDI [103], and Multi-compartment microscopic diffusion imaging using Spherical Mean Technique (SMT) [61]; 3) the fibre orientation dispersion - NODDI, Bingham-NODDI; 4) the permeability - Karger model [104], Apparent exchange rate imaging [105], a machine learning based compartment models with permeability [106]. Given the theoretical advantage of these multi-compartment models, further work towards the clinical translation of such techniques is highly demanded. Out of these models, NODDI is a very simple model that only requires clinically-feasible datasets. And it is also the only multi-compartment diffusion MRI model that has been validated with histological measures in human neural tissue [107]. Therefore, NODDI is the ideal candidate for the translation of advanced diffusion MRI techniques into clinical studies.

2.3.1 Diffusion tensor imaging (DTI)

2.3.1.1 Mathematical descriptions of DTI

DTI uses a single 2nd-order tensor **D** in 3-D space to describe the distribution of water diffusion (Figure 2.11). Mathematically, it can be written as a 3-by-3 symmetrical covariance matrix:

$$D = \begin{bmatrix} D_{xx} & D_{xy} & D_{xz} \\ D_{yx} & D_{yy} & D_{yz} \\ D_{zx} & D_{zy} & D_{zz} \end{bmatrix} = \begin{bmatrix} \vec{v}_1 \vec{v}_2 \vec{v}_3 \end{bmatrix} \begin{bmatrix} \lambda_1 & 0 & 0 \\ 0 & \lambda_2 & 0 \\ 0 & 0 & \lambda_3 \end{bmatrix} \begin{bmatrix} \vec{v}_1 \vec{v}_2 \vec{v}_3 \end{bmatrix}^{-1} \quad (2.17)$$

where the diagonal elements (D_{xx}, D_{yy}, and D_{zz}) represent the diffusion coefficients along x, y and z axis while the off-diagonal elements represent the diffusion covariance between each pair of axes. By decomposition, a 2nd-order tensor **D** can be represented by eigenvalues (λ_1, λ_2, λ_3) and eigenvectors ($\vec{v_1}$, $\vec{v_2}$, $\vec{v_3}$, with a dimension of 3 by 1) (Equation 2.14).

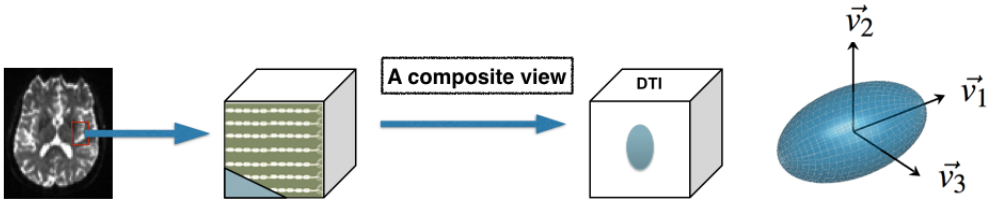

Figure 2.11: An illustration of the single tensor model in DTI

2.3.1.2 Tensor fitting

For each voxel, the tensor **D** is estimated by fitting a tensor into the diffusion attenuated MRI signal using a linear/nonlinear least square fitting. As **D** is symmetrical, only 6 elements require estimations, including D_{xx}, D_{xy}, D_{xz}, D_{yy}, D_{yz} and D_{zz}. Therefore, with a minimum acquisition consisting of 6 DWI volumes acquired at non-colinear diffusion gradient directions with the same diffusion weighting and 1 without diffusion weighting, we could compute a tensor **D** for all the voxels within the images. There are many choices of software available for ensor fitting, such as FSL [108], DTIstudio [109], Camino [110] and so on.

2.3.1.3 Computing DTI metrics

Various DTI metrics were proposed, and the most widely used ones are FA, AxD, RD, and Mean Diffusivity (MD). The equations below describe how to compute these popular DTI metrics based on the eigenvalues [λ_1, λ_2, λ_3] of the tensor D ($\lambda_1 > \lambda_2 > \lambda_3$).

$$MD = \frac{\lambda_1 + \lambda_2 + \lambda_3}{3} \tag{2.18}$$

$$AxD = \lambda_1 \tag{2.19}$$

$$RD = \frac{\lambda_2 + \lambda_3}{2} \tag{2.20}$$

$$FA = \sqrt[2]{\frac{(\lambda_1 - MD)^2 + (\lambda_2 - MD)^2 + (\lambda_3 - MD)^2}{2(\lambda_1^2 + \lambda_2^2 + \lambda_3^2)}} \tag{2.21}$$

As the equation suggests, FA describes the anisotropy of water diffusion along different directions. It has a range of 0-1, and is often regarded as a marker of white matter tract integrity. MD describes the mean magnitude of water diffusion across all the directions we measure. AxD describes the magnitude of water diffusion along the principal eigenvector of the tensor $\vec{v_1}$, and RD describes the average magnitude of water diffusion along the other two eigenvectors ($\vec{v_2}$ and $\vec{v_3}$).

2.3.2 Neurite orientation dispersion and density imaging (NODDI)

2.3.2.1 Mathematical descriptions of NODDI

NODDI describes water diffusion in each voxel as three compartments, including intra-neurite, extra-neurite and free-water compartments. Mathematically, the diffusion weighted MR signal can be written as a linear combination of signals contributed by these three compartments (Equation 2.19).

$$S = (1 - f_{iso})(f_{ic}S_{ic} + (1 - f_{ic})S_{ec}) + f_{iso}S_{iso} \tag{2.22}$$

where S is the normalized diffusion weighted signal, and S_{ic}, S_{ec} and S_{iso} are the normalized diffusion weighted signal decays contributed separately by the intra-neurite compartment, extra-neurite compartment and free water compartment, and f_{ic}, f_{ec} and f_{iso} are the volume fractions of the respective compartments.

S_{ic} represents the normalized signal contributed by the intra-neurite compartment (neurites, modelled as zero-radius cylinders), and can be mathematically described as:

$$S_{ic} = \int_{S^2} f(\vec{n}) e^{-bd_{||}(\vec{q}\times\vec{n})} d(\vec{n}) \tag{2.23}$$

where $\vec{q}$ is the diffusion-weighted gradient direction, $f(\vec{n})$ is the probability density of a stick (i.e., a zero-radius cylinder) along the direction, and $d_{||}$ is the intrinsic diffusivity. Watson distribution is chosen as the mathematical description of $f(\vec{n})$, and

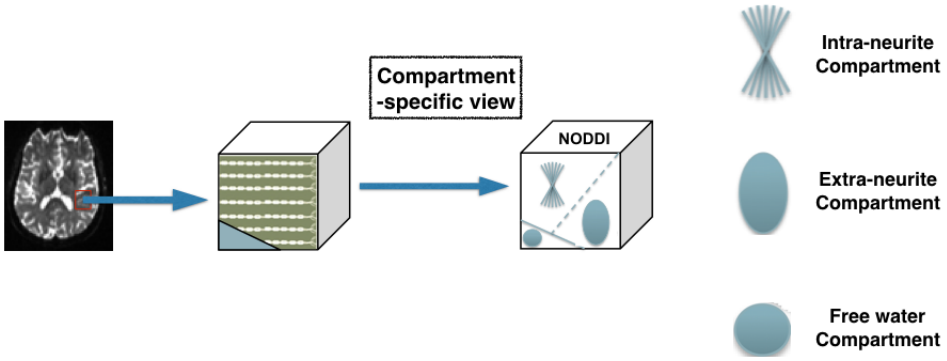

Figure 2.12: An illustration of NODDI model

is determined by a concentration parameter kappa κ) and the mean orientation $\vec{\mu}$. In the intracellular compartment, water diffusion is free along the direction of axons and dendrites but highly restricted in the perpendicular direction by the membrane barriers, and therefore referred to as **"restricted diffusion"**.

S_{ec} represents the normalized signal contributed by the extra-neurite compartment (glial cells and cell bodies, modelled as a cylindrically symmetric tensor (also known as "zeppelin"), and can be described as:

$$S_{ec} = -b\vec{q}^T(\int_{S^2} f(\vec{n})D(\vec{n})d\vec{n})\vec{q} \tag{2.24}$$

where $D(\vec{n})$ is an anisotropic tensor with the same eigenvalue in the two perpendicular directions. $\vec{n}$ is the principal direction of $D(\vec{n})$, $d'_{||}$the parallel diffusivity , $d'_{\perp}$and the perpendicular diffusivity. In NODDI, the parallel diffusivity $d'_{||}$ in the extra-neurite compartment is not set as the intrinsic diffusivity $d_{||}$, but equals to $d_{||}f_{ic}\tau_1$ to take the effect of orientation dispersion into consideration. τ_1 is defined as:

$$\tau_1 = \frac{-1}{2\kappa} + \frac{1}{2F(\sqrt[2]{\kappa})\sqrt[2]{\kappa}} \tag{2.25}$$

where $F(x) = \frac{1}{2}\sqrt[2]{\pi}e^{-x^2}erfi(x)$, and $erfi(x)$ is the imaginary error function. And the perpendicular diffusivity $d'_{\perp}$ has a tortuosity relationship with the intrinsic diffu-

sivity, and equals to $d'_{\perp} = (1 - f_{ic})d'_{\parallel}$. In this extra-neurite compartment, the water diffusion is hindered by two types of tissue, glial cells and cell bodies (somas), and therefore is referred to as **"hindered diffusion"**.

S_{iso} represents the normalized signal contributed by the free water compartment (modelled as a ball), and can be mathematically described as:

$$S_{iso} = -bd_{iso} \tag{2.26}$$

where d_{iso} is the free water diffusivity. In free water compartment, water molecules move freely, and have isotropic diffusion.

NODDI provides estimations of two tissue features of interest. One is Neurite Density Index (NDI) that is the volume fraction of the sticks. The more axons there are in white matter, the higher the NDI is. The other is Orientation Dispersion Index (ODI), derived from the concentration parameter of Watson distribution κ, which can be mathematically written as:

$$ODI = \frac{2}{\pi}\arctan(\frac{1}{\kappa}) \tag{2.27}$$

ODI describes the degree of the dispersion of dendrites from strictly parallel to fully dispersed with the respective value of 0 to 1. The more dispersed the dendrites are aligned with each other, the higher the ODI is. There is one more quantitative metric from NODDI, the volume fraction of free water f_{iso}, termed as $FISO$ in this thesis.

2.3.2.2 NODDI fitting

For each voxel, NODDI fitting is implemented by searching for a set of parameters $\vec{p}$ that maximize the log likelihood between the measurements and the predicted signals using a noise model with rician distribution. The log likelihood is defined as:

$$\log L(\vec{p}) = -2M\log v + \sum_{m=1}^{M}\log I_0(\frac{S_m S'_m(\vec{p})}{v^2}) + \log S_m - \frac{S_m^2 + S'_m(\vec{p})^2}{2v^2} \tag{2.28}$$

where S_m is the $m-th$ measurement, $S_m^{'}$ is the predicted signal from NODDI model at the corresponding settings of S_m acquisition, v is the spread of the rician distribution and I_0 is the modified first kind and $0-th$ order Bessel function.

The fitting procedure for NODDI includes two stages. A **grid search** is performed before the **gradient descent search**. The **grid search** is to identify a set of plausible parameters from a pool of parameters within their range for the microstructure within each voxel. And this set of parameters is used as the input for the second stage of fitting - **gradient descent search**. Using the results of grid search as the starting points for gradient descent search improves the time efficiency and accuracy of fitting. The NODDI fitting is implemented in a matlab package (http://mig.cs.ucl.ac.uk/index.php?n=Tutorial.NODDImatlab).

2.3.2.3 NODDI metrics

The complete set of model parameters in NODDI includes:

- f_{ic}, the volume fraction of the intracellular compartment (referred as NDI throughout this thesis);
- f_{iso}, the volume fraction of the free water compartment (referred as FISO throughout this thesis);
- $kappa$, the concentration parameter of Waston distribution used to represent $f(\vec{n})$;
- $\vec{\mu}$, the main orientation of Waston distribution;
- $d_{\parallel}$, the intrinsic diffusivity;
- d_{iso}, the isotropic diffusivity of free water.

The diffusivities $d_{\parallel}$ and d_{iso} in NODDI are set at typical values for in-vivo brain tissue: $d_{\parallel}$ equal to $1.7 \times 10^{-3} mm^2/s$ and d_{iso} equal to $3.0 \times 10^{-3} mm^2/s$ as in Alexander et al., 2010 [57] and Zhang et al., 2011 [111]. ODI is computed from kappa using equation 2.24.

2.4 Diffusion MR Image Analysis

After estimating diffusion MRI metric, the next step in a diffusion MRI processing pipeline is diffusion MRI image analysis. In either case or population studies of the human brain white matter, popular quantitative analysis approaches in diffusion MRI include voxel-wise analysis and regions of interest (ROI) analysis. The following describes the popular approaches: voxel-based analysis (VBA), tract-based spatial statistics (TBSS), tractography, and region of interest (ROI) analysis(Figure 2.13).

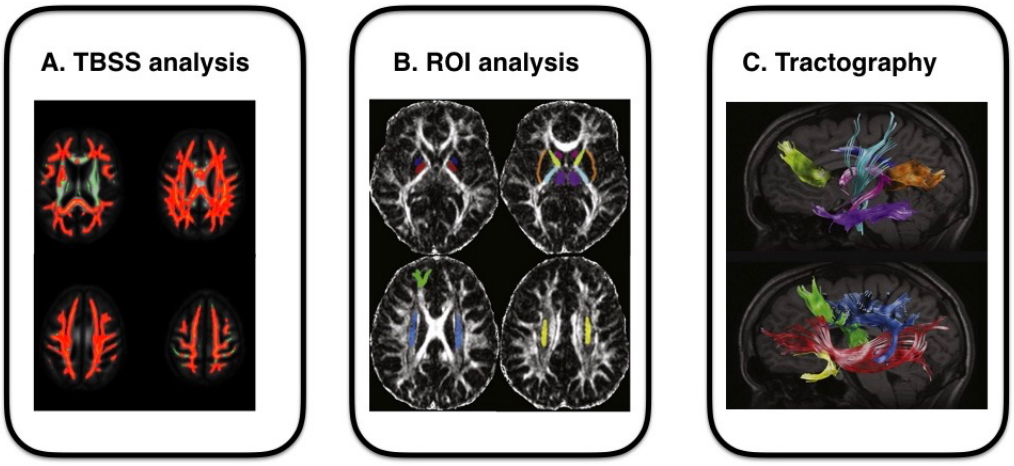

Figure 2.13: Popular image analysis methods in diffusion MRI. Figure B and C were adapted from Lebel et al., 2008 [112]

2.4.1 Voxel-based analysis

Voxel-based analysis (VBA) is an automated method in medical imaging research, and it performs group comparisons or correlation analysis voxel by voxel [113–117]. A whole brain white matter VBA is an ideal choice for exploratory studies with no priori hypothesis. VBA in diffusion MRI is in general very useful but also limited.

Similar as voxel-based morphometry (VBM) [118, 119], valid conclusions using VBA approach depends greatly on good alignments of brain structures by spatial registration and the choice of kernel width for spatial smoothing [120–123]. On one hand, a perfect spatial registration should not only resolve topological variabil-

ities but also perform exact alignments of the fine structures. However, this kind of spatial registration is often not guaranteed in reality [124–126]. For example, the differences in ventral size between groups may introduction bias into spatial alignments and therefore may introduce false-positive results. Simon et al [113] found that the changes in FA may be due to the differences in ventral size when they examined the changes in the brains of chromosome 22q11.2 deletion syndrome children. On the other hand, smoothing is often performed to reduce the effects of misalignments and improve the sensitivity to abnormalities if the kernel width of smoothing is chosen right to the extent of the structure of interest. However, the choice of the smoothing kernel width is often arbitrary and has been found to have impact on the final results [126, 127]. Moreover, the smoothing introduces another issue - the increasing of effective partial volume, especially in the voxels that are localised at the interfaces of different tissue types.

The whole brain searching in VBA is ideal for exploratory studies but this wide spatial extent may bring up issues such as reducing the statistical power. Due to the expenses of MRI scans and the accessibility of MRI scanners, modern MRI studies usually have only tens or hundreds of participants. Compared with the tens of thousands of voxels that we perform group comparisons or correlation analysis, this is rather limited and the localised subtle changes may not be picked up after correcting multiple comparisons.

2.4.2 Tract-based spatial statistics (TBSS)

To deal with those issues in VBA analysis, a fully automated voxel-wise approach - Tract-based spatial statistics (TBSS) [128] was proposed in 2006. It combines both the advantage of automated whole brain searching in VBA and the anatomical specificity in tractography and has been one of the most popular approaches since then. In TBSS, all the statistical analyses are limited on the ”white matter skeleton”. White matter skeleton is identified by searching for the centres of all white matter fiber bundles that are common across the subjects in the cohort of a study. The main steps of TBSS are:

- Step 1: Create the group-specific white matter skeleton using the skeletonized

map of the average FA image in the common space.

  - Align FA maps of all subjects to a common target using nonlinear spatial registration.
  - Create the group mean FA map of all aligned FA maps.
  - Apply a "thinning" procedure to the group mean FA image (no maximal suppression perpendicular to the relevant tract) and mask out those areas with low FA values and/or high individual variability of FA values. The final "skeletonized" group mean FA map is the group-specific white matter skeleton.

- Step 2: Create the "skeletonized" FA map for each subject by projecting each aligned FA map onto the group-specific white matter skeleton.

  The voxels with the highest FA value are considered as the local centers of the white matter tract, and therefore this step searches for the maximum FA value in the perpendicular direction of the nearest relevant tract on the group-specific skeleton. For each subject, all the voxels on the skeleton are valued as the same FA values from the respective local center of the nearest relevant white matter tract. The same projection is applicable for other DTI metrics, such as MD, AD and RD. By the end of this step, the "skeletonized" diffusion MRI metric maps are created.

- Step 3: Perform voxel-wise statistical analysis across subjects on the group-specific white matter skeleton.

2.4.3 Tractography

By integrating the direction information of each voxel, tractography, which is also referred to as "fiber tracking", reconstructs the 3D white matter tracts that connects different brain areas (see [129] for a review). The fiber directions in each voxel are estimated by diffusion MRI models and fiber tracking is a process of drawing streamlines between cortical/subcortical structures.

A typical fiber tracking algorithm usually consists of 4 main steps:

- Identify areas between which the fiber tracking will be performed;
- Place seeds (i.e., starting points for the next step - propagation) within those areas;
- Carry out the propagation (i.e., a process that identifies all the voxels along the tract) and draw streamlines;
- Terminate the propagation.

The areas for fiber tracking can be manually drawn, or defined according to the projections from atlas in other MRI modalities (e.g., $T1$), or whole brain. The seed placement for fiber tracking is usually automated, and the number of seeds is often one or more.

For propagation, two kinds of algorithms are used, deterministic [130,131] and probabilistic fiber tracking [53, 132]. The deterministic fiber tracking reconstructs streamlines that connect brain areas while the probabilistic fiber tracking takes the uncertainty of the estimation of fiber directions into account and provides a probability map of the likelihood that a voxel belongs to a fiber tract. To improve the robustness of the fiber tracking results, a few well-defined criteria to terminate fiber tracking are often used, including the thresholds of minimum FA value and an appropriate step size as well as the turning angle.

2.4.4 ROI analysis

ROI analysis is often chosen for studies with clear hypotheses because it improves the statistical power by decreasing the number of multiple comparisons from tens of thousands of voxels into tens or a couple of ROIs. It also has a relatively higher tolerance of misalignments than VBA [133]. In ROI analysis of diffusion MRI metrics, we compute the representative value/curve such as mean, median or histogram across all the voxels for each ROI. These values/curves in the chosen ROIs are the inputs for the further statistical analysis.

The ROIs can be defined in many ways, such as definitions in the white matter atlas, manually drawing, tractography and so on. The manual delineation of

ROIs is subjective and very time-consuming, and its accuracy greatly depends on the experience and anatomical knowledge of the one who performs the drawing. Tractography has been demonstrated to be able to reconstruct the major white matter bundles. However, its accuracy is still under debate [134, 135]. Anoter choice is to define ROIs based on a white matter atlas. White matter atlases are often created by experts with a good knowledge of the neuroanatomy. Therefore, an atlas-based approach should theoretically minimise the potential impact of the knowledge of the one who defines the ROI on the final results and improves the comparability of findings across studies. However, this approach involves a registration step between the white matter atlas and the diffusion MRI metric maps. The accuracy of this step is key on the validity and reproducibility of the results.

Chapter 3

White matter in neurodegenerative diseases: An overview

3.1 White matter in the human brain

White matter in the brain refers to the fibre tracts that link cortical and subcortical brain areas, and mainly consists of glial cells and axons with or without myelin.

3.1.1 White matter microstructure

From a MR imaging point of view, the white matter microstructure in a voxel is composed mainly of axons and the intra-axonal structure, myelin, glia cells, extracellular space, and the vascular system (illustrated in Figure 3.1).

3.1.1.1 Axons

Axons in white matter connect to somas in cortical and subcortical regions, and play an important role in brain function.

One important axonal feature is its diameter, and the relationship between the axon diameter and the signal transmitting speed can be approximately considered as linear [138]. That is to say, the larger the axon diameter is, the faster the signals will transmit. Ideally, the more the axons with large diameters are in the human, the faster the signal transmission will be. However, due to the constraints of biological factors such as brain volume and energy supply, human brain is not mainly constituted by giant axons but instead small axons [139]. In the human brain, axon diameter ranges from 0.1 um to 10 um [140]. Myelinated axons often have a diam-

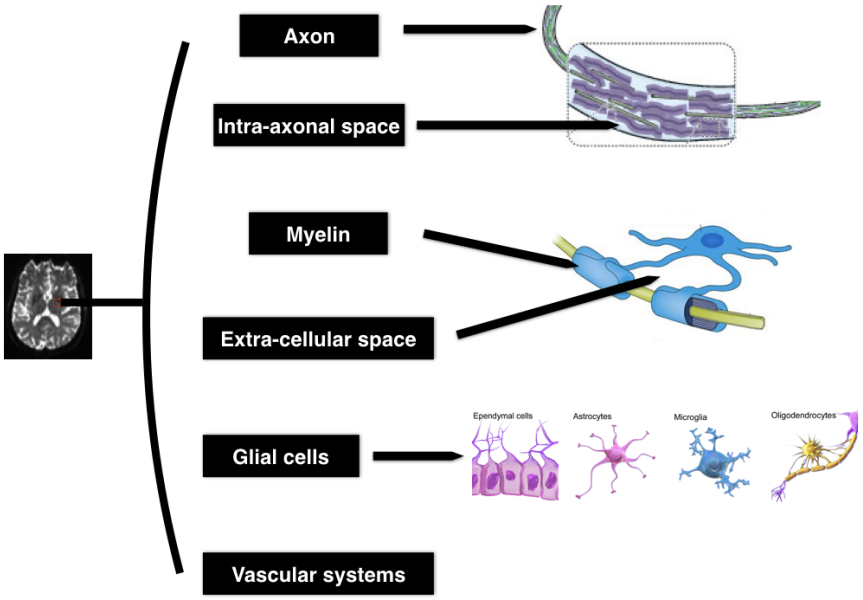

Figure 3.1: An illustration of the microstructure in a voxel of human brain white matter from a view of MR imaging. Elements were adapted from [136] and [137]

eter that is more than 0.2 um, and a small number of giant axons with a diameter bigger than 3 um have been found in fiber tracts such as corpus callosum [141, 142] and corticospinal tract [143]. Interestingly, there is a variation of axon diameter even within the same tract. For example, previous studies found that the middle body of corpus callosum have a large diameter than the genu of corpus callosum. Moreover, the axons in its splenium occasionally have the largest diameter but often have the smallest mean value of the diameter [141, 142, 144, 145].

Another important morphological feature is the density of axons. The decrease in axon density has been found to be related with ageing [146] and neurodegenerative diseases such as multiple sclerosis [147] and AD [148]. In addition, the spatial organisation of axon alignments may carry information about disease pathology [149]. For example, the histological measures in a recent study showed that MS patients had a reduced variability of axon orientations in the white matter of the spinal cord compared with controls [107].

3.1.1.2 The intra-axonal space

The membrane of axons form a unique intra-axonal space [14]. In this space, there are proteins, macromolecules, filaments and mitochondria. Filaments maintain the shape and the internal organisation of the axons [150]. The microtubules are the structures that support the material transportation from the cell body to the axon terminals [150].

3.1.1.3 Myelin

Myelin refers to the sheath that wraps around the axons with a thickness of about 10 nm [14]. It consists of 80 percent lipids and 20 percent proteins [14]. The segments of myelinated axons repeat at a length of about 12 nm [151], and the gaps between those segments are known as "nodes of Ranvier" [152].

In neural tissue, myelin supports a fast transportation of information along the axons [138]. Notably, not every axon in the brain is myelinated. For example, only about 30% of the axons in the corpus callosum have myelin [153]. Compared with unmyelinated axons, myelinated axons are to a higher degree, physiologically specialized [153].

3.1.1.4 Glial cells

Glial cells are the non-neuronal cells in central nervous system. They do not produce action potentials, and provide support to neural activities [154]. However, this view has been shifted as it has been found that astrocytes, one subtype of glial cells, have a key role in modifying the synapses in the brain [155].

In the central nervous system, there are various glial cell subtypes, including microglia and macroglia (astrocytes, oligodendrocytes, ependymal cells, and radial glia) [136]. Microglia are immune cells that protect the brain against diseases. As for the macroglial cells, astrocytes have a unique star shape and maintain the working environment of neurons, especially synapses; oligodendrocytes are the producers of the myelin; ependymal cells are involved in the processing of creating CSF; radial cells are the "stem cells" in the brain that can create neurons and provide a scaffold for neurons to radially migrate in the cortex (see [136] for more

information).

3.1.1.5 Extra-cellular space

Extra-cellular space, as the name suggests, refers to the space outside the cells. The fraction of this space was reported to be 15-35% in the non-human adult brains using invasive microscopy techniques [156]. However, the techniques available are invasive and always involve a process of fixing neural tissue, which often introduce tissue shrinkages [141, 142, 145, 157]. Therefore, there is still no accurate way of measuring the volume of this space until now.

3.1.1.6 Vascular system

There are three kinds of vascular system in the brain, including veins, arteries and capillaries [14]. They can produce an effect of water-dispersion similar as water diffusion. This effect is more rapid than water diffusion, and can be measured non-invasively by a technique "intravoxel incohorent motion imaging" [158].

3.1.2 White matter tracts

White matter tracts in the brain have been popularly classified into 3 groups - commissural fibers and association fibers as well as projection fibers according to their origins and terminals [159]. This approach was first proposed by a psychiatrist - Theodore Meynert at the second half of the 19th century [160].

3.1.2.1 Commissural fibers

Commissural fibers refer to those that connect the brain areas between the two hemispheres, and include corpus callosum and anterior commissure as well as posterior commissure [159]. Take corpus callosum as an example. It is the biggest fiber bundles in the brain, and carries the major information exchange between the two hemispheres.

3.1.2.2 Association fibers

Association fibers are the white matter connections within each hemisphere [159]. Based on their length of the subcortical course and the origins and terminals, we can further divide them into short fibers - U-shape fibers and long fibers - long

association bundles. U-shape fibers are the connections between gyri in the near neighbourhood. In contrast, long association bundles connect gyri in a more widely distributed space. For example, superior longitudinal fasciculus connects the frontal and occipital lobes.

3.1.2.3 Projection fibers

Projection fibers consist of afferent and efferent fibers that connect cortical areas with subcortical structures and the spinal cord [159]. For example, the white matter fibers connect the thalamus and the cortex.

3.2 White matter pathology in neurodegenerative diseases

3.2.1 Neurodegenerative diseases

Neurodegeneration refers to the phenomenon that the neurons in the nervous system suffer from structural and/or functional losses observed in neurodegenerative diseases [161]. Neurodegenerative diseases often occur from middle to later stages of life, and include progressive neurological disorders with heterogeneous clinical and pathological expressions [162].

In the last couples of years, neurodegenerative diseases have caused great physical and financial burdens of patients, their families and to society. For example, in Europe, there are approximately 7 million people with dementia, and the cost of caring for them is about 130 billion euros per annum [163]. The situation is becoming worse, as this population with dementia is expected to double every 20 years [163]. Sadly, there is still no effective solution to halt or slow down the progression of such neurodegenerative processes.

Neurodegenerative diseases include dementia (its most common type - Alzheimer′s disease, (AD)), Parkinson′s disease (PD), Huntington′s Disease (HD) and so on. Although they have clear differences in the clinical symptoms and the pattern of disease progression, they seem to share some common neurodegenerative pathology, such as synapse loss [164], abnormal axonal transport [165, 166]

and so on. Such neuropathology might be caused by abnormal aggregations of disease-specific mis-folding protein (see [162] for a review).

So far, the causes of these neurodegenerative diseases are not still well understood. However, genes do play a role in the pathogenesis of neurodegenerative diseases [1]. HD is caused by abnormal CAG trinucleotide repeats in the HTT gene [167]. The discovery of this HTT gene has motivated researchers in this field to identify genes that cause the neurodegenerative diseases (see [1] for more about the story). For AD, there are 3 fully-penetrant genes (APP, PSEN1, and PSEN2) that have been shown to be implicated in the disease [168, 169], and one risk factor - APOE $\varepsilon 4$ [170]. Multiple genes are also associated with the development of PD [171].

Here, my work focused on the two characteristic neurodegenerative disease - young onset AD (YOAD) and Huntington's Disease (HD). The pre-manifest stage of HD individuals can be identified by predictive genetic testing years before the clinical onset [167]. Therefore, pre-manifest HD is an ideal candidate to represent the preclinical stage of neurodegenerative diseases. AD is the most common type of dementia, and has been studied extensively so far. According to the age at the disease onset, AD can be grouped into YOAD (also referred as early onset AD) and late onset AD (LOAD). The disease progression in YOAD was found to be faster than LOAD [172–174]. This makes YOAD a better disease model than LOAD for our exploratory study on testing the feasibility of NODDI in tracking the longitudinal progression of white matter pathology over a relatively short period of time. The following sections give a brief introduction to the selected disease models.

3.2.1.1 Huntington′s disease

HD is an autosomal dominant inheritance disease, and its occurrence in western countries is about 10.6-13.7 cases per 100, 000 [175]. More than 36 CAG trinucleotide repeats in the HTT gene largely increases the risk of developing HD in the adulthood [176]. And more than 39 CAG repeats means a fully penetrant onset for human beings [175].

The onset of HD often occurs at the middle or late stage of life (Figure 3.2).

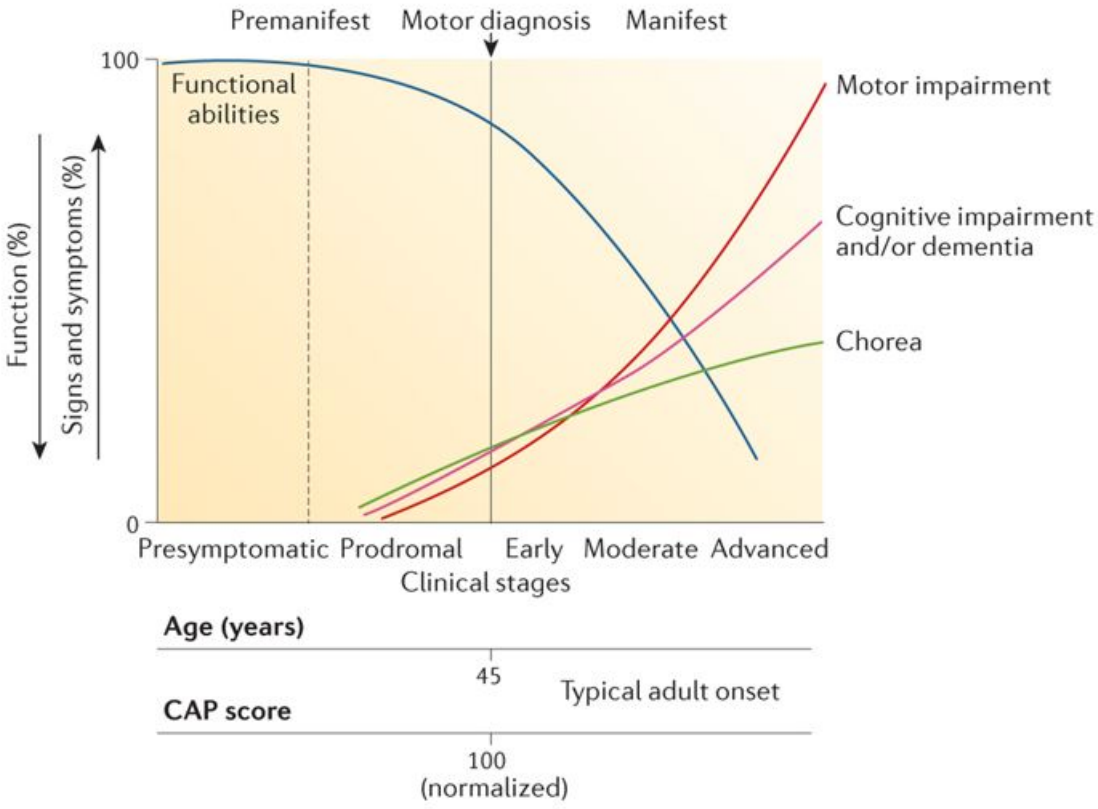

Figure 3.2: The clinical history of Huntington′s disease (adapted from [167])

HD patients have characteristic atrophy in the subcortical nuclei of the brain, including caudate, putamen, globus pallidus and nucleus accumbens [175]. Clinically, HD patients exhibit a combination of motor, cognitive and behavioural symptoms [167,175]. Movement disturbance in HD is characterized by chorea, the occurrence of which is often regarded as the criteria of the clinical onset [167]. Cognitive dysfunctions in HD include impairments to recognition of emotion, visuospatial and executive function, visual working memory, processing speed, and smell identification [177–180]. Neuropsychiatric symptoms in HD are various, including apathy (most common, 28% occurrence), anxiety, irritability, depression, obsessive compulsive behaviours and pyschosis [180–183].

3.2.1.2 Young onset Alzheimer′s disease

AD is the most common type of dementia, and its incidence is about 1-3% in the aging population that is over 65 years old [184–187]. AD can be caused by the

abnormal mutations of gene - APP, PSEN1, or PSEN2, known as familial AD [188]. However, familial AD is relatively rare and the majority of AD patients belong to sporadic AD [188].

The onset of AD often occurs at a mean age of about 80 years old (Figure 3.3), caused by the abnormal accumulations of Aβ proteins in the brain [189]. The brain atrophy in AD patients often starts from the frontal and temporal lobes, and then progresses to the rest of the brain [189].

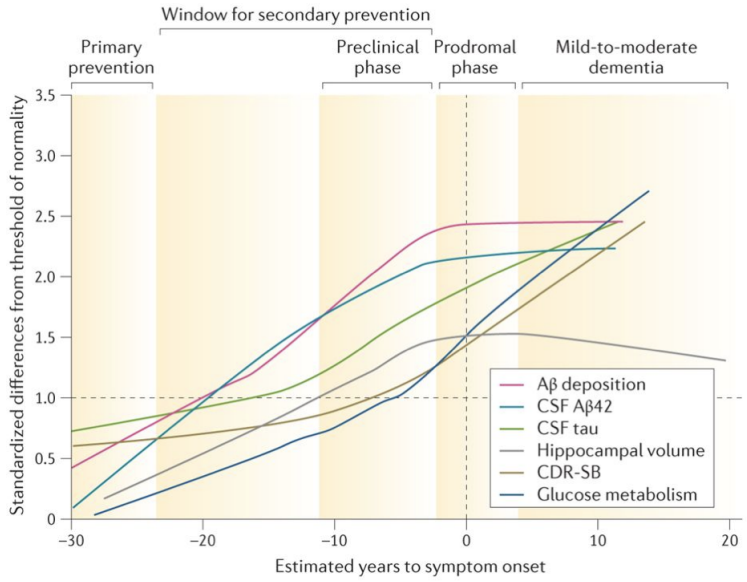

Figure 3.3: The clinical history of Alzheimer′s disease (adapted from [189])

Conventionally, the clinical diagnosis criteria for YOAD is that patients have the clinical onset of AD before the age of 65 years old [190]. Typically, YOAD patients have less vascular brain damage compared with LOAD patients but a heavier burden of neurofibrillary tangles, synapse loss, and neurite plaques [191].

3.2.2 White matter pathology in neurodegenerative diseases

The axonal pathology in white matter that is responsible for triggering the onset of neurodegenerative diseases has been demonstrated to emerge decades before the signs of clinical symptoms [192, 193]. Especially, the abnormal axonal transport has been identified to be a feature shared by a variety of neurodegenerative diseases [165, 166, 194], including AD [195, 196], HD [197], Parkinson's disease [198] and

so on.

Axonal transport refers to the transportation of materials between cell bodies and synaptic terminals via the cellular cytoskeleton of axons [199]. In neurodegenerative diseases, the abnormal accumulations of proteins have been proposed to be an early toxic marker of the disease pathology [194]. And these proteins disrupt the fast axonal transport, which is one of the essential processes for the survival of neurons [194].

In **HD**, the cellular pathology relevant to the abnormal axonal transport are the disruptions of both anteorgrade and retrograde transport [197] as well as axonal swellings [200]. In **AD**, the relevant cellular pathology include the disruption of anterograde transport [201] and the axonal blockage [202] (see [166] for more details on axonal transport in neurodegenerative diseases and the relevant cellular pathology). These evidences highlight the importance of studying and monitoring the progression of white matter pathology in neurodegenerative diseases.

3.2.3 Diffusion MRI in studying the white matter abnormalities in neurodegenerative diseases

In the last few years, a lot of attention has been paid to studying white matter abnormalities in neurodegenerative diseases. Especially, diffusion MRI techniques, which provide valuable information on the *in vivo* microstructural configurations via measuring water diffusion non-invasively, have been widely used in clinical neurodegenerative studies [203].

There are a lot of reviews on the role of diffusion MRI in studying impaired white matter in neurodegenerative diseases, such as detecting abnormal white matter (see [204–208] for reviews), identifying impaired connectivity (see [209, 210] for reviews), evaluating altered organisations of brain network (see [167, 211–214] for reviews), providing potential markers for clinical diagnosis and predicting the long-term outcomes [215–220] and so on.

More specifically, in **pre-manifest HD**, diffusion MRI studies have identified increased diffusivity and decreased FA in CC, internal/external capsules, cingulate, thalamic radiations, cerebral peduncles, fronto-occipital fasciculus, cortico-striatal

tracts and fronto-thalamic tract [221–225]. In **AD**, diffusion MRI studies found increased diffusivity and decreased FA in the temporal, parietal and frontal white matter, the corpus callosum and the longitudinal association fiber tracts [226–230]. The longitudinal changes in DTI metrics of AD have been found over time in the fornix, corpus callosum, inferior cingulum, hippocampal cingulum, internal and external capsule, corona radiata, posterior thalamic radiation, superior and inferior longitudinal fasciculus, fronto-occipital fasciculus, tapetum and uncinate fasciculus [231–234].

Chapter 4

Image acquisition, preprocessing, image analysis in a clinical study using diffusion MRI

This chapter aims to cover the key imaging factors to be considered when designing and performing a clinical study using NODDI and DTI (illustrated in the flowchart of Figure 4.1). The first section discusses about acquisition protocols and the importance of pre-testing the protocols. The second section describes the key steps of imaging processing used in all our studies - from image quality control to the quantitative analysis of diffusion MRI metrics.

4.1 Image acquisition

A successful MRI acquisition depends on a lot of factors. This section focuses on the optimised acquisition protocols for NODDI and DTI first and then the importance of performing pre-testing for MRI scans.

4.1.1 Protocol design

The diffusion properties of the brain measured by MRI could fully reflect the microstructural configurations when measured with a high diffusion gradient along all possible directions in 3D space. This demands a long scan time, which is not only expensive but also infeasible for human participants. Therefore, for clinical studies, it is important to optimise the parameters of the acquisition protocol so that a

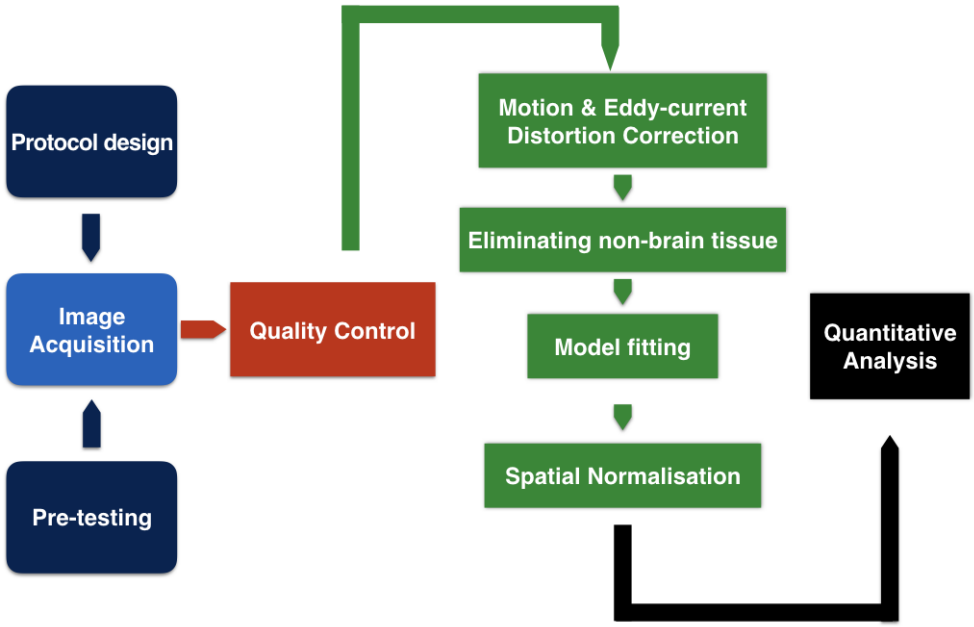

Figure 4.1: The flowchart of the steps in an imaging study

relatively small collection of diffusion MRI measurements within a tolerable scan duration could provide a good estimation of diffusion MRI metrics.

The key parameters of a diffusion MRI protocol are diffusion weighting factor (b value), the number of diffusion weighted non-colinear directions, the duration of the gradient pulses (δ), the diffusion time (Δ), TR/TE, Field of View (FOV), image resolution, and the total acquisition time.

The selected b value in **DTI** studies typically ranges from 700 to 1000 s/mm^2, and the standard b value for DTI acquisition in clinical studies is 1000 s/mm^2 [235]. Theoretically, the estimation of a 2nd-order tensor requires an acquisition with at least one image without diffusion weighting (b= 0 s/mm^2) and 6 non-colinear diffusion weighted directions. However, a number of simulation studies showed that using more than 6 directions could not only reduce the errors of the estimated DTI metrics [236, 237], but also improve the accuracy of the estimated principle direction of DTI for fiber tracking [238–244]. In vivo human brain data also showed the similar improvements of estimating fiber orientation for fiber tracking with more than 6 directions [245]. Accordingly, 30/60/64 non-colinear directions are often

sampled in clinical studies [246]. The typical ranges of TE and TR are 50-70 ms and 8500-12000 ms respectively, and the voxel size is often between 2 mm and 2.5 mm for each dimension in the 3D space. A typical whole brain DTI acquisition takes about 5-10 minutes. For our studies, we chose a DTI protocol that has a b value of 1000 s/mm^2 with 64 non-colinear directions and a resolution of 2.5mm isotropic. The total acquisition is less than 10 minutes.

For NODDI, an acquisition protocol optimised for clinical studies was proposed in its original paper [7] based on a framework for the experiment design diffusion MRI studies [102]. The optimised clinical protocol for NODDI consists of 2 shells (b=711 s/mm^2 with 30 directions and 2855 s/mm^2 with 60 directions, TR/TE= 78/12500 ms) with a resolution of 2mm isotropic, implemented in a Philips 3T scanner with a the $|G|_{max} = 65mT/m$. Its total acquisition time is about 25 minutes. For our study, we used Siemens scanners, and adapted the b values into 700 s/mm^2 and 2000 s/mm^2 with 32 and 64 non-colinear directions respectively. Moreover, as partial volume effect might be worse in ageing and neurodegenerative diseases [6], we added another shell with a b value of 300 s/mm^2 acquired along 8 directions. This might improve the quality of estimating NODDI metrics, especially for FISO, as signals at low b values contain more contributions from the free water diffusion. In order to avoid the contamination from perfusion effects, we did not choose a b value lower than 300 s/mm^2 [247]. Lastly, we used a voxel size of 2.5mm isotropic and the acquisition time is around 15 minutes.

4.1.2 Pre-testing MRI scans

Although MRI scans are expensive, it is of great importance to pre-test the acquisition protocols on one or two subjects and perform image quality control for those datasets before the actual study starts. This is essential to avoid acquiring problematic images with artefacts caused by the incorrect settings of the acquisition protocol.

4.2 Image processing

After MR image acquisitions, image processing follows. The main steps used in our studies consist of: 1) quality control; 2) motion and eddy-current distortion correction; 3) elimination of the non-brain tissue; 4) model fitting; 5) spatial normalisation; 6) quantitative analysis. Each step in the processing pipeline (Figure 4.2) is described in detail later.

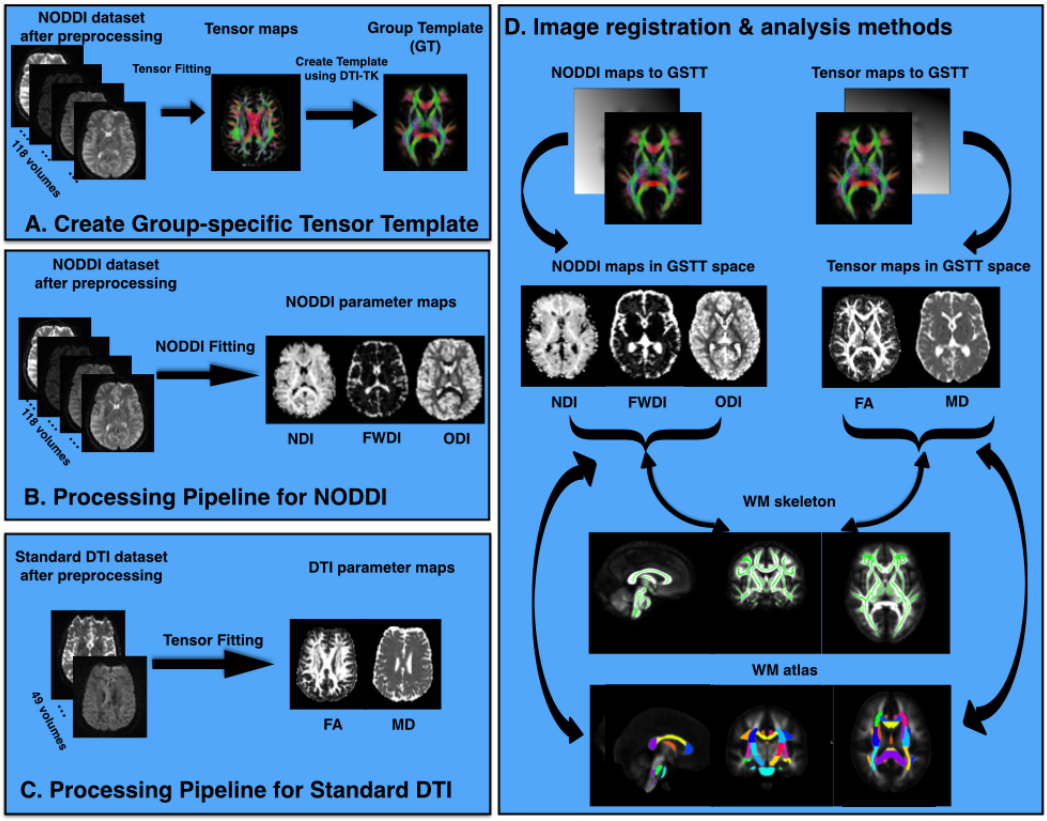

Figure 4.2: An illustration of the image processing pipeline

4.2.1 Quality control

Image Quality Control (QC) is an essential step to ensure that no problematic images with artifacts are included in the image analysis and improve the reproducibility of the findings in a study [248]. A diffusion MRI dataset with good quality usually has proper brain coverage, minimal or no artifacts (see chapter 2.2.2.2), little motion either within a volume or across the images along different diffusion weighting directions, correct tissue contrasts as described in the online tutorial [249]. We

used manual QC methods in all our experiments. QC should be done within one or two days after the MR image acquisition so that if the dataset does not pass the QC - the researchers can either arrange re-scan this participant or recruit new participants. Details on how we check diffusion MR images can be found in an online tutorial [249].

4.2.2 Motion and eddy-current distortion correction

Head motion often brings up mismatching problems, i.e., the coordinates of one voxel may not stay the same throughout the whole dataset.

Eddy-current distortion refer to the unrealistically distorted geometry of the brain introduced by the magnetic gradients caused by time-varying eddy currents, as described in chapter 2.2.2.2. In particular, this distortion is more severe for rapid imaging sequences. As for diffusion MRI, the fast switching of diffusion weighted gradients with high amplitude and long duration produces larger time-varying gradient fields, which interfere with the spatial encoding gradients and therefore introduce bigger geometrical distortion of the brain [39].

Both head motion and eddy-current distortion introduce bias in the estimated diffusion MRI metrics and the final conclusions. Therefore, it is essential to correct for both artifacts before any actual image analysis.

Registering the diffusion weighted images to the b0 images is a popular approach to correct for head motion and eddy-current distortion. However, there is a difference in the signal intensities between b0 images and diffusion weighted images. And this difference may introduce bias into the direct registration between the diffusion weighted images and the b0 images used in the most common used approach - FSL "eddy_correct" [250]. Here, our approach for motion correction was a linear registration using FLIRT [250–252]. We first estimated the affine transformation matrixes by registering each b0 image to the first b0 image. Then we registered every diffusion weighted image to the first b0 image using the transformation matrix estimated for registering its closest b0 image to the first b0 image. This approach was also used in a previous study on NODDI in the spinal cord [253] and has been demonstrated to be the most beneficial for diffusion MRI image processing [254].

To have a better estimation of motion, instead of acquiring all the b0 images in the first or last few volumes, we designed the acquisition of all b0 images in a way that one b0 image is acquired after every 8 diffusion weighted images.

The output transformation matrix by FLIRT is an affine transformation matrix estimated, and equals to "rotation matrix * skew matrix * scale matrix". The rotation matrix describes the rotational motion along the 3 axes, and can be mathematically written as "R_x*R_y*R_z". R_x can be mathematically written as:

$$R_x = \begin{bmatrix} 1 & 0 & 0 & 0 \\ 0 & c_x & s_x & 0 \\ 0 & -s_x & c_x & 0 \\ 0 & 0 & 0 & 1 \end{bmatrix} \tag{4.1}$$

where $c_x = cos(\theta)$, $s_x = sin(\theta)$, θ is the angle that the head rotates away from the head in the reference image along the x axis. R_y and R_z can be represented in a similar mathematical form. The skew matrix can be mathematically written as:

$$\begin{bmatrix} 1 & k_{xy} & k_{xz} & 0 \\ 0 & 1 & k_{yz} & 0 \\ 0 & 0 & 1 & 0 \\ 0 & 0 & 0 & 1 \end{bmatrix} \tag{4.2}$$

where k_{xy}, k_{xz} and k_{yz} are the three skew parameters. As it is a registration between b0 images of the same subject, ideally the scaling matrix here is an identity matrix.

4.2.3 Eliminating the non-brain tissue

The non-brain tissue here refers to those structures such as skull, neck, fat, muscle and so on. Masking out the non-brain tissue is necessary especially for brain segmentation and image registration [255]. In our case, since NODDI fitting using the available matlab toolbox [256] is very time consuming, excluding the non-brain tissue can save a lot of time. This can be quite beneficial, especially for large studies that recruits hundreds and thousands of participants.

In our study, we excluded non-brain tissue using a brain mask created using

the Brain Extraction Tool (BET) [255]. This tool uses an approach that exploits the local intensity changes and is applicable to images acquired with a collection of MRI sequences (T1, T2 and T2*). Notably, BET provides an option to specify the fractional intensity threshold to estimate the brain outline. And I often chose a threshold of 0.15 as the starting one because according to my experience, this threshold often gives a relatively good result for clinical datasets. After finishing running BET, we checked and reassured the coverage of the brain mask. If the mask either does not cover the whole brain or includes too many non-brain voxels, we would adjust this threshold and re-run BET until we think the mask looks fine.

4.2.4 Model fitting

Both NODDI and the tensor model were fitted to estimate the NODDI and DTI metrics respectively using the NODDI Matlab toolbox [256] and FSL [108]. The details of the algorithms for NODDI fitting and DTI fitting were described in chapter 2.3.2.2 and chapter 2.3.1.2. NODDI fitting using this matlab toolbox is time consuming. And it is recommended to plan enough time for the fitting before running the quantitative analysis.

When the fitting is finished, it is important to check the NODDI metric maps, especially for the first few scans in a study. It helps the researchers assess if the settings of the sequences are appropriate.

4.2.5 Spatial normalisation

Spatial normalisation aligns the MRI volumes from their native spaces (in which the MRI images are acquired) into a standard space with standardised coordinates. This allows us to perform quantitative analyses such as group comparisons and identifying the individual variations at both the voxel-wise and ROI levels. In spatial normalisation, a certain volume is often chosen as the target to warp other volumes onto. A popular choice of this target is a template in a standard space (see [257] for a review on the templates available).

Although the standard templates have been extensively used in neuroimage analysis, a study-specific template is demonstrated to be beneficial as it could min-

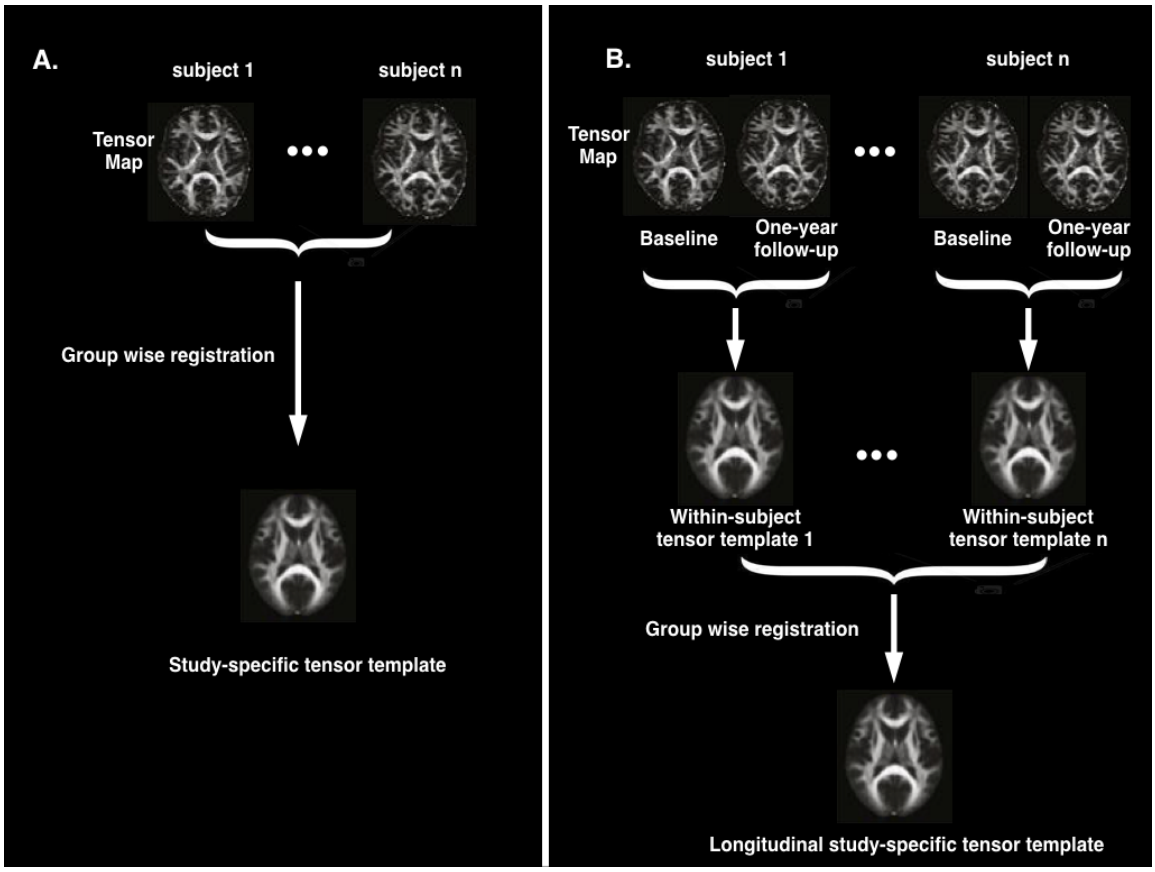

Figure 4.3: The flowchart of spatial normalisation using DTI-TK. A. Constructing the study-specific tensor template for cross-sectional studies; B. Constructing the study-specific tensor template for longitudinal studies.

imise the bias caused by the differences in neuroanatomy between the template and the brain of each individual [258, 259]. The creation of a study-specific template is an iterative process. The first step is usually to initialise the study-specific template by warping all the brain volumes onto a template or a target volume. Then we register all the volumes from the native space onto this initial study-specific template. This process is often repeated again and again until the differences between the template and all the volumes in this study reach a certain threshold. By the end of these iterations, we have created a template that is most likely to reflect the similarities in brain anatomy within the population in the study. This template is often referred to as a study-specific template.

For diffusion MRI, to create a study-specific template, we can use either single-channel information, for example, a FA map [108], or multi-channel information

such as tensor volumes [125], spherical harmonics [260] and so on. The estimation of the spherical harmonics requires high b value datasets, and therefore it is not an appropriate choice for our clinical datasets. Tensor-based registration approaches have been demonstrated to perform better than FA-based registration both cross-sectionally and longitudinally [261, 262]. Therefore, we implemented a tensor-based framework for the spatial normalization using DTI-TK [263, 264] in all our studies as illustrated in Figure 4.2. The template we used for initialising the study-specific template is a template created based on an ageing population "*ixi_aging_template.nii*" [265]. Finally, we warped both NODDI metric maps and DTI metric maps to the template space.

4.2.6 Quantitative analysis

With all the NODDI and DTI metric maps aligned in the template space, we extracted the representative values of NODDI and DTI metrics based on the spatial unit in the following quantitative analyses.

In our case, as all of our experiments are exploratory studies, we first exploited the most popular voxel-wise analysis method - tract-based spatial statistics (TBSS, described in chapter 2.4.2). The white matter skeleton was created based on the mean FA map of the whole cohort. We then projected all the NODDI and DTI metric maps onto the skeleton. To further investigate the clinical relevance of NODDI, we then computed the mean NODDI metrics of selected white matter ROIs defined in the template space and explored the relationship between NODDI metrics and the clinical measures of disease progression or cognitive performances.

As for the statistical analysis, for TBSS, we used "glm_gui" to set up the general linear model for group comparisons while for ROI analysis, we used matlab to set up the general linear model for correlation analysis and group comparisons. Further details were described in the methods of all the following studies.

Chapter 5

NODDI in the pre-manifest stage of Huntington′s Disease

5.1 Introduction

In this chapter, we aimed to evaluate the feasibility of translating NODDI into studying in-vivo white matter pathology at the preclinical stage of neurodegenerative diseases. We also compared NODDI over the standard diffusion MRI technique - DTI in terms of the sensitivity to detecting white matter abnormalities at this stage.

Here, we took pre-manifest HD as a disease example representing the preclinical stage of neurodegenerative diseases. Huntington's disease is a monogenic, neurodegenerative disorder, characterised by motor, cognitive and neuropsychiatric disturbance [266]. As it is both autosomal-dominant and fully penetrant, HD gene-carriers can be identified many years prior to clinical onset via predictive genetic testing [167]. This provides us a window to evaluate the early changes in the brain at the preclinical stage of neurodegenerative diseases.

Studying white matter could greatly shed light on deepening our understanding of the disease pathology. Abnormal white matter volumes have been identified in major white matter bundles of both pre-manifest HD individuals and HD patients using T1-weighted imaging [267–269]. The emergence of such volume loss in white matter at the macrostructural level is likely to be preceded by subtle alterations at the microstructural level. Therefore, studying white matter microstructural

configurations in preclinical stage of HD might enable us to probe much earlier abnormalities due to the neurodegeneration and therefore provide a much earlier picture of the disease pathology in the brain.

DTI has been used to examine white matter microstructural changes in pre-manifest HD participants [167]. Interest has mainly focused on two key metrics of water diffusion at the microscopic level: fractional anisotropy (FA) and mean diffusivity (MD), estimating respectively the extent of directional dependence and the magnitude of water diffusion [13]. Previous studies have shown that in a number of white matter tracts, including the corpus callosum and internal capsule in addition to cortico-striatal white matter tracts, pre-manifest HD individuals had increased MD and decreased FA compared with controls [221–225]. As we described in chapter 2, whilst sensitive to white matter microstructural changes, DTI metrics lack specificity to inform on the underlying cellular sources of these white matter changes and therefore specific disease mechanisms. DTI conflates the effect on water diffusion from multiple sources of tissue microstructure, e.g. axonal density (the packing density of axons) and axonal orientation distribution (the way in which the axons spread in space relative to one another). Thus, though axonal loss has often been suggested as the mechanism underpinning DTI findings in pre-manifest HD studies, it remains unclear whether other alterations, such as changes to patterns of axonal organization may also contribute to such pathologies.

More specific biological features of white matter microstructure can be investigated using more recent advances in diffusion MRI techniques [14]. Most recently, these advances have been made accessible for clinical research with the development of NODDI [7]. NODDI disentangles the heterogeneity of the tissue composition within each voxel by partitioning the MR signal into different components reflecting distinct tissue features: neurite (dendrites and axons) density, their orientation distribution, and free water contamination (e.g. CSF partial volume). Using this approach, changes in axonal density can be distinguished from those in axonal spatial organization, while removing the potentially confounding effect of free water, which increases in areas of tissue degeneration [6]. NODDI has seen widespread

uptake to help ascertain cellular substrate of white matter alterations, including applications to neurological disorders, such as Focal Cortical Dysplasia [270], young onset Alzheimer's disease [271], first-episode psychosis [272] and Parkinson's disease [273], but is yet to be applied in HD.

We hypothesised that 1) NODDI could detect white matter abnormalities in pre-manifest HD individuals compared to normal controls; 2) NODDI could provide a better depiction of white matter pathology in pre-manifest HD than DTI. To test these hypotheses, with a cohort of thirty-eight pre-manifest HD individuals and forty-five controls from the Track-On HD study [274], we quantified group differences of NODDI & DTI metrics over the whole brain white matter using TBSS [128]. To evaluate the clinical relevance of NODDI, within the pre-defined white matter ROIs, we evaluated the feasibility of NODDI to track the disease progression by correlation analysis between NODDI metrics and clinical scores of disease progression, and calculated sample sizes as references for future clinical trials.

5.2 Research dissemination

We presented the preliminary results of this work at the ISMRM 2015. And we then finished analysing the whole cohort and this work has been published on Annals of Neurology.

- Reduced Neurite Density in Pre-manifest Huntington′s Disease Population detected by NODDI, J Zhang, S Gregory, RI Scahill, A Durr, DL Thomas, S Lehericy, G Rees, SJ Tabrizi, H Zhang, TRACK-ON HD investigators, International Society for Magnetic Resonance in Medicine, 2015.

- *In vivo* characterisation of white matter pathology in pre-manifest Huntington′s disease. J Zhang*, S Gregory*, RI Scahill, A Durr, DL Thomas, S Lehericy, G Rees, SJ Tabrizi, H Zhang, TRACK-ON HD investigators, Annals of Neurology, 2018 (* joint first author)

5.3 Methods

5.3.1 Participants

40 pre-manifest HD gene-carriers and 52 controls were recruited at two HD research centres (one in Paris and the other in London) as part of the Track-On HD study. Pre-manifest HD subjects had a Unified Huntington′s Disease Rating Score (UHDRS) Total Motor Score (TMS) [275] of <5; a diagnostic confidence score of <4, and were required to have a CAG repeat length no less than 40 and a disease burden score (DBS) [276] greater than 250 at recruitment. Controls were spouses or gene-negative siblings of the pre-manifest HD gene carriers. The exclusion criteria for both groups included manifest disease, age below 18 or above 65, major psychiatric, neurological or medical disorder or a history of severe head injury. For further details, see previous work [274]. Cumulative probability to onset (CPO) [277] and TMS were assessed by experienced clinicians and used as clinical measures of disease progression. The local ethics committee approved this study and each participant signed written informed consent.

5.3.2 Diffusion MR image acquisition

Participants were scanned using the same type of 3T Siemens Trio scanners in both centres. A twice-refocused spin-echo echo-planar imaging sequence was used to minimise the eddy-current distortions for both NODDI and DTI acquisition.

5.3.2.1 The NODDI acquisition

The NODDI protocol is: multiple b-values (2000, 700 and 300 s/mm^2) with 64, 32 and 8 non-colinear diffusion-encoding directions respectively; 14 b=0 s/mm^2 images; voxel size=$2.5\times2.5\times2.5$ mm^3; TR/TE = 7000 ms/ 90.8 ms; 55 slices; acquisition time about 15 mins.

5.3.2.2 The DTI acquisition

The DTI protocol is: a b-value of 1000 s/mm^2 and 42 non-colinear diffusion-encoding directions; 7 b=0 s/mm^2 images; voxel size=$2\times2\times2$ mm^3 isotropic; TR/TE = 13100 ms/ 88 ms; 75 slices; acquisition time about 9.5 mins.

5.3.3 Preparations of NODDI and DTI metric maps

The NODDI and DTI metric maps were computed in the way as we listed in Chapter 4. We did 1) quality control of the image datasets; 2) motion and eddy-current distortion correction; 3) exclude non-brain tissue by creating a brain mask and check whether the mask covers the brain properly; 4) model fitting for both NODDI and DTI; 5) registration of each subject into the group-specific tensor template using DTI-TK [263].

5.3.4 Statistical analysis

5.3.4.1 The general linear model for group comparison

We used a general linear model (GLM) for group comparison. The dependent variable is the NODDI/DTI metric of either each voxel on the white matter skeleton or each ROI. The main factor is the group type, "Pre-HD" standing for pre-manifest HD individuals and "NC" standing for normal controls. We includes age, gender and scan site as covariates. For continuous variables like age, we demeaned the variable and converted into a vector. For categorical variables - gender and study center, we used 0 to represent male and 1 to represent female, and used 0 to represent the research centre in London and 1 to represent that in Paris.

5.3.4.2 TBSS Analysis

As designed in Chapter 4, we used TBSS to identify whole brain white matter microstructural changes using NODDI in pre-manifest HD compared to the controls. We created white matter skeleton from the group mean FA map in the template space with the default FA threshold (0.2). We then projected NODDI and DTI metric maps onto the skeleton.

After map projection, we used a non-parametric analysis for group comparison - permutation test, and we set up the GLM as we described in section 5.2.4.1. The permutation was performed 5000 times [278] and multiple comparisons were corrected at $p<0.05$ using Threshold-Free Cluster Enhancement (TFCE) [279]. We also performed the same TBSS analysis of group comparisons between pre-manifest HD individuals and controls using DTI.

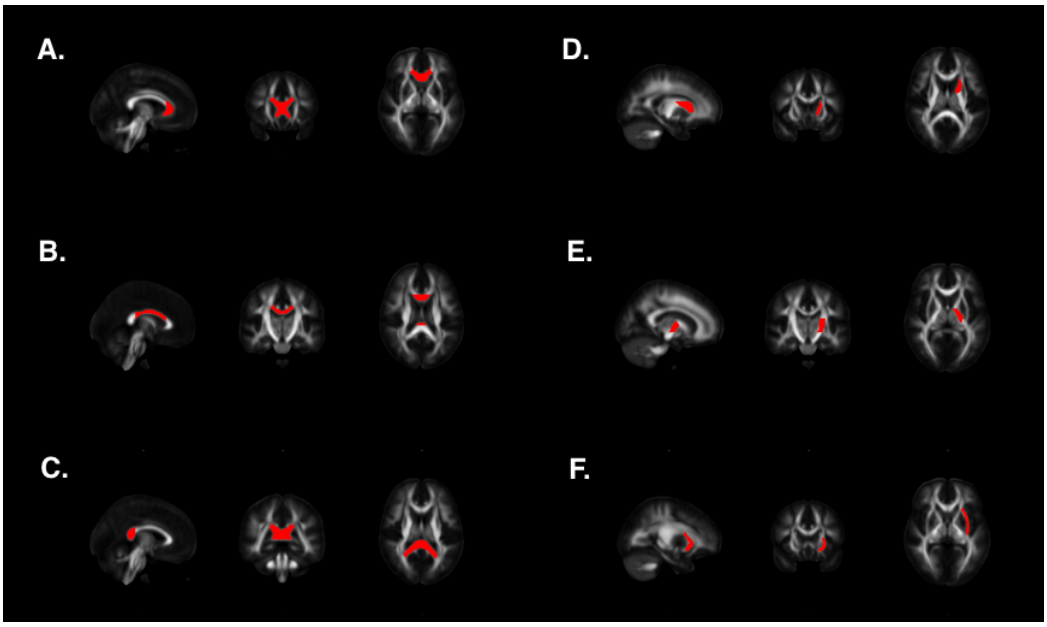

Figure 5.1: White matter ROIs defined in the ICBM-81 white matter atlas. A. Genu of the corpus callosum; B. Body of the corpus callosum; C. Splenium of the corpus callosum; D. Anterior limb of the internal capsule; E. The posterior limb of the internal capsule; F. The external capsule.

5.3.4.3 ROI Analysis

To reveal descriptive statistics of NODDI metrics in white matter, complementing TBSS analysis, ROI-based analysis was performed for a set of key white matter tracts chosen a priori according to the literature (corpus callosum (genu, body, splenium); internal capsules (anterior and posterior limbs); external capsules) [221, 222, 225, 280]. The ROIs for these tracts are presented in Figure 5.1. ROIs were defined by warping the ICBM-81 white matter atlas [281] to the FA map of the group tensor template using NiftyReg [282], as described in Chapter 4. To minimize partial volume effects, ROIs were defined by thinning the mask of each white matter ROI in the atlas by $1mm$.

Group comparison

To increase the statistical power, the bilateral internal/external capsules were analyzed jointly. The general linear model used for group comparison of mean NODDI metrics in white matter ROIs is the same as that in TBSS. The multiple comparisons were corrected using False Discovery Rate at $p < 0.05$.

Correlation analysis

Among the ROIs with significant group differences, we evaluated the value of NODDI metrics in tracking disease progression using Pearson correlation analysis. Correlations between the NODDI metrics and the clinical scores of disease progression (CPO and TMS) were considered as significant if $p<0.05$.

Sample size estimation

The estimation of sample sizes for future clinical trials using NODDI were calculated (using matlab) with 80% power and 5% 2-tailed significance of group difference using NODDI metrics of ROIs (chosen based on statistical significance in ROI-based group comparisons).

5.4 Results

5.4.1 Demographics, Number of CAG Repeats and Clinical Scores of HD Disease Progression

	Controls	Pre-manifest HDs	Statistics
N	45	38	N/A
Age, mean±std (range)	49.1±10.8(28-69)	44.3±8.6(28-70)	p=0.03
Gender, Female/Male	27/18	17/21	n.s.
Site, London/Paris	20/25	18/20	n.s.
CAG repeats	N/A	42.9±1.9(40-47)	N/A
CPO	N/A	0.30±0.18 (0.06-0.75)	N/A
TMS	N/A	6.40±3.85 (0-15)	N/A

Table 5.1: The demographic summary of Controls and Pre-manifest HD individuals. N/A = non applicable. n.s. = not significant.

Following the assessments of controlling image quality, 38 pre-manifest HD and 45 control participants were included in the final statistical analysis. The summary of the demographics and numbers of genetic mutation as well as clinical

scores of HD disease progression (CPO and TMS) were listed in Table 5.1. Pre-manifest HD individuals and normal controls were matched for gender and site but pre-manifest HD individuals were younger than controls ($p<0.05$).

5.4.2 Group differences detected by NODDI using TBSS analysis

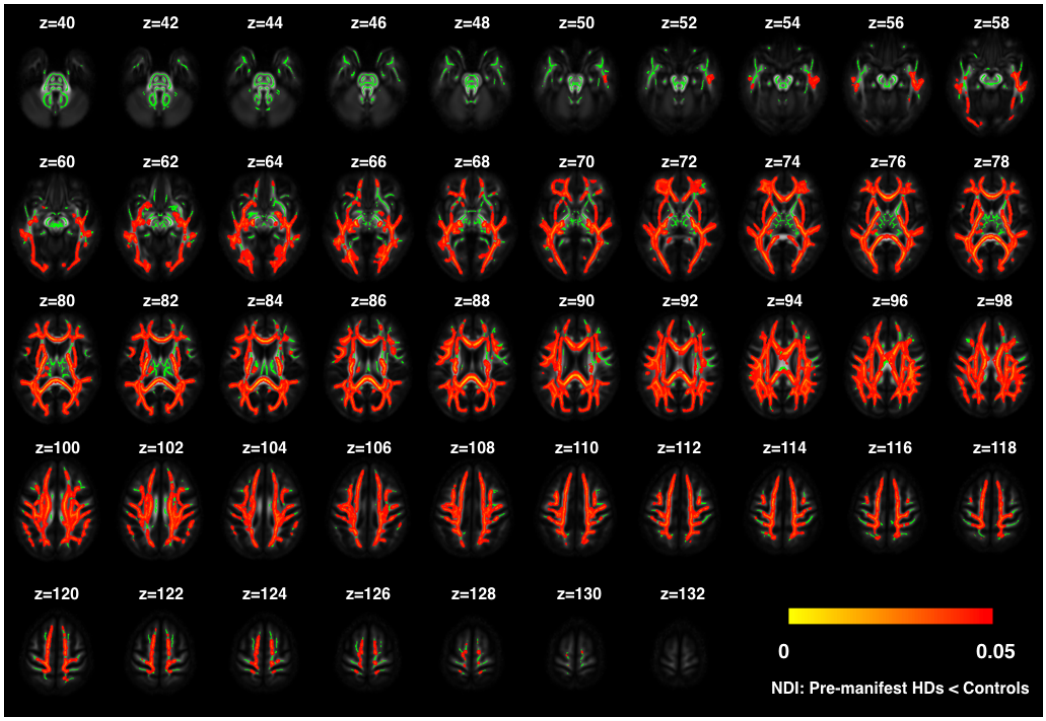

Figure 5.2: Whole brain white matter abnormalities in pre-manifest HD detected by NDI using TBSS, TFCE corrected, $p<0.05$

The whole-brain white matter analysis of NODDI metrics revealed that compared with the controls, pre-manifest HD gene-carriers showed a) reduced axon density in widespread white matter areas indicated by NDI, including the corpus callosum, bilateral superior longitudinal fasciculus, the posterior limb of internal capsule, external capsule, posterior thalamic radiation, middle cerebellar peduncle, corona radiation, uncinate fasciculus and the posterior cingulum (Figure 5.2, TFCE corrected $p<0.05$) and b) altered axonal organization in localized white matter surrounding the basal ganglia indicated by ODIs, including anterior limbs of the internal capsule bilaterally, external capsule, and right retrolenticular part of internal capsule) (Figure 5.3, TFCE corrected $p<0.05$). There were no significant

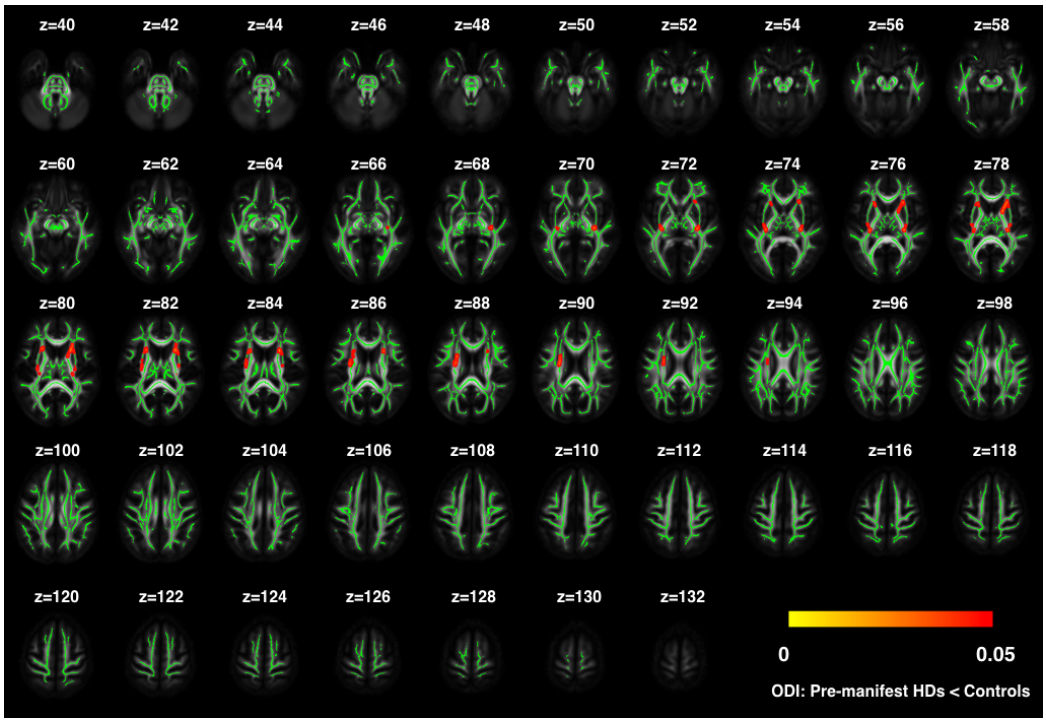

Figure 5.3: Whole brain white matter abnormalities in pre-manifest HD detected by ODI using TBSS, TFCE corrected, $p<0.05$

differences in FISO (TFCE corrected $p<0.05$).

With a stricter threshold of significance $p<0.01$, group differences in NDI still survived (Figure 5.4) but not ODI.

5.4.3 Group differences detected by DTI using TBSS analysis

The whole-brain white matter analysis of DTI metrics revealed that compared with controls, pre-manifest HD group had 1) reduced FA predominantly in the corpus callosum, superior longitudinal fasciculus, and posterior corona radiata bilaterally compared to controls (Figure 5.5, TFCE corrected $p<0.05$); 2) increased MD, including the corpus callosum, bilateral superior longitudinal fasciculus, the posterior limb of internal capsule, external capsule, posterior thalamic radiation, middle cerebellar peduncle, corona radiation, uncinate fasciculus and the posterior cingulum (Figure 5.6, TFCE corrected $p<0.05$); 3) increased AxD, including the external capsules, the right cerebellar peduncle, the corpus callosum, the posterior thalamic radiations, the right uncinate fasciculus and corona radiata (Figure 5.7, TFCE corrected $p<0.05$); 4) increased RD, including the corpus callosum, the left posterior

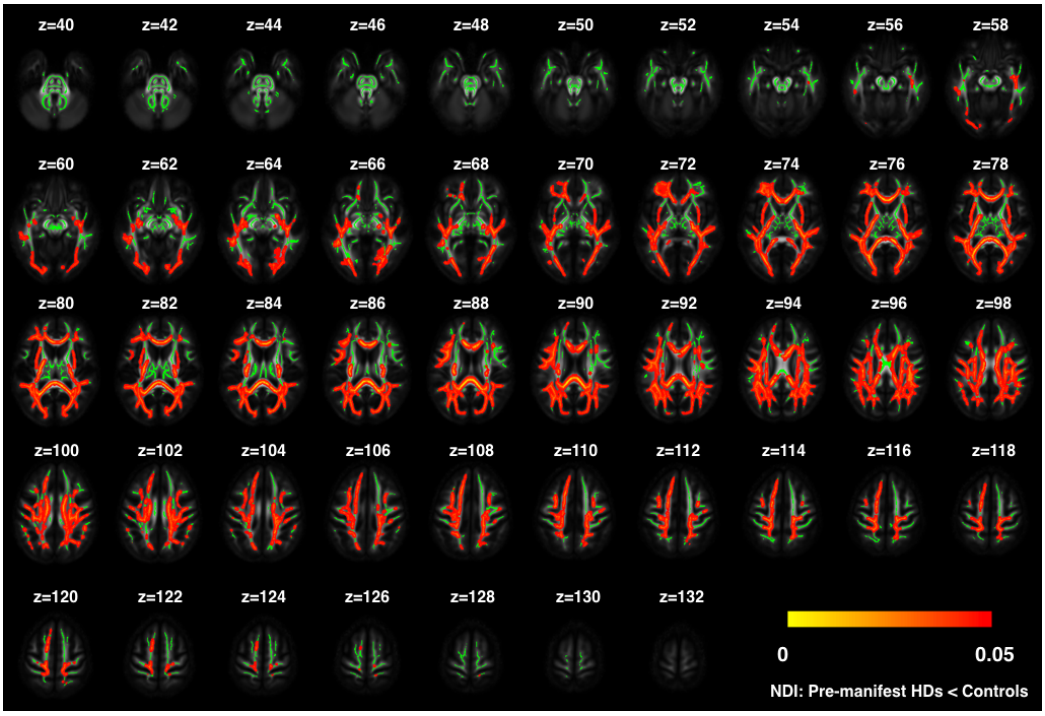

Figure 5.4: Whole brain white matter abnormalities in pre-manifest HD detected by NDI using TBSS, TFCE corrected, p<0.01

limb of internal capsule, the left middle cerebellar peduncle, the left uncinate fasciculs, the bilateral superior longitudinal fasciculi, the bilateral corona radiata (Figure 5.8, TFCE corrected p<0.05). There was no decreased in diffusivities or increase in FA. (TFCE corrected p<0.05)

With a stricter threshold of significance p<0.01, none of group differences in DTI metrics survived.

5.4.4 Group differences detected by NODDI using ROI analysis

In line with the whole-brain findings, ROI analyses showed that pre-manifest HD gene-carriers had a) decreased NDI in the splenium, body and genu of the corpus callosum, posterior limb of the internal and external capsules and b) decreased ODI in the anterior limb of internal compared with controls (Table 6.2, FDR corrected p¡0.05). No ROIs showed significant FISO group differences.

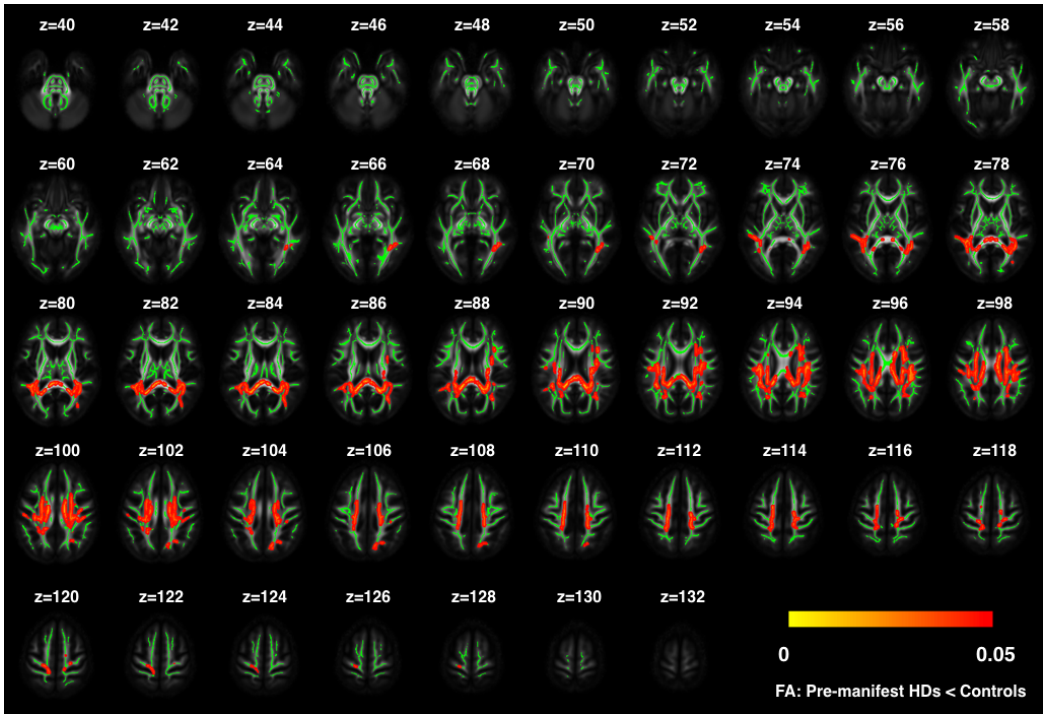

Figure 5.5: Whole brain white matter abnormalities in pre-manifest HD detected by FA using TBSS, TFCE corrected, $p<0.05$

Table 5.2: NODDI metrics of white matter ROIs selected in pre-manifest HDs and controls (FDR corrected, $p<0.05$), specifically a) ROIs with NDI group differences; b) ROIs with ODI group differences.

a) NDI (mean±std)			
WM ROIs	Pre-manifest HD	Controls	Statistics
Genu of corpus callosum	0.53±0.05	0.56±0.04	p<0.000
Body of corpus callosum	0.58±0.05	0.60±0.04	p=0.026
Splenium of corpus callosum	0.60±0.04	0.63±0.03	p<0.000
Posterior limb of internal capsule	0.68±0.05	0.70±0.04	p=0.023
External capsule	0.50±0.03	0.51±0.02	p=0.014
b) ODI (mean±std)			
WM ROIs	Pre-manifest HD	Controls	Statistics
Anterior limb of internal capsule	0.17±0.01	0.18±0.01	p<0.000

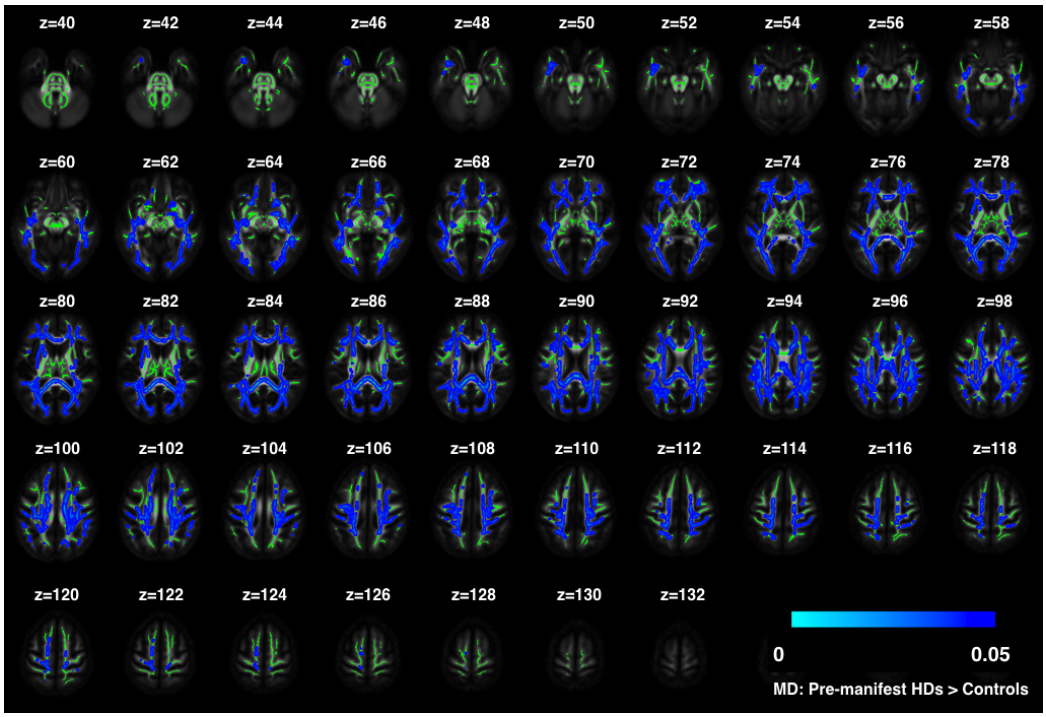

Figure 5.6: Whole brain white matter abnormalities in pre-manifest HD detected by MD using TBSS, TFCE corrected, $p<0.05$

5.4.5 Correlations between clinical scores of disease progression and NODDI metrics in selected white matter ROIs

Clinical scores of disease progression, CPO and TMS, were negatively correlated with NDI in the body and splenium of corpus callosum respectively (Figure 8.2 A-B). No HD progression scores significantly correlated with ODI in anterior limb of internal capsule.

5.4.6 The estimated sample sizes for selected ROIs using NODDI

For NDI, 19, 57, 16, 58, 43 participants for each group could achieve a power of 0.8 respectively in genu of corpus callosum, body of corpus callosum, splenium of corpus callosum, posterior limb of internal capsule, and external capsule. For ODI, 20 participants for each group could achieve the same power of 0.8 in anterior limb of internal capsule.

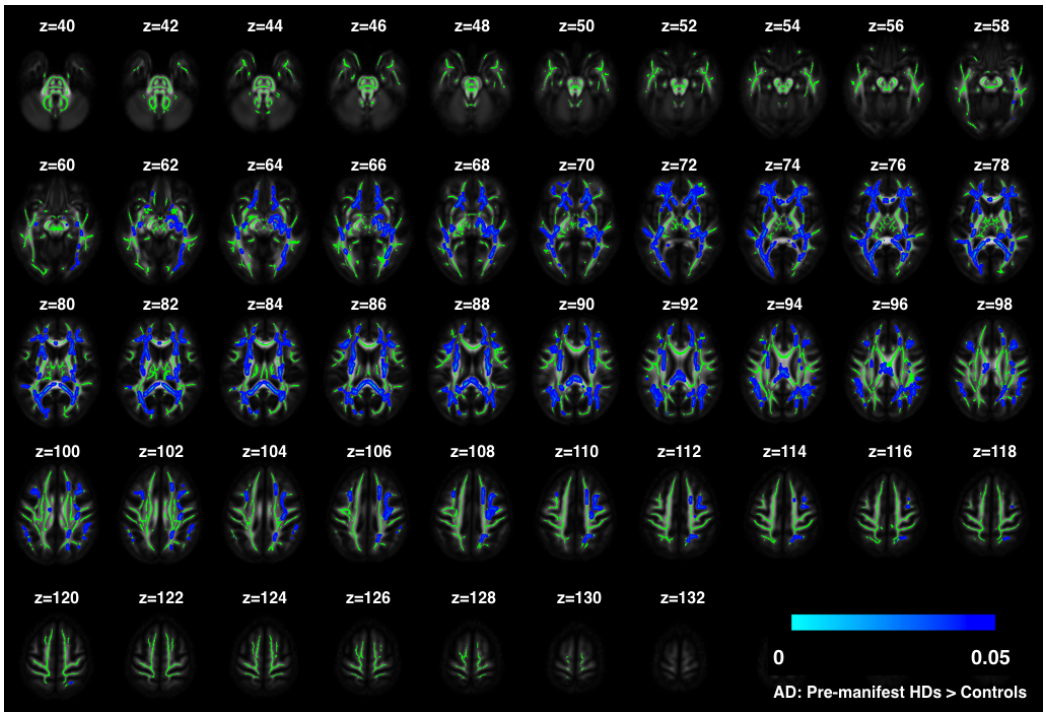

Figure 5.7: Whole brain white matter abnormalities in pre-manifest HD detected by AxD using TBSS, TFCE corrected, $p<0.05$

5.5 Discussion

To our knowledge, this study is the first that provides the most detailed depiction, to date, of the in-vivo axonal pathology in white matter at the premanifest stage of neurodegenerative diseases using a cohort of pre-manifest HD. Using NODDI, we found that NDI, the NODDI marker for axonal density, is reduced in widespread white matter of pre-manifest HD compared to the controls, and NDI in the callosal tracts correlated with the clinical measures of the disease progression. These findings provide direct support for the view that axonal loss is the major factor underlying white matter pathology in pre-manifest HD. Interestingly, we have also identified an alteration in the coherence of axonal organization in the white matter tracts surrounding the basal ganglia in pre-manifest HD compared to controls. This might suggest a compensatory prunning of axons in those white matter regions that are most likely to be affected in HD.

Whole-brain white matter analysis identified that compared with controls, pre-manifest HD had decreased NDI in widespread white matter areas. This suggests

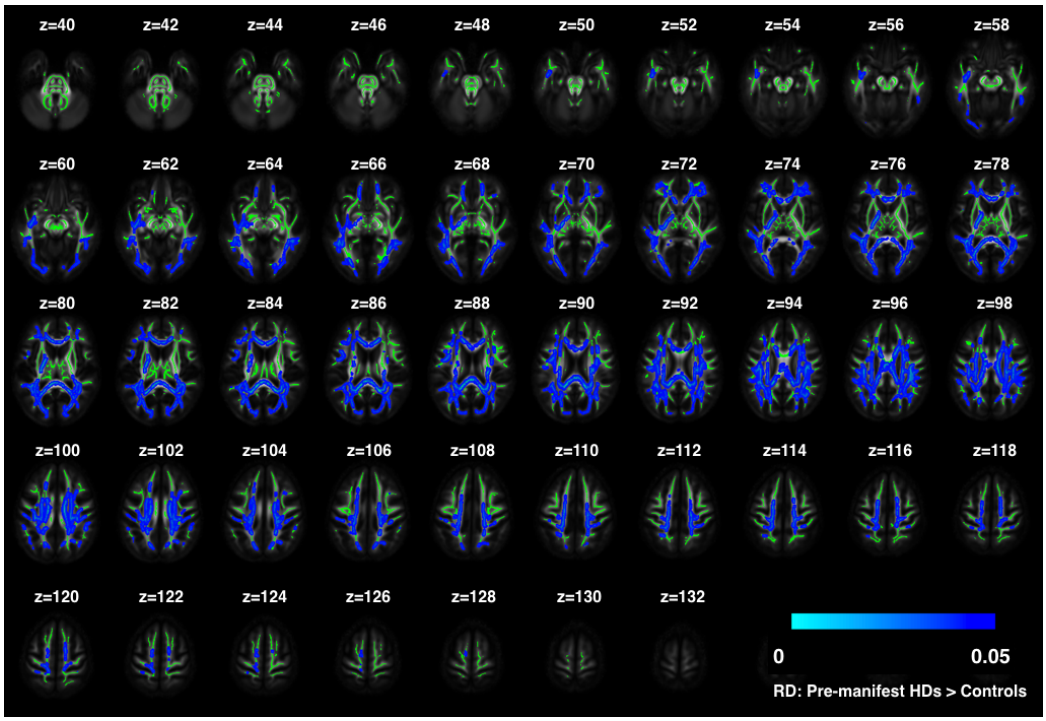

Figure 5.8: Whole brain white matter abnormalities in pre-manifest HD detected by RD using TBSS, TFCE corrected, $p<0.05$

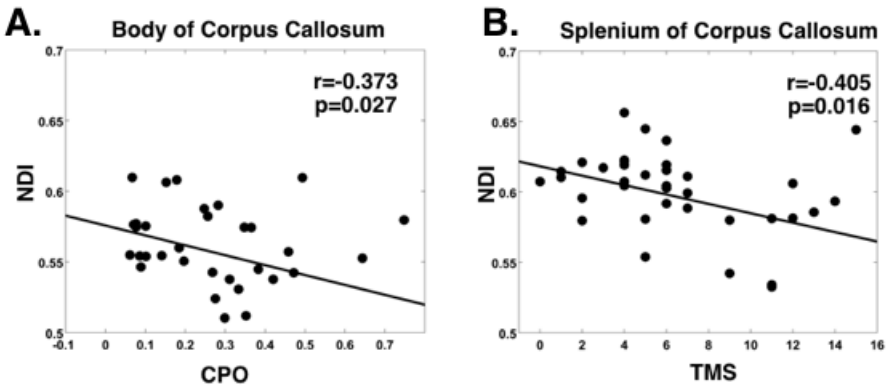

Figure 5.9: Correlations between clinical scores of disease progression and NODDI metrics

that 1) the reduction of axonal density might be the predominant factor of white matter pathology in pre-manifest stage of HD, which is supported by the evidence of abnormal axonal transport in the HD animal models [283,284]; 2) the widespread white matter abnormalities indicate a large proportion of abnormal structural connections between cortical and subcortical areas in pre-manifest HD individuals, pro-

viding further evidence to support the observed disrupted anatomical networks in pre-manifest HD population [223, 285–287]. Notably, even though it is plausible that the reduction in NDI observed here is underscored by the loss of axon density, there may also be an impact from the demyelination. In white matter regions with a loss of myelin, there might be a decreased MRI signal and a reduced NDI estimated by NODDI [107].

Meanwhile, we found a decrease in ODI of those white matter areas that surround the basal ganglia - the characteristic atrophy in Huntington′s disease. Pre-manifest HD individuals still maintain a normal life, and this suggests that fiber tracts linking the striatum to the cortex might be in a reorganizing process to compensate for the axonal loss in the same areas. This theory needs further efforts to investigate using the proposed compensation models in neurodegenerative diseases [288]. For example, to identify solid evidence of compensations in the brain of pre-manifest HD individuals, we could investigate HD-gene carriers at both younger adulthood and older adulthood to check if their microstructure in these areas are similar as the cohort we observed here, and if the functional activities of the brain are similar as what we observed here. Additionally, ODI has been validated in a recent histological study in the spinal cord of patients with Multiple Sclerosis (MS) [107]. This study showed the reduction in ODI is consistent with the histological observations of a reduced variability of axon orientation. This suggests that the increase coherence of axon packing might be a reflection of either reduced collateral branching driven by the pathology or the alterations in the morphometry of individual axons.

These NODDI findings together revealed a unique and complete picture of axon degeneration in whole brain white matter of HD. Importantly, our NODDI findings are highly likely to be reproducible because the cohort in our study is not unique. This is supported by the consistency of our DTI findings with previous studies [221–225].

Using DTI, we found that pre-manifest HD participants displayed widespread increased MD and reduced FA in white matter compared to controls. However, the

simplicity of the single tensor model used in DTI prevents changes in DTI metric from being directly linked to changes in the tissue properties of white matter. More explicitly, the increases in MD and decreases in FA that we observed here could be attributed to multiple factors in neurodegeneration, such as the decrease in axonal density, altered white matter organization (i.e., the coherence of fiber orientation), and the change in the partial volume effect. Even though we could speculate that these increases in MD are driven by the reductions in axonal density, an increase in free water volume can also attribute to MD increases [6].

Interestingly, we found that the group differences in NDI still survived after using a much stricter significant threshold of p value less than 0.01, but none of the differences in DTI metrics survived. This suggests that NODDI may have a better sensitivity than DTI. However, it is not fair to conclude that NODDI is more sensitive than DTI just with these datasets. Firstly, there is a difference in the voxel size of the datasets for DTI and NODDI. Our single-shell data for DTI has a smaller voxel size than multi-shell DWI data for NODDI. A smaller voxel has quite a few benefits, but it also means its SNR is lower than that of a bigger voxel. One can argue that the more abnormalities identified using NODDI than DTI may be partly due to our NODDI dataset might have a better SNR than DTI dataset. The DTI protocol used here was part of a longitudinal study - TRACK-ON HD, and they had already acquired DTI data for the previous two visits before adding a multi-shell DWI acquisition for NODDI. Therefore, it was not possible for us to change the settings of DTI just for our study at the third-time visit. Most importantly, there was very limited time left for adding new scans. In the end, we had to make the voxel size bigger for NODDI to make the acquisition time fit the whole schedule. Secondly, the number of measurements for single-shell DWI data for DTI is almost half of that for multi-shell DWI data for NODDI. Further studies on comparing the sensitivity of NODDI and that of DTI could be implemented in a fair way that we fit both NODDI and DTI to the same multi-shell dataset. Although DTI fails to describe the non-gaussian water diffusion, we could estimate the parameters of DTI using DKI as the kurtosis model is an extension of the 2nd-order tensor [289].

The tract-specific white matter ROI analysis further confirmed the importance of those white matter tracts in understanding the white matter pathology of HD. The decreases of NDI in all parts of corpus callosum suggest that the axon loss in corpus callosum might start in the early stage of HD. This may have an impact on the inter-hemisphere communications for certain cognitive activities as corpus callosum is the main pathway for transferring signals between the two hemispheres [290]. Interestingly, we found decreased NDI but decreased ODI in posterior and anterior limb of internal capsules. This suggests that in the pre-manifest stage of HD, the pathway that carries the communications between the striatum and the thalamus might have less axons and there might be a reorganization of axons that connects the structures within the striatum as posterior and anterior limb of internal capsules are those white matter tracts that connect different anatomical structures within the striatum and the striatum to the cortex and the thalamus [290]. Moreover, the decreased NDI in external capsules (a part of the corticostrital fiber tract [290]) suggests disrupted connections between putamen and the opercular cortex; these two are the major grey matter atrophies in HD [266].

As for the clinical relevance, we identified correlations between clinical measures of disease progression and NDI in corpus callosum. This demonstrated that NDI is very sensitive to pathological changes in pre-manifest HD and therefore has the potential to be a useful biomarker to track the disease progression during the pre-manifest stage of HD.

A deep understanding of the white matter pathology in the pre-manifest stage of HD could aid the developments of effective therapies for other neurodegenerative diseases, such as Parkinson's disease and dementia. As the axonal pathology may be shared by other protein-misfolding neurodegenerative disorders, NODDI might potentially offer new insights into a mechanistic understanding of white matter pathology in these diseases as well. However, we have studied data acquired at only one time point. Therefore, it is possible that our findings might be a reflection of the abnormal neural development caused by the abnormal HD gene mutations. Nevertheless, our work differentiated alterations to axonal density from other po-

tential confounding sources in neurodegeneration, such as the coherence of axon alignments, free water contamination and so on. This may contribute to linking ex-vivo histopathological observations to modern neuroimaging findings. In future, investigating a longitudinal cohort of pre-manifest HD might help clarify this concern.

A few issues deserve additional comments. Firstly, we used a multi-center dataset combining the data from two HD research centers. Given the relatively low prevalence of HD in the whole population, it is necessary to combine datasets from multiple centers to achieve a sufficient statistical power. To minimize any potential confounding effects, an identical acquisition protocol was used at both sites in the scanner with the same model, and in all our statistical analysis we have included "site" as a covariate. However, further studies are needed to investigate the potential impact of different scanners on the final results. Secondly, even though NODDI is much more informative on the tissue microstructure than the standard DTI, NODDI is still a simple model and may not describe pathological tissue microstructure fully in the neurodegenerative process. Nevertheless, NODDI still provides a unique window to study the axonal pathology at the microscopic level non-invasively and *in vivo*. Along with the future work we discussed earlier in this section, one more future work could be the exploration of the structural substrates in grey matter that are relevant to the functional abnormalities in both pre-manifest and manifest HD using NODDI as this technique was also proposed to probe the grey matter microstructure. Finally, as HD is characterized by the atrophy in basal ganglia, it would be interesting to investigate to what content, the white matter microstructural changes we observed here is affected by the atrophy, and how the interactions between the subcortical atrophy and the white matter pathways have impact on the development and the progression of HD.

5.6 Conclusions

In summary, our work showed that axonal loss might be a predominant feature of white matter pathology in pre-manifest HD, and NODDI metrics correlated with

clinical scores of disease progression. In addition, we also found group differences in NDI survived at a much stricter threshold of statistical significance, and might suggest its better sensitivity than DTI to white matter microstructural abnormalities at the pre-manifest stage of neurodegenerative diseases. These evidence together demonstrated the feasibility of NODDI in studying preclinical white matter changes and its clinical relevance.

Chapter 6

NODDI in young onset Alzheimer's disease

6.1 Introduction

In this chapter, we aimed to test the feasibility of NODDI in depicting the most detailed picture of *in vivo* white matter pathology at the clinical stage of neurodegenerative diseases. We also compared NODDI over the standard DTI in terms of the sensitivity to detecting white matter microstructural changes in patients compared with controls at the onset stage of neurodegenerative diseases.

The disease model we chose to represent the clinical stage of neurodegenerative diseases is Alzheimer's disease (AD), as AD is the most common cause of dementia in humans [291]. Young Onset AD (YOAD) patients are defined as those who have the disease onset at an age of less than 65 years old [190]. YOAD tend to have a faster disease progression than Late Onset AD (LOAD) [172–174], and often present non-amnestic phenotypes with unique syndromes, including a dysexecutive/behavioural syndrome [292], logopenic progressive aphasia [293] and posterior cortical atrophy [294]. These atypical phenotypes share a certain similarity in terms of the distribution of Aβ plaques [295], but they also have marked differences in the atrophy of the brain [296] and focal tau tangle pathology [297]. Although grey matter and the hippocamus are the first structures that break down in AD [298], white matter is also involved in AD patholgoy [299]. Moreover, from a

mechanistic perspective, the mismatch between the widespread amyloid deposition and more focal downstream neurodegeneration might be potentially explained by the prion-like spread of proteinopathies with tropism for specific large scale neural networks [300, 301]. As white matter is the information highway in the neural networks, it is of great interest to understand the pathology of white matter in YOAD.

With DTI, white matter microstructure in YOAD has been found to have decreased fractional anisotropy (FA) and increased diffusivity compared with normal controls [302–304]. As described in chapter 2, DTI is limited in terms of informing specific tissue properties. Using NODDI, we may differentiate the changes in axonal density from the changes in the spatial organisation while excluding the potential contamination from the free water that is often found to increase in tissue with degeneration [6].

As genes encode the protein that dictates the function of cells, these selective vulnerabilities of brain areas and differential patterns of brain pathology of YOAD patients are likely to be driven, at least to some degree, by the genetic influences. One of the established genetic risk factors for sporadic AD is Apolipoprotein (APOE) $\varepsilon 4$ [305]. In humans, there are 3 variants of APOE (i.e., $\varepsilon 2$, $\varepsilon 3$ and $\varepsilon 4$), and APOE $\varepsilon 4$ is found to be associated with the higher risk of disease manifestation for young onset AD [291] and the earlier decline of cognitive performance [306]. The protein APOE encodes is apoE, which is a low-density protein that is key in coordinating the redistribution and mobilization of fatty acid, cholesterol, and phospholipids [307]. And apoE protein is involved in brain plasticity, neuronal development and repair functions [308, 309]. As the major role of apoE in the brain is transporting the lipid components that contribute to building up the myelin sheath in the white matter [310–312], it would be interesting to study if genotypes (with or without APOE $\varepsilon 4$) may play a role in the white matter pathology in YOAD.

In this study, we applied both DTI and NODDI in a population of YOAD patients and controls. We tested the hypotheses that (1) NODDI could detect the white matter breakdown in YOAD; (2) NODDI metrics would reveal different patterns and extents of white matter microstructural damage in individuals with different geno-

types (with or without APOE $\varepsilon 4$); (3) NODDI could provide a much more detailed picture of white matter pathology in YOAD than DTI; and (4) regional measures of neurite density estimated using NODDI would correlate with performance on neuropsychological tests.

6.2 Research dissemination

This work has been accepted and published on Neurobiology of Aging.

- ApoE influences regional white matter neurite density loss in Alzheimer's disease, Slattery CF*, Zhang J*, Paterson RW, Foulkes AJM, Carton A, Macpherson K, Mancini L, Thomas DL, Modat M, Toussaint N, Cash DM, Thornton JS, Henley SMD, Crutch SJ, Alexander DC, Ourselin S, Fox NC, Zhang H, Schott JM, Neurobiology of Aging, 2017 (* joint first author)

6.3 Methods

6.3.1 Participants

From 2013 to 2015, we recruited 45 YOAD patients who met the diagnosis criteria for probable AD and had the disease onset at an age of less than 65 years old from a specialist Cognitive Disorders clinic. None of them had a family history or a known mutation that might suggest an autosomal dominant inheritance. For all the YOAD patients, we recorded their presenting cognitive symptom. YOAD patients were classified as having a phenotype of typical [313] or atypical (posterior cortical atrophy) AD [294] according to published diagnosis criteria. We also recruited twenty-four healthy controls who matched for the mean age and gender. All participants underwent MRI scans, the mini-mental state examination (MMSE) [314] testing, the assessment on the Hachinski Ischaemic Score [315] and an extensive neuropsychology battery designed to capture phenotypic diversity in YOAD include the assessments of:

- general intellect (the matrices and vocabulary subtests of the Wechsler Abbreviated Scale of Intelligence, WASI) [316];

- numeracy and literacy (Graded Difficulty Arithmetic, GDA) [317];
- episodic memory for faces and words (Recognition Memory Test, RMT) [318];
- visuospatial and visuoperceptual performance (Visual Object and Spatial Perception battery, VOSP) [319];
- Graded Difficulty Spelling Test, GDST) [320];
- Digit Symbol Modalities Test, DSMT [321];
- speed of processing and executive function (Delis−Kaplan Executive Function System−design fluency test, DKEFS) [322];
- verbal fluency.

Ethical approval of this study was obtained from the National Hospital for Neurology and Neurosurgery Research Ethics Committee of UK. Written informed consents were clearly explained to and obtained from all the subjects.

6.3.2 Assessing APOE ε4 genotype

Separate specific consents on blood donation for genetic analysis were assigned by all the patients. For each patient, their DNA was extracted from their blood sample and their APOE ε4 genotype was determined by PCR with 3'−minor groove binding probes.

6.3.3 Diffusion MR image acquisition

Participants were scanned in a Siemens Magnetom Trio (Siemens, Erlangen, Germany) 3T MRI scanner using a 32-channel phased array head coil at Queen square in London. A twice-refocused SE EPI sequence was used to minimise the eddy-current distortion for both NODDI and DTI acquisition.

6.3.3.1 The NODDI acquisition

The settings of the optimized NODDI protocol are: multiple b-values (2000, 700 and 300 s/mm^2) with 64, 32 and 8 non-colinear diffusion-weighted directions re-

spectively; 14 b=0 s/mm^2 images; voxel size=2.5×2.5×2.5 mm^3; TR/TE = 7000 ms/ 92 ms; 55 slices; the acquisition time about 16:13 minutes.

6.3.3.2 The DTI acquisition

The settings of the DTI protocol are: a b-value of 1000 s/mm^2 and 64 non-colinear diffusion-weighted directions; 9 b=0 s/mm^2 images; voxel size=2.5×2.5×2.5 mm^3; TR/TE = 6900ms / 91ms; 55 slices; the acquisition time about 16:29 minutes. This acquisition was repeated twice. Again, the DTI acquisition is part of a bigger study and they specified the acquisition parameters before we added NODDI acquisition.

6.3.4 Preparations of NODDI and DTI metric maps

Thirty-seven YOAD patients and twenty-three controls had both the DTI and NODDI data that passed the quality control criteria. All the diffusion-weighted images were confirmed to have the minimal artefacts. And the NODDI and DTI metric maps were estimated in the way as we explained in Chapter 4. We did 1) motion and eddy-current distortion correction; 2) exclude non-brain tissue by creating a brain mask and check whether the mask covers the brain properly; 3) model fitting for both NODDI and DTI; 4) spatial normalisation of both NODDI and DTI maps by registering the tensor map of each subject into the group-specific tensor template using DTI-TK. Notably, we fit tensor to the whole DTI dataset with 128 gradient directions, of which the volume number is similar to that of NODDI. Therefore, the comparisons of NODDI and DTI performances here are much fairer than what we did in chapter 5.

6.3.5 Statistical analysis

6.3.5.1 The statistics of clinical characteristics and neuropsychology scores

We converted the raw scores (x) of patient neuropsychology performances into z-scores $z = (x-u)/\sigma$, where u is the mean of the control population and σ is the standard deviation of the control population. Then we calculated the mean z scores for each neuropsychological test within each participant group and the composite

score for each cognitive score across all the neuropsychological tests (where applicable) for each domain. For categorical variables, we used fisher exact test and for the continuous scores, we used t test. For z scores, we used Wilcoxon rank sum test. All the statistical analyses of the clinical characteristics and neuropsychology scores were performed using Stata version 12.

6.3.5.2 The general linear model for group comparison

We used a general linear model (GLM) for group comparison. The dependent variable is the NODDI/DTI metric of either each voxel on the white matter skeleton or each ROI. For group comparisons, the GLM includes age, gender as covariates. Before entering covariates - age and gender into the GLM, for continuous variables such as age, we demeaned the variable and converted into a vector while for categorical variables - gender, we used 0 to represent male and 1 to represent female. The main factor is the group type, "APOE ε4-" standing for APOE ε4 negative patients, "APOE ε4+" standing for APOE ε4 positive patients, "YOAD" standing for all the patients and "NC" standing for normal controls.

6.3.5.3 TBSS Analysis

As designed in Chapter 4, we used TBSS to identify whole brain white matter microstructural changes using NODDI in patients compared to the controls. We created white matter skeleton from the group mean FA map in the template space with the default FA threshold (0.2). We then projected DTI and NODDI metric maps onto the skeleton.

After map projection, we used a non-parametric analysis for group comparison - permutation test [278], and we set up the GLM as we described in section 6.2.5.2. The permutation was performed 5000 times and multiple comparisons were corrected at $p<0.05$ using TFCE [279]. We also performed the same TBSS analysis of

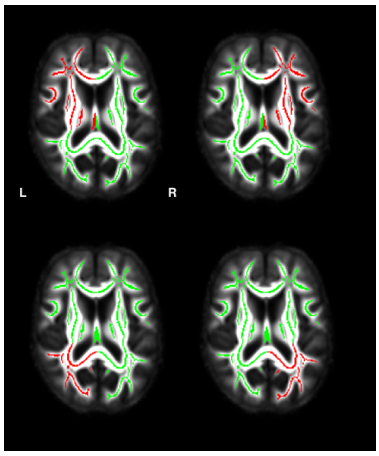

Figure 6.1: The 4 quadrant ROIs we defined on the white matter skeleton.

group comparisons between YOAD and controls using DTI. The contrasts of the pairwise comparisons we tested included "NC>YOAD", "NC<YOAD", "NC>APOE ε4-", "NC<APOE ε4-", "NC>APOE ε4+", "NC<APOE ε4+", "APOE ε4+>APOE ε4-", "APOE ε4+<APOE ε4-".

6.3.5.4 ROI Analysis

Four ROI corresponding to left and right posterior quadrants (parieto-occipital lobe projections) and left and right anterior quadrants (fronto-temporal lobe projections) of the white matter skeleton were manually defined to assess the relationship between microstructural tissue changes and neuropsychological performance in YOAD patients. These ROIs were delineated in the group template space by dividing the white matter skeleton into 4 areas at coordinates (x=112, y=88) (Figure 6.1). We then calculated the mean NODDI metrics (NDI, ODI and FISO) of each quadrant ROI for all the participants in our cohort. We further performed both group comparisons on NODDI metrics and correlations between NODDI metrics and the neuropsychological performances. In both analyses, we included age and gender covariates and a $p<0.05$ was considered significant.

6.4 Results

6.4.1 Demographics, genetic and clinical characteristics

Demographics and neuropsychological performance for all the participants are shown in Table 6.1. There were no significant differences in the mean age and gender between patients and controls (age, p = 0.3; gender, p = 0.8). No individual scored more than 4 on the Hachinski Ischaemic Score. As for the genotype of APOE 4 status, of the 37 patients, 22 (59%) were APOE ε4 positive (ε4+, 18 heterozygotes and 4 homozygotes) and the rest as APOE ε4 negative (ε4-). APOE ε4+ patients were significantly older than APOE ε4- patients at their enrollment to the study (p = 0.03). There were no significant differences between ε4+ and ε4- patients in MMSE scores, their age at the clinical symptom onset, or their clinical

disease duration at enrollment to the study. Most of the ε4+ patients were characterised as a 'typical AD' amnestic phenotype (19 out of 26) while 8 of the ε4- patients presented a phenotype of a 'typical AD' amnestic phenotype and the other 7 of the ε4- patients had atypical AD - Posterior Cortical Atrophy (PCA).

6.4.2 Neuropsychological profiles

YOAD patients showed multi-domain cognitive impairments, including performance IQ; literacy and numeracy; recognition memory for words; speed of information processing and executive function; visuospatial and visuoperceptual performance (Table 6.1). Compared with APOE ε4+ patients, APOE ε4- patients did not have significant differences in the duration of the disease but had worse performances on the speed of information processing and executive function (p=0.01) and the tests of literacy and numeracy (p=0.04).

6.4.3 Whole brain white matter microstructural damage in YOAD

6.4.3.1 Group differences detected by NODDI using TBSS analysis

The voxel-wise group differences in NODDI metrics between YOAD patients and controls on the white matter skeleton were shown in Figure 6.2. Compared to controls, YOAD patients had reduced NDI in occipital, parietal, temporal frontal white matter, superior longitudinal fascicules, cingulum, the splenium and genu of the corpus callosum. Moreover, we found reduced ODI in splenium and body of corpus callosum, superior longitudinal fascicules, and temporal white matter. Interestingly, we found increases in FISO in the corpus callosum.

6.4.3.2 Group differences detected by DTI using TBSS analysis

The voxel-wise group differences in DTI metrics between YOAD patients and controls on the white matter skeleton were shown in Figure 6.3. We found that compared to controls, YOAD patients had decreased FA and increased diffusivities (MD, AxD and RD), involving the occipital, parietal, temporal white matter, corpus callosum. Unlike NODDI results, the majority of frontal white matter were spared

using DTI. The differences in FA and RD between YOAD and controls were more asymmetric compared with those in MD and AD.

6.4.4 White matter microstructural damage in YOAD with different APOE ε4 genotypes

6.4.4.1 Group differences detected by NODDI using TBSS analysis

The voxel-wise group differences in NODDI metrics between genotypes of YOAD patients and controls on the white matter skeleton were shown in Figure 6.4, Figure 6.5 and Figure 6.6. Both APOE ε4+ YOAD patients and APOE ε4- YOAD patients had similar distribution of decreased ODI compared with controls. However, these two showed their unique signature differences in NDI and FISO compared with controls. Both patient groups had significant decrease in NDI across the parietal-occipital and temporal white matter areas compared with controls. However, YOAD patients with APOE ε4 showed much more widespread white matter impairments with decreased NDI across the brain than YOAD patients without ε4. Specifically, frontal white matter was less involved in patients without APOE4, and there was a difference in the symmetry of decreased NDI between APOE ε4+ and APOE ε4- YOAD patients. Moreover, APOE ε4- YOAD patients had significant FISO increase compared with controls while no significant increase in FISO was found in APOE ε4+ YOAD patients. No significant group differences were found when we compared YOAD patients with APOE ε4 directly.

6.4.4.2 Group differences detected by DTI using TBSS analysis

The voxel-wise group differences in DTI metrics between genotypes of YOAD patients and controls on the white matter skeleton were shown in Figure 6.7, Figure 6.8, Figure 6.9 and Figure 6.10. Both YOAD groups with or without APOE ε4 had decreased FA involving the parieto-occipital white matter, genu of the corpus callosum, temporal white matter. However, in the FA differences relative to controls, YOAD APOE ε4+ patients involved less areas of corpus callosum and temporal lobe than YOAD APOE ε4- patients. MD, AxD and RD were all found to increase in both YOAD patient groups compared with controls, in the splenium, body and

genu of the corpus callosum, and parieto-occipital white matter. Moreover, YOAD APOE ε4+ patients had increased RD in the frontal white matter. And there were no significant group differences in any of DTI metrics when we compared YOAD subgroups directly.

6.4.5 ROI analysis with NODDI metrics

6.4.5.1 Group differences in NODDI metrics of ROIs on the white matter skeleton

We presented the mean NODDI metrics of all the 4 quadrant white matter skeleton ROIs in Table 6.2. The group comparisons showed that in all the 4 quadrant ROIs, YOAD patients had abnormal NDI compared with controls. There were no significant differences in FISO and ODI between YOAD patients and controls.

6.4.5.2 The correlations between NODDI metrics and cognitive function in patients

The correlation analysis showed that in patients, NDI of the quadrant white matter ROI in the right parieto-occipital lobe had significant positive correlations with the visually-demanding measure of performance IQ from WASI matrices (Figure 6.11A); NDI of both the left and right quadrant white matter ROI in the parieto-occipital lobes had significant positive correlations with the visuospatial and visuoperceptual tasks (Figure 6.11 B and 6.11 C). There were no other correlations between NDI and the cognitive performance in any other domain. There were no significant correlations between ODI and any cognitive performance in all the domains. There was a positive correlation between FISO of the left quadrant white matter ROI in the posterior lobe and the performance of episodic memory for words in patients ($r=0.4$, $p=0.01$).

6.5 Discussion

This study used NODDI to identify white matter damage in YOAD and its associations with the APOE ε4 genotype in YOAD patients. We found that NODDI is sensitive to the white matter abnormalities in YOAD patients and has the potential

to provide further insights into the commonalities and differences in white matter change associated with APOE ε4 genotype. On top of the shared parietal-occipital white matter changes, YOAD APOE ε4+ patients had more widespread areas with reduced NDI while YOAD APOE ε4- patients exhibited reductions of NDI in more focal posterior areas. And we demonstrated that regional NDI on the white matter skeleton correlated with cognitive impairments in YOAD, suggesting that NODDI metrics not only provide insights into regional white matter vulnerability, but also have relevant clinical correlates. In the same cohort, DTI also revealed white matter impairments in both APOE ε4+ and APOE ε4- YOAD patients relative to controls.

We found that NODDI is sensitive to the white matter damage in YOAD. Most importantly, we confirmed the benefits of the tissue specificity of NODDI metrics. For example, in corpus callosum, we found that all the diffusivity metrics of DTI increased in YOAD patients. However, in the same region, we found that there was an increase in FISO using NODDI. This highlighted the fact that DTI metrics are prone to free water contaminations and changes in NODDI metrics are free from this partial volume effect.

Moreover, APOE ε4+ YOAD patients had more extensive white matter areas with reduced NDI than APOE ε4- YOAD patients. Although there were no significant group differences in the direct comparisons between these two genotypes of YOAD, we found that the t statistic map (Figure 6.12) of the direct comparison exhibited the statistical trend of group differences as we compare the differences each group had in the comparison with normal controls. Moreover, the reduction in NDI of right parietal white matter keeps with a trend of worse performances of visual tasks. Moreover, the differences and similarities of white matter damage in YOAD genotypes may suggest a subtle modulation of this AD risk gene on brain structure and functions. The reduction in NDI suggests axonal loss in YOAD and this is supported by histological observations on abnormal axonal transport in AD [195, 196].The reduction in ODI of white matter in YOAD patients may suggest a disorganization of fibers in those areas. Moreover, we identified the correlations between NDI and the cognitive performances of YOAD patients. This highlighted

the clinical relevances of NODDI metrics. However, we also found an unexpected correlation between FISO in the left posterior quadrant on the white matter skeleton and episodic memory for words. As we did not find any significant group differences in FISO, the cause of this correlation is not clear and we may need further investigations.

The ROI analysis was based on our manual definition of 4 parts of the white matter skeleton. This was just an approximate parcellation, and it was defined according to the experience as described. The principle behind it was simply to extract the white matter areas on the skeleton that correspond to the white matter in the frontal and posterior lobe of both hemispheres as the cognitive performances we were interested in are thought to be related to those white matter. Future studies could be done to explore the relationship between specific cognitive performance and white matter tracts that we reconstruct using tractography. T1-weighted images can also be exploited to parcellate the white matter skeleton according to the lobe they belong to. Interestingly, we found that FISO of the left quadrant white matter skeleton correlated with the performance of episodic memory for words in YOAD patients. As AD is known to have enlarged ventricles, future studies are needed to identify the relationship between the volume loss in this area and the NODDI metrics as well as the cognitive performances.

There are a few limitations. Firstly, the assumptions in NODDI may not be appropriate for disease conditions. And as a simple model, NODDI cannot characterise all kinds of possible pathology in neurodegenerative diseases. Secondly, we did not account for the potential presence of white matter hyperintensities (WMH) on our results. Previous studies have shown that changes in DTI metrics might be related to this WMH [323]. However, YOAD are less likely to have coexistent vascular problems than LOAD at clinics. Therefore, we expect our results are less confounded by this WMH. Nevertheless, future studies are required to check if NODDI metrics are affected by WMH lesions. Thirdly, we only have a relatively small cohort of the YOAD patients and it might be the reason that no significant differences in either DTI metrics or NODDI metrics survived in the direct compar-

isons between the genotypes of YOAD. Future studies with bigger sample sizes are needed to confirm our findings. Lastly, we did not have the genotype information of the normal controls, and we assumed that the distribution of APOE $\varepsilon 4$ status is similar in patients as the controls. Previous studies showed that APOE $\varepsilon 4$ is a factor that has influence on brain microstructure in normal controls [206,324,325]. Therefore, our findings here need confirmations in future studies. As for future work, it would be interesting to evaluate the sensitivity of NODDI to the early white matter abnormalities at the preclinical stages of AD. Moreover, it is of clinical importance to investigate if microstructural changes detected by NODDI and DTI are earlier than the volumetric losses. Thirdly, as NODDI is a model designed to describe both grey and white matter, we could also explore the respective microstructural changes in grey matter in YOAD as this may inform on the cortical atrophy. Finally, as cortical and hippocampal atrophy are known to be the characteristic atrophy in AD, it would be interesting to investigate the relationship between these atrophy and the white matter microstructural abnormalities we observed here.

6.6 Conclusion

Using NODDI, we identified white matter abnormalities in YOAD patients compared with controls, and found NODDI could give a better quantification of the tissue-specific microstructural changes than DTI. And we found NODDI has the potential to reveal the associations between gene status and the spatial distribution of white matter impairments in YOAD. In conclusion, we demonstrated the feasibility of NODDI in detecting the white matter damage at the clinical stage of neurodegenerative diseases using YOAD as a disease model. And NODDI may provide a more fine-grained depiction of the microstructural changes at the clinical stages of neurodegenerative process.

Table 6.1: The Demographic and Clinical Characteristics.

	Controls n=23	YOAD n=37	p	APOE ε4- n=15	APOE ε4+ n=22	p
Demographics						
Sex, M:F, n	10:13	18:19	0.8	7:8	11:11	1.0
Age (years), mean/std	60.7/6.0	62.3/4.9	0.3	60.2/3.8	63.6/5.2	0.03
Handedness, L:R, n	3:20	1:36	0.2	0:15	1:21	1.0
Years of education	16.7/3.1	14.9/2.8	0.03	15.5/2.3	14.5/3.0	0.3
MMSE (/30)	29.3/1.0	21.3/4.5	$<$0.0001	19.9/4.4	22.3/4.4	0.1
Age at onset (years)	n/a	56.8/4.4	n/a	55.4/4.3	57.8/4.4	0.1
Disease Duration (years)	n/a	5.4/3.2	n/a	4.8/3.0	5.9/3.3	0.3
Neuropsychology						
General intellect: Verbal IQ (WASI vocabulary), z score	n/a	-1.15/1.9	n/a	-1.56/2.3	-0.88/1.6	0.4
General intellect: Performance IQ (WASI matrices), z score	n/a	-5.80/2.4	n/a	-6.24/2.3	-5.43/2.39	0.4
Episodic memory for faces (RMT), z score	n/a	-1.90/1.8	n/a	-1.65/1.3	-2.08/2.1	0.6
Episodic memory for words (RMT), z score	n/a	-4.35/2.6	n/a	-4.38/2.7	-4.33/2.5	0.8
Literacy and numeracy (GDST, GDA), z score	n/a	-2.04/1.3	n/a	-2.54/1.0	-1.70/1.4	0.04
Visuoperceptual and visuospatial (VOSP), z score	n/a	-6.81/6.5	n/a	-8.34/5.7	-5.76/7.0	0.09
Speed of processing and executive function (DKEFS), z score	n/a	-2.23/0.8	n/a	-2.6/0.7	-1.97/0.7	0.01
Phenotype						
Leading symptom, memory/visual	n/a	24/13	n/a	8/7	16/6	0.3

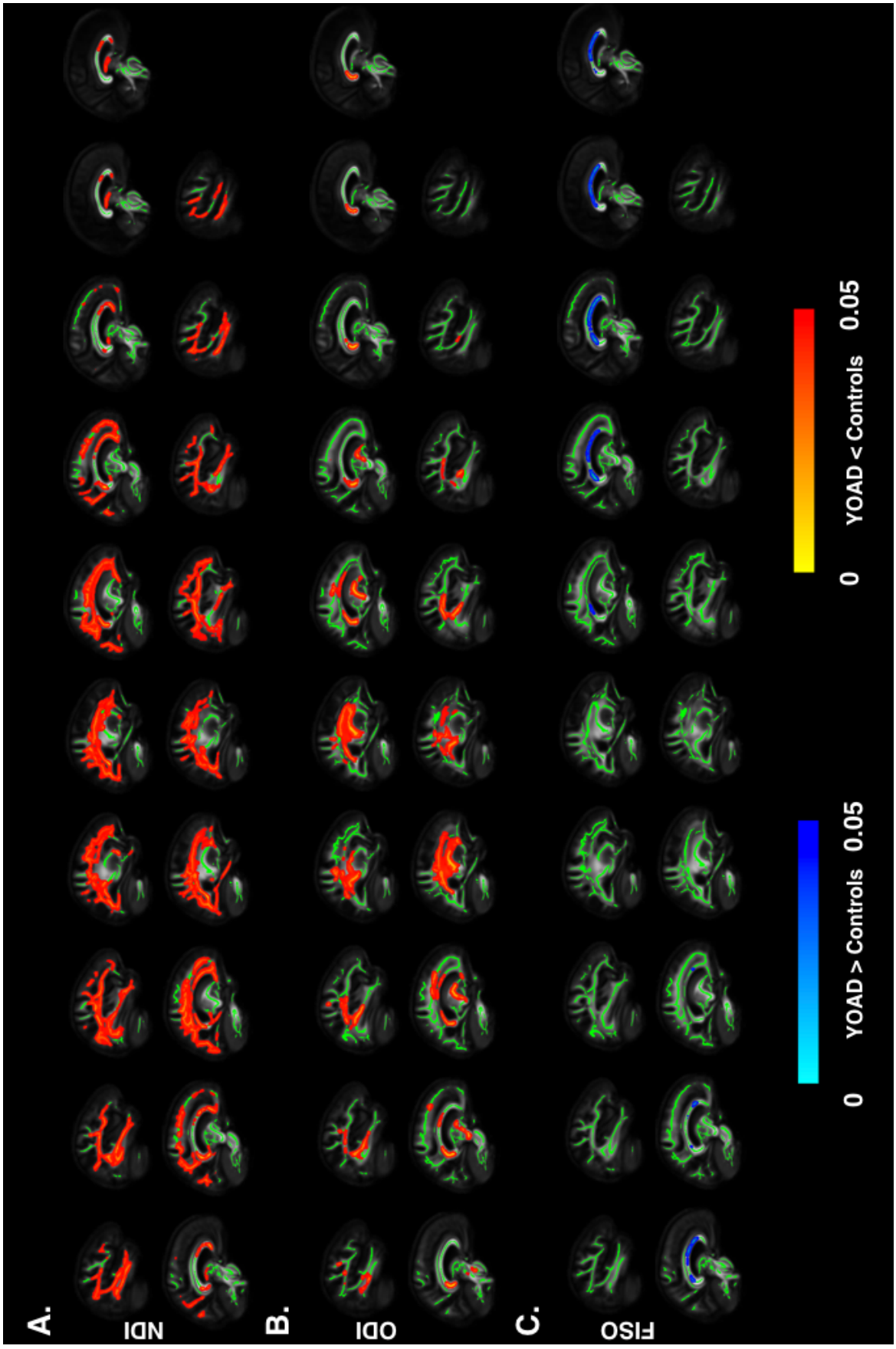

Figure 6.2: Group differences in NODDI metrics between YOAD and controls on the white matter skeleton, tfce corrected p<0.05. A. NDI; B. ODI; C. FISO.

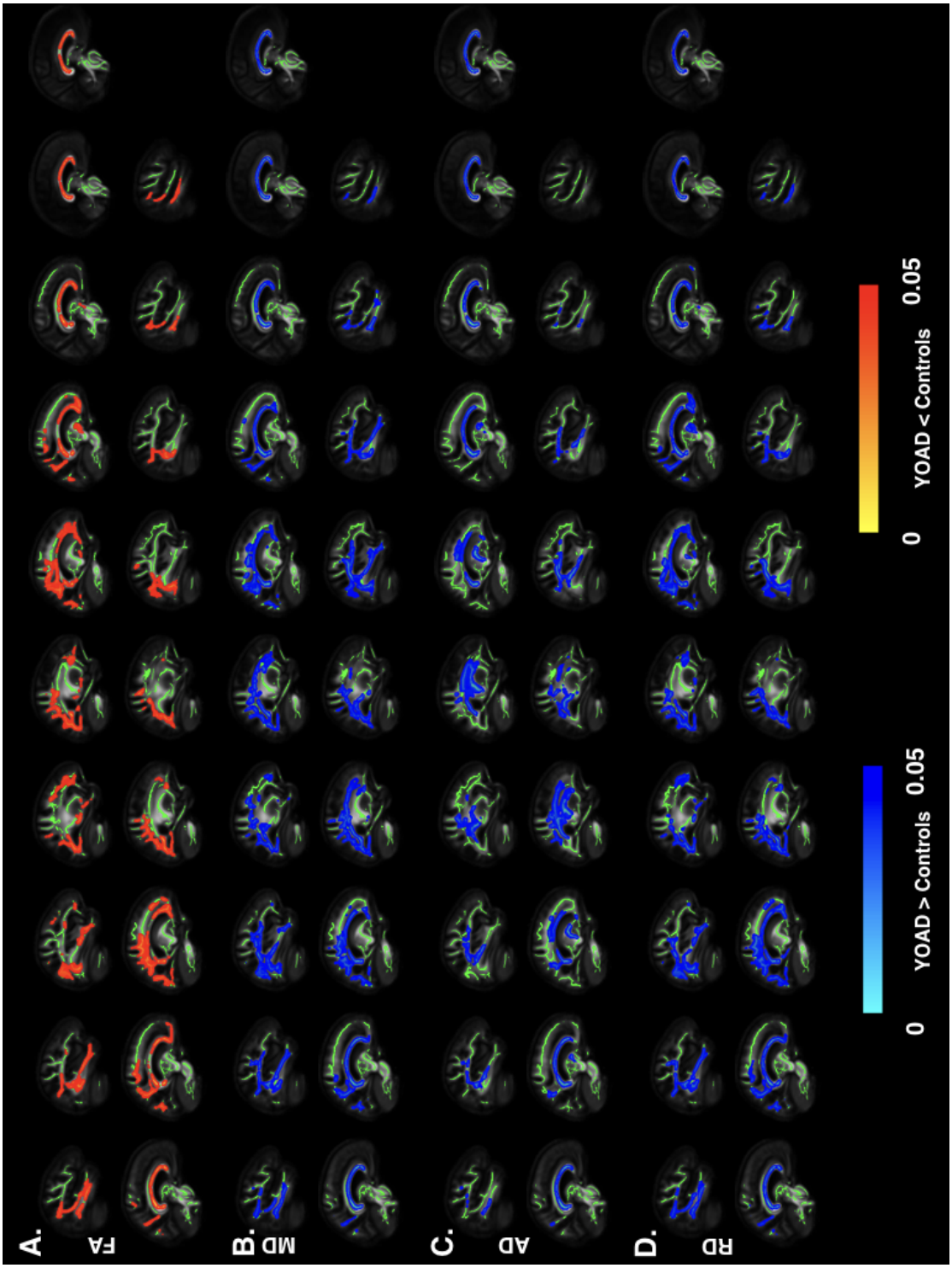

Figure 6.3: Group differences in DTI metrics between YOAD and controls on the white matter skeleton, tfce corrected p<0.05. A. FA; B. MD; C. AD; D. RD.

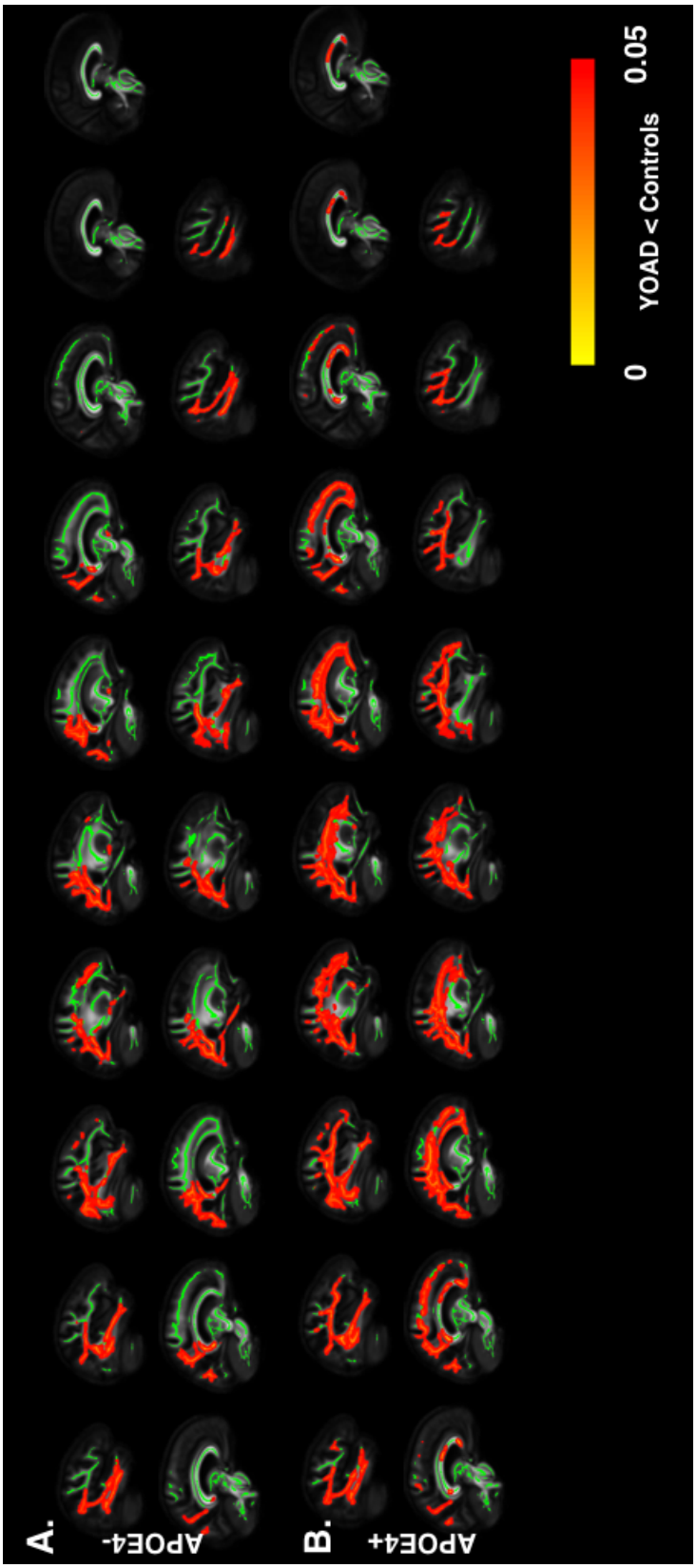

Figure 6.4: Group differences in NDI between YOAD genotypes and controls on the white matter skeleton, tfce corrected $p<0.05$. A. APOE ε4-; B. APOE ε4+.

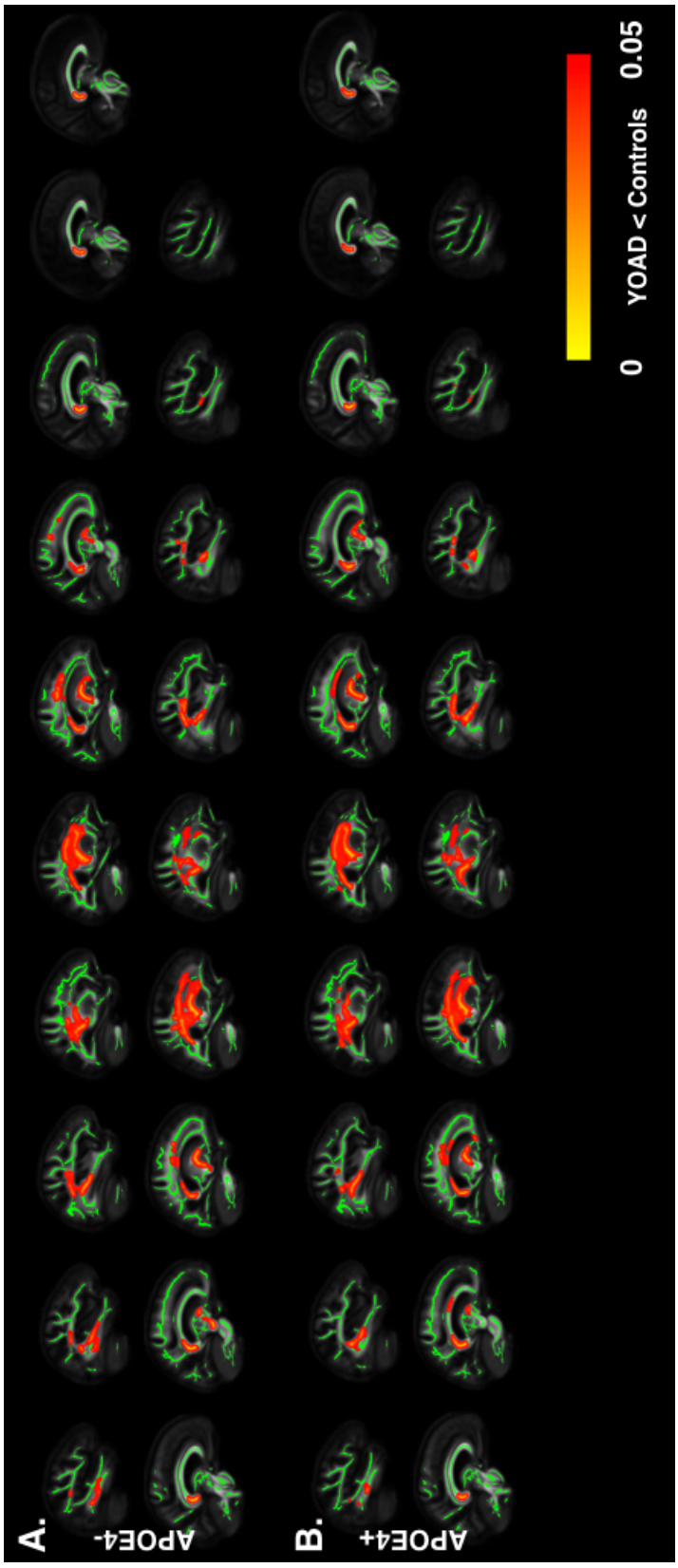

Figure 6.5: Group differences in ODI between YOAD genotypes and controls on the white matter skeleton, tfce corrected $p<0.05$. A. APOE ε4-; B. APOE ε4+.

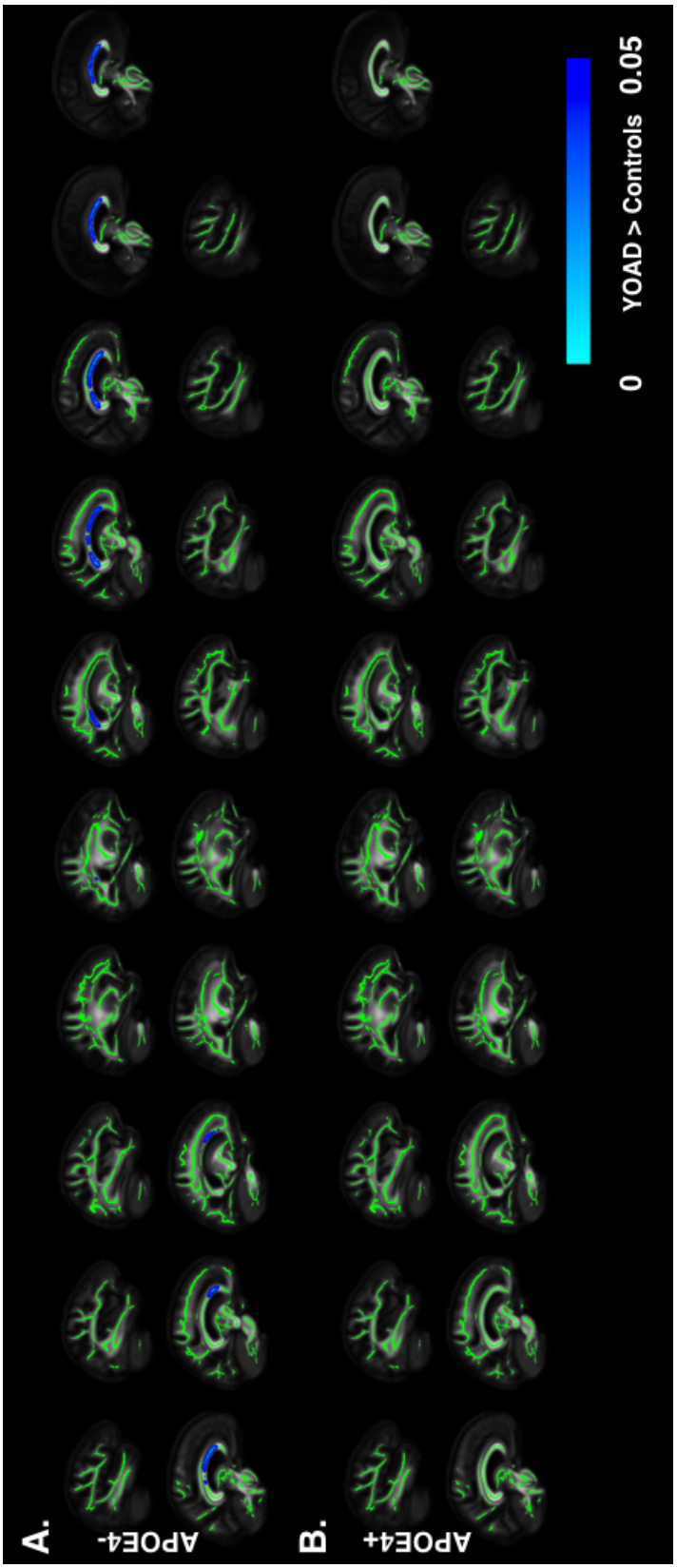

Figure 6.6: Group differences in FISO between YOAD genotypes and controls on the white matter skeleton, tfce corrected $p<0.05$. A. APOE ε4-; B. APOE ε4+.

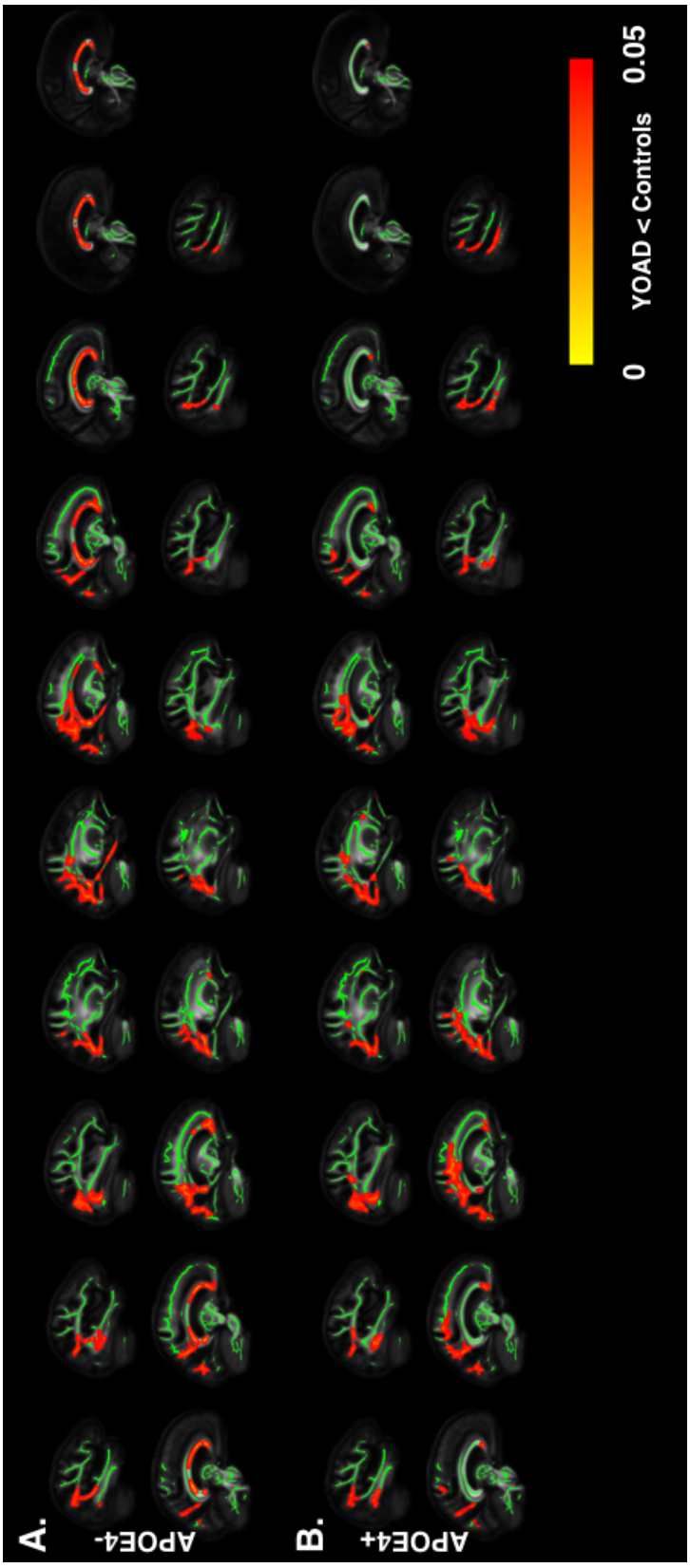

Figure 6.7: Group differences in FA between YOAD genotypes and controls on the white matter skeleton, tfce corrected $p<0.05$. A. APOE ε4-; B. APOE ε4+.

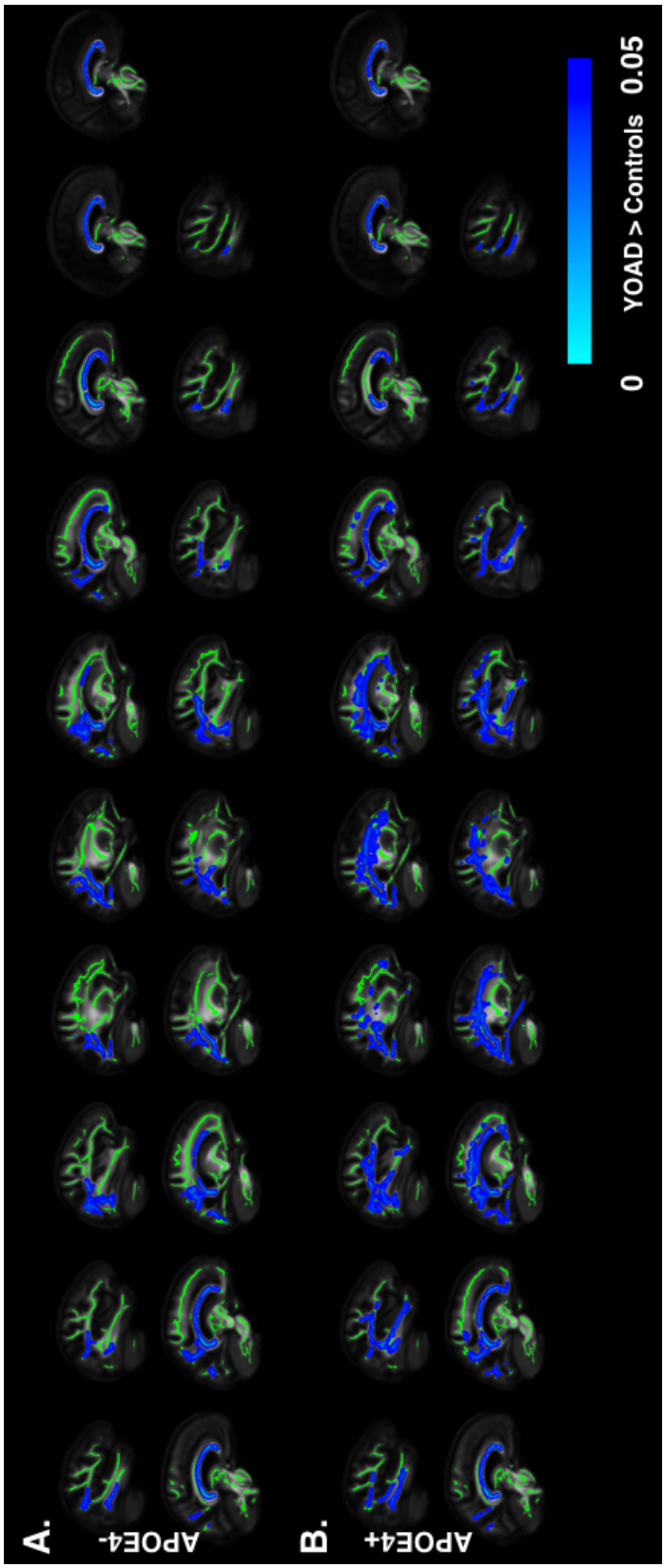

Figure 6.8: Group differences in MD between YOAD genotypes and controls on the white matter skeleton, tfce corrected $p<0.05$. A. APOE ε4-; B. APOE ε4+.

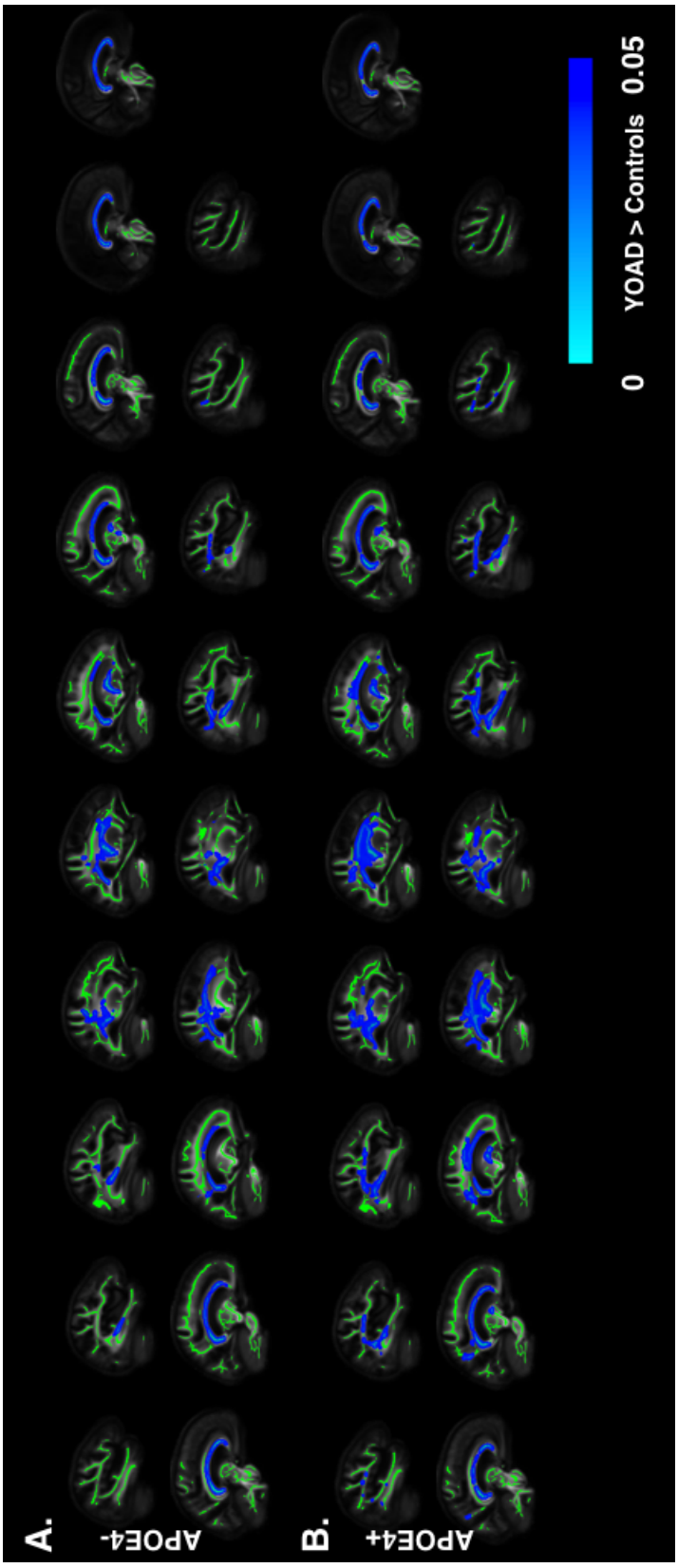

Figure 6.9: Group differences in AD between YOAD genotypes and controls on the white matter skeleton, tfce corrected $p<0.05$. A. APOE ε4-; B. APOE ε4+.

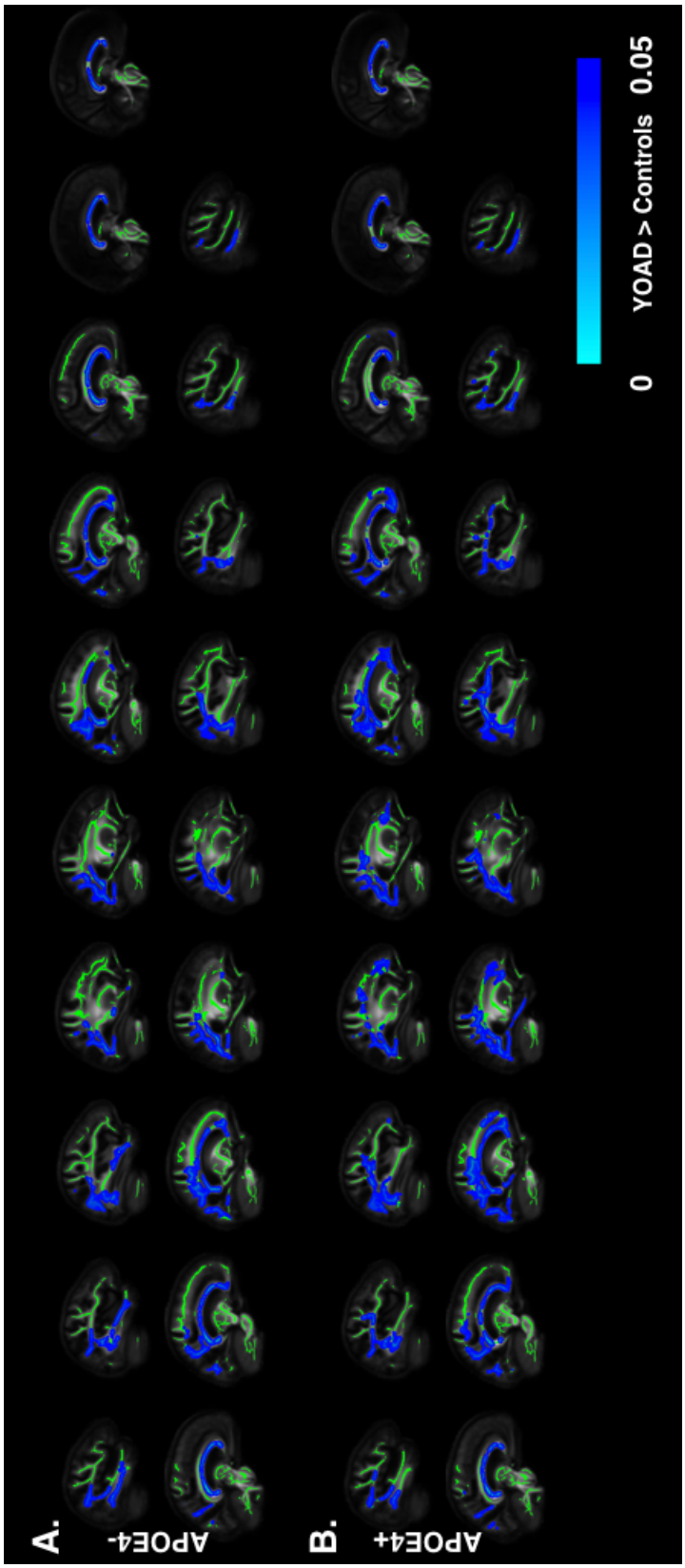

Figure 6.10: Group differences in RD between YOAD genotypes and controls on the white matter skeleton, tfce corrected $p<0.05$. A. APOE ε4-; B. APOE ε4+.

Table 6.2: NODDI metrics of all quadrant white matter ROIs on the white matter skeleton in YOAD and controls.

WM ROIs	YOAD	Controls	Statistics
NDI (mean±std)			
Left anterior quadrant	0.554±0.022	0.538±0.031	p=0.043
Left posterior quadrant	0.559±0.029	0.518±0.031	p<0.0001
Right anterior quadrant	0.555±0.022	0.539±0.036	p=0.067
Right posterior quadrant	0.552±0.029	0.511±0.052	p=0.001
ODI (mean±std)			
Left anterior quadrant	0.214±0.015	0.214±0.007	p=0.95
Left posterior quadrant	0.202±0.023	0.201±0.007	p=0.76
Right anterior quadrant	0.213±0.014	0.211±0.008	p=0.54
Right posterior quadrant	0.195±0.013	0.194±0.008	p=0.68
FISO (mean±std)			
Left anterior quadrant	0.105±0.017	0.108±0.016	p=0.67
Left posterior quadrant	0.107±0.024	0.111±0.017	p=0.58
Right anterior quadrant	0.099±0.017	0.106±0.018	p=0.22
Right posterior quadrant	0.101±0.023	0.111±0.034	p=0.26

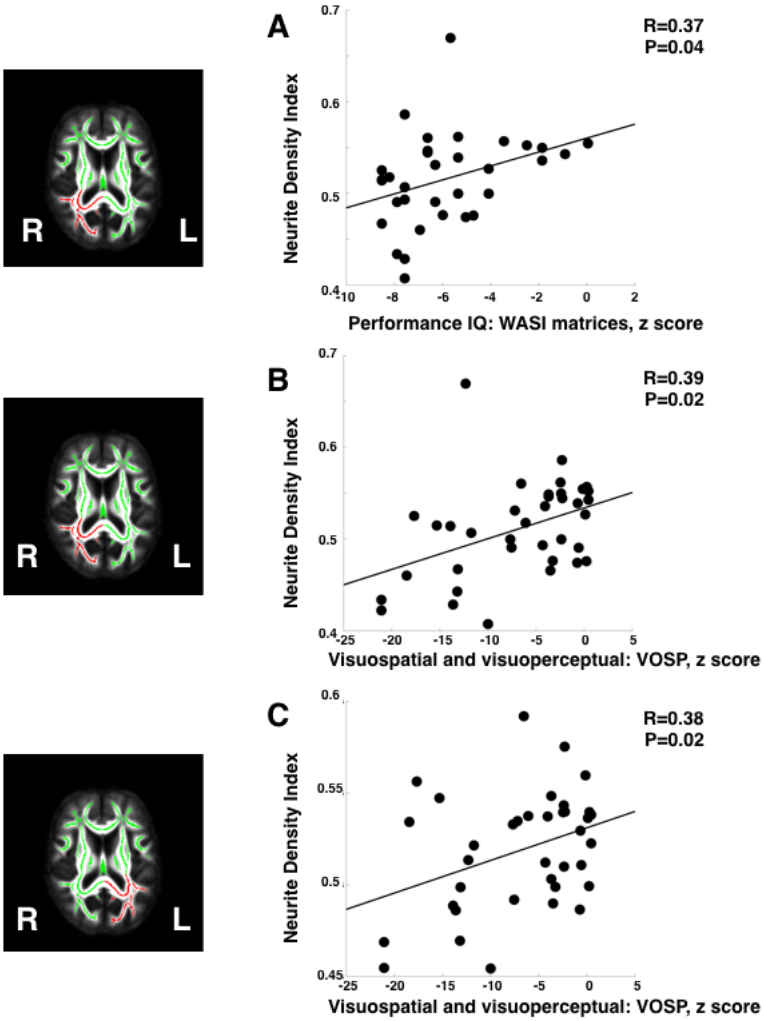

Figure 6.11: The correlations between NODDI metrics and cognitive function in YOAD patients (adapted from [271])

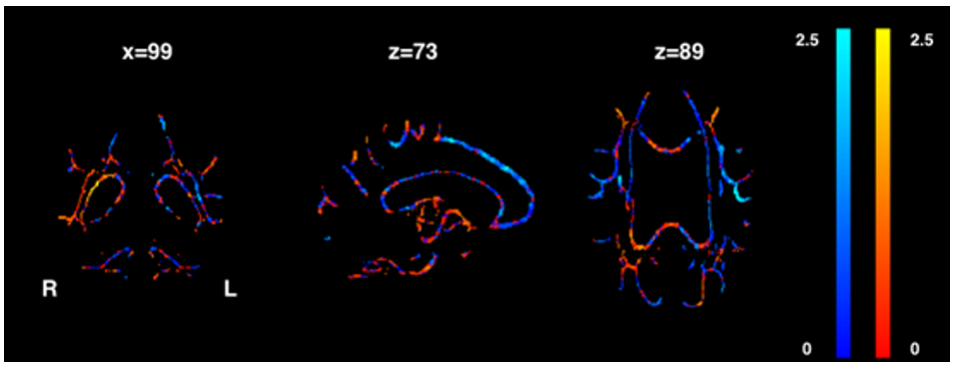

Figure 6.12: The t statistic map of the direct comparison between APOE ε4+ YOAD patients and APOE ε4- YOAD patients, warm color APOE ε4+ YOAD patients $<$ APOE ε4- YOAD patients, cool color APOE ε4+ YOAD patients $>$ APOE ε4- YOAD patients

Chapter 7

NODDI in longitudinal young onset AD

7.1 Introduction

In this chapter, we aimed to test the feasibility of NODDI in tracking the longitudinal progression of the *in vivo* white matter damage at the clinical stage of neurodegenerative diseases.

In both the cross-sectional studies described in chapter 5 and 6, we demonstrated the feasibility of NODDI in revealing a detailed picture of the *in vivo* white matter pathology at both the preclinical and clinical stages of neurodegenerative diseases using pre-manifest HD and YOAD as the disease models. Moreover, in chapter 6, we found that NODDI has the potential to reveal the impact of APOE $\varepsilon 4$ genotypes on the profiles of white matter damage in YOAD. As a novel technique that might potentially bridge the gap between the traditional pathology in postmortem studies and the *in vivo* neuroimaging, it is also of great importance to investigate if NODDI metrics could be sensitive biomarkers of the temporal evolution of white matter damage in clinical studies.

The importance of studying white matter abnormalities in AD has been highlighted by previous findings of abnormal axonal transport in Alzheimer$'$ disease. The deficiency of axonal transport has been suggested to be a cause and a consequence of the generation of amyloid β (Aβ) [201, 326]. The accumulation of this

amyloid β is considered as another characteristic feature in AD pathology [327]. Another essential factor for the maintenance of normal axonal transport is the neuronal cytoskeleton, which can be disrupted by APOE $\varepsilon 4$ [170]. In addition, the accumulation of the hper-phosphorylated tau protein in the intraneuronal neurofibrillary tangles is also taken as a characteristic feature in AD pathology [327]. Tau protein often presents in axons, and is mostly expressed by neurons that have a preferential axonal localization [328]. The C-terminal microtubule-binding region of Tau protein has a key role in the successful assembly and the stabilisation of axonal microtubules [329–331]. Therefore, tau protein is important for the regulation of axonal transport [332]. Additionally, we often find that axonal swelling occurs in these three features that are involved in AD pathogenesis (Amyloid β, tau, and APOE $\varepsilon 4$) [333–336]. Therefore, studying abnormalities in white matter might shed light on revealing AD pathology.

White matter abnormalities in AD has been studied by DTI both cross-sectionally and longitudinally. The cross-sectional studies have consistently found that widespread white matter areas in AD had increased diffusivity and decreased FA compared with normal controls, including the temporal, parietal and frontal white matter, the corpus callosum and the longitudinal association fiber tracts [226–230]. Longitudinally, FA has been found to decrease but MD has been found to increase over time in the fornix, corpus callosum, inferior cingulum, hippocampal cingulum, internal and external capsule, corona radiata, posterior thalamic radiation, superior and inferior longitudinal fasciculus, fronto-occipital fasciculus, tapetum and uncinate fasciculus [231–234]. Whilst sensitive, due to the limited single tensor model used in DTI, we can not directly link the DTI findings with any specific tissue property. Such tissue properties have been becoming more and more accessible with the emerging advanced diffusion MRI techniques with biophysical models. NODDI is one of such techniques that provides compartment-specific information on the tissue properties. NODDI uses different mathematical distributions to model the water diffusion contributed by different microstructure compartments and therefore provide us much more detailed information on the tissue property.

Here, with a cohort of YOAD patients and controls scanned at both the beginning and the end of one year, we explored the potential utility of NODDI for depicting the temporal evolution of white matter pathology in neurodegenerative diseases. In this exploratory study, we used a whole brain white matter voxel-wise analysis - TBSS together with an unbiased longitudinal analysis framework [262]. Additionally, we explored the potential impact of APOE $\varepsilon 4$ on the progression pattern of white matter damage in YOAD using NODDI.

7.2 Research dissemination

This work has been presented in ISMRM 2017 and AAIC 2017. And a journal paper is under preparations.

- Longitudinal neurite orientation dispersion and density imaging in young onset AD, Slattery CF, Zhang J, Paterson RW, Foulkes AJM, Carton A, Macpherson K, Mancini L, Thomas DL, Modat M, Toussaint N, Cash DM, Thornton JS, Henley SMD, Crutch SJ, Alexander DC, Ourselin S, Fox NC, Zhang H, Schott JM, Alzheimer's and Dementia, 2017.

- Longitudinal progression of white matter deficits in Young Onset Alzheimer's Disease and Its Syndromic Variants using NODDI, Zhang J, Slattery CF,Paterson RW, Foulkes AJM, Carton A, Macpherson K, Mancini L, Thomas DL, Modat M, Toussaint N, Cash DM, Thornton JS, Henley SMD, Crutch SJ, Alexander DC, Ourselin S, Fox NC, Zhang H, Schott JM, International Society for Magnetic Resonance in Medicine, 2017.

7.3 Methods

7.3.1 Participants

Out of the cohort we described in chapter 6, there were 20 controls and 26 YOAD patients who participated in both of the scans (see chapter 6 for more details on participants).

7.3.2 Assessing APOE ε4 genotype

For each patient, their APOE ε4 genotype was determined as we described in Chapter 6.2.2. Specific consents on donating blood for genetic analysis were given, explained and assigned by the patients at both times.

7.3.3 MRI acquisition

All the subjects were scanned twice with an interval of 12 months on the same 3T Siemens Trio MRI scanner at the Queen Square in London. The multi-shell acquisition protocol is the same as the one used in chapter 6.

7.3.4 Preparations of NODDI metric maps

The quality of images was checked manually one volume by one volume as we described in Chapter 4. Only 24 YOAD patients and 17 controls had both NODDI scans that passed the quality control criteria. All the preprocessing steps (eddy-current distortion and motion correction and tissue mask creation) and model fitting are the same as described in Chapter 4. Notably, here we used an optimised longitudinal framework implemented in DTI-TK for spatial normalisation. The details on how to create the longitudinal group specific tensor template are described in Chapter 4. To evaluate the longitudinal progression of white matter damage in YOAD, we also calculated the annualised rate of change in NODDI metrics. The annualised rate of change was computed by (**NODDI metrics at the baseline** - **NODDI metrics at the one-year follow-up**) **/ the interval between the two scans (in months)**.

7.3.5 Statistical analysis

7.3.5.1 The statistics of clinical characteristics

For categorical variables, we used fisher exact test for comparisons between 2 groups and chi-square test for comparisons between 3 groups. And for the continuous scores, we used student t test for the comparisons between two groups and analysis of variance (ANOVA) for the three-group comparisons. All the statistical analyses of the clinical characteristics were performed using Matlab 2016a. Notably, we do not expect there would be a difference in their demographic distribu-

tions at the follow up because the participants were scheduled to be scanned at the same interval of 12 months.

7.3.5.2 The general linear model for group comparison

We used the general linear model (GLM) for all our group comparison analysis. In the GLM, the dependent variable is the NODDI metric of each voxel on the white matter skeleton, and the covariates include gender and age at the baseline. Before putting these two covariates into the GLM, we demeaned the continuous variable of age and then converted it into a vector while for the categorical variable - gender, we binarized the labels with 0 and 1 representing male and female respectively. The main factor is the group type, "YOAD" standing for all the patients and "NC" standing for normal controls.

7.3.5.3 TBSS analysis

As designed in Chapter 4, we used TBSS to identify group differences across the whole brain white matter microstructure using NODDI. We first created white matter skeleton from the group mean FA map in the template space with the default FA threshold (0.2). We then projected the NODDI metric maps at the baseline and the follow-up as well as the annualised rate of change in NODDI metrics onto the white matter skeleton.

After map projection, we used a non-parametric analysis for group comparison - permutation test [278] , and we set up the GLM as we described in section 7.2.5.2. The permutation was performed 5000 times and multiple comparisons were corrected at $p<0.05$ using TFCE [279]. The contrasts of the pairwise comparisons we tested included "NC>YOAD", "NC<YOAD", "NC>APOE ε4-", "NC<APOE ε4-", "NC>APOE ε4+", "NC<APOE ε4+", "APOE ε4+>APOE ε4-", "APOE ε4+<APOE ε4-". Notably, to compare with findings in our cross-sectional study, we also performed the group comparisons of NODDI metrics cross-sectionally at the baseline.

7.4 Results

7.4.1 Demographic

Table 7.1: The Demographic of YOAD patients and controls.

	Controls n=17	YOAD n=24	Statistics
Sex, M:F, n	8:9	8:16	p=0.52
Age at baseline (years), mean/std	60.7/6.3	61.4/5.7	p=0.7

The summary of the demographics of controls and YOAD patients is listed in Table 7.1. There were no significant differences in the age and gender between patients and controls (age, p = 0.7; gender, p = 0.52). In terms of the genotype of APOE ε4, among the 24 YOAD patients, there were 14 APOE ε4+ patients and 10 APOE ε4- patients. The summary of the demographic for YOAD genotypes and controls is listed in Table 7.2. There were no group differences in age across controls and APOE ε4- and APOE ε4+ (p=0.91). There were more female than male in APOE ε4+ but the differences in the gender distributions in the three groups did not reach a significant level (p=0.25). Most of the APOE ε4+ patients (11 out of 14) and APOE ε4- patients (6 out of the 10) presented a 'typical AD' amnestic phenotype while the rest presented an atypical AD - PCA.

Table 7.2: The Demographic of controls and YOAD genotypes of patients.

	Controls n=17	APOE ε4- n=10	APOE ε4+ n=14	Statistics
Sex, M:F, n	8:9	5:5	3:11	p=0.25
Age at baseline (years), mean/std	60.7/6.3	61.2/3.8	61.6/6.9	p=0.91

7.4.2 Group differences between YOAD patients and controls

Compared with controls, we found that YOAD patients had a faster annualised rate of change in NDI (Figure 7.1 A, TFCE corrected $p<0.05$) in temporal, parietal and occipital white matter, fornix, the splenium of corpus callosum, and white matter in the cerebellum. There were no significant group differences in the annualised rate of change in ODI (Figure 7.1 B, TFCE corrected $p<0.05$). Interestingly, we found the annualised rate of change in FISO was bigger in YOAD than in controls, mainly

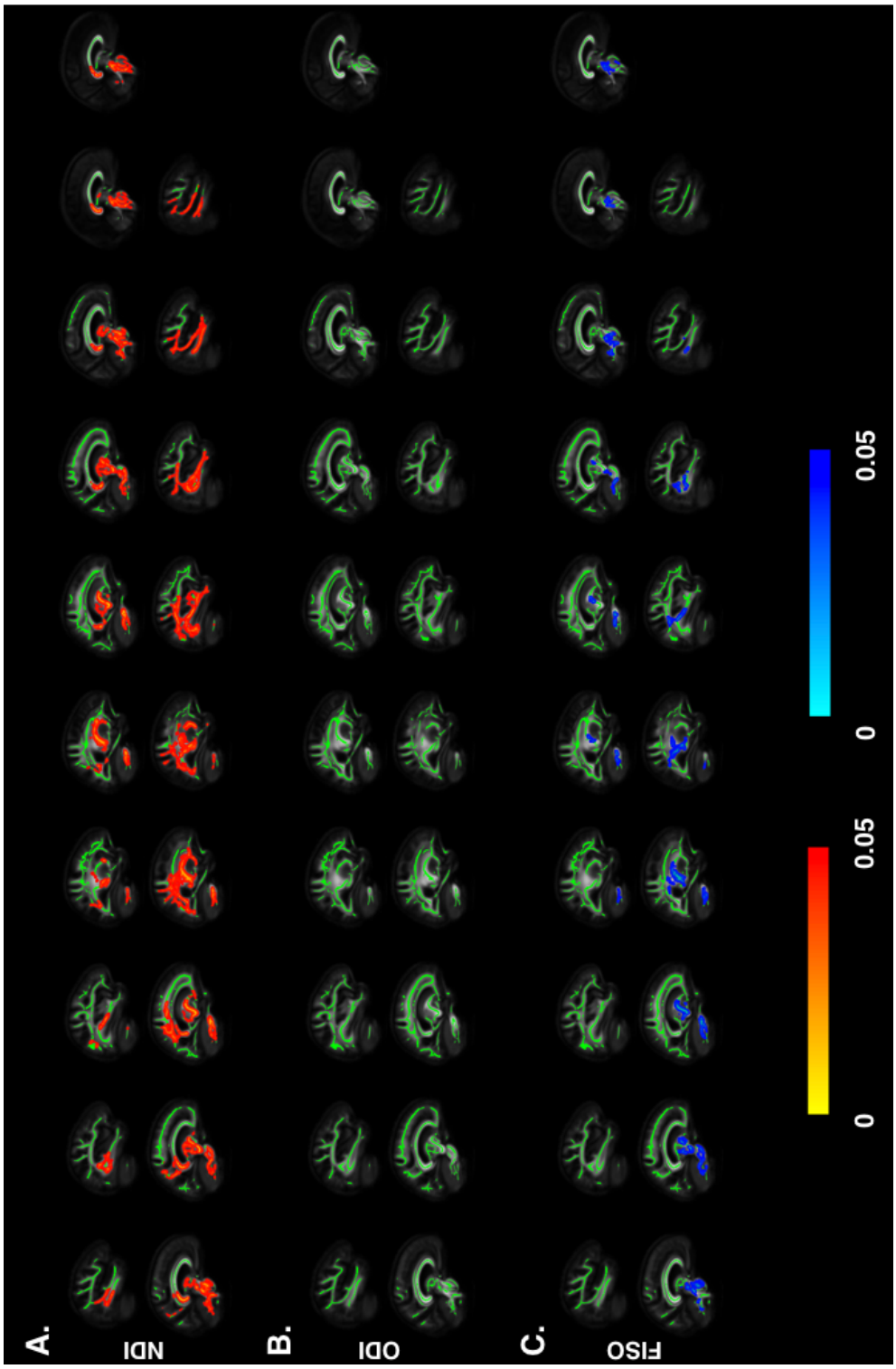

Figure 7.1: Group differences in annualised rate of change of NODDI metrics on the white matter skeleton, tfce corrected $p<0.05$. A. Faster decreasing rate of NDI in YOAD than controls in temporal, parietal and occipital white matter, fornix, the splenium of corpus callosum, and the cerebellar white matter; B. No group differences in the annualised rate of change in ODI between YOAD patients and controls; C. Faster increasing rate of FISO in YOAD patients than controls in mainly involving the temporal white matter, cerebellar white matter, fornix, and brainstem.

involving the temporal white matter, cerebellar white matter, fornix, and brainstem (Figure 7.1 C, TFCE corrected $p<0.05$).

In terms of the group comparisons between YOAD and controls at the baseline,

we identified decreased NDI and decreased ODI as well as increased FISO with a similar pattern (Figure 7.2, TFCE corrected $p<0.05$) as what we found in the cross-sectional study described in Chapter 6.3.3.1.

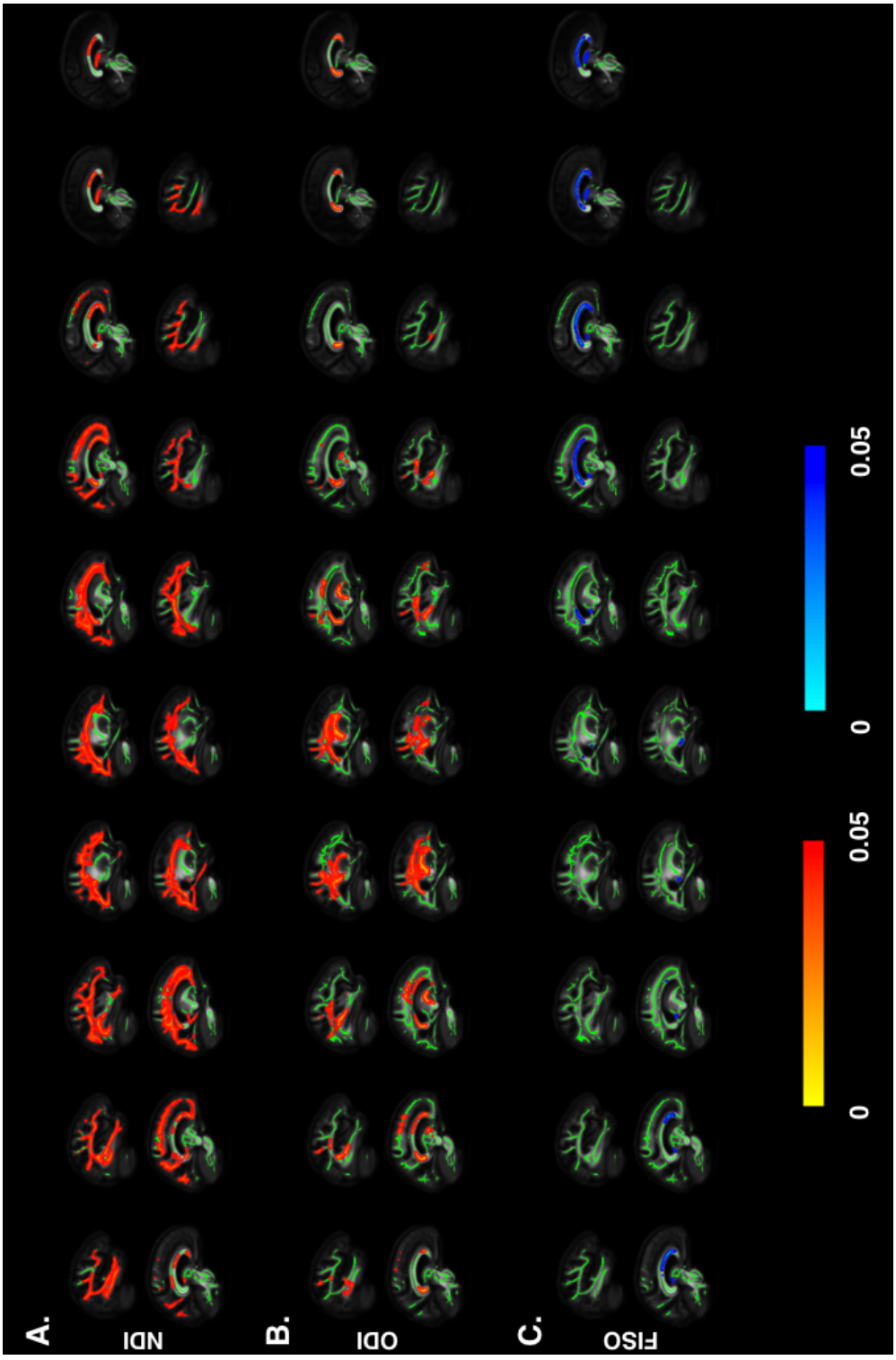

Figure 7.2: Group differences in NODDI metrics at the baseline on the white matter skeleton, tfce corrected $p<0.05$. These group differences in NODDI metrics between YOAD patients and controls showed a similar pattern as what we have found in Chapter 6.3.3.1.

7.4.3 Group differences between YOAD genotypes and controls

The whole brain white matter TBSS analysis between YOAD genotypes and controls showed that both genotypes of YOAD patients had significant differences in annualised rate of change in NODD metrics than controls (TFCE corrected $p<0.05$).

Both genotypes of YOAD patients had faster annualised rate of change in NDI than controls (Figure 7.3, TFCE corrected $p<0.05$). However, there were more white matter tracts involved in APOE ε4+ patients than APOE ε4- patients. For example, in the body of fornix and the splenium of corpus callosum as well as the parietal white matter, APOE ε4+ patients had faster decrease in NDI than controls while there were no significant group differences in annualise rate of change in NDI between APOE ε4- patients and controls (TFCE corrected $p<0.05$). Additionally, there seemed to be a different temporal evolution pattern in the two hemispheres detected by NDI in YOAD genotypes. The differences in annualised rate of change in NDI between APOE ε4- patients and controls showed a much more asymmetrical pattern than those differences between APOE ε4+ patients and controls.

There were no significant group differences in annualised rate of change in ODI between YOAD genotypes and controls (TFCE corrected $p<0.05$).

As for the group differences in the annualised rate of change in FISO, the genotypes of YOAD patients showed a different pattern (Figure 7.4, TFCE corrected $p<0.05$). There were no significant group differences in the annualised rate of change in FISO between APOE ε4- patients and controls while APOE ε4+ patients had a much quicker increase in FISO than controls in the cerebellar and temporal white matter, fornix, and brainstem(TFCE corrected $p<0.05$).

There were no significant group differences in annualised rate of change in any of NODDI metrics between ε4+ and ε4- in the direct group comparisons between these two YOAD genotypes (TFCE corrected $p<0.05$).

In terms of the cross-sectional group comparisons in NODDI metrics between YOAD genotypes and controls at the baseline, we identified decreased NDI (Figure 7.5) and decreased ODI (Figure 7.6) as well as increased FISO (Figure 7.7) in YOAD genotypes compared to controls (TFCE corrected $p<0.05$), which showed a

similar spatial distribution as what we found in Chapter 6.3.4.1.

7.5 Discussion

Our study is the first study that explores the feasibility of NODDI in tracking the longitudinal progression of white matter damage in neurodegenerative diseases. We found that NODDI is sensitive to the longitudinal progression of white matter pathology in YOAD and its association with the APOE $\varepsilon 4$ genotypes. NODDI metrics showed faster annualised rate of change in NDI and FISO in YOAD patients than controls, and the similarities and differences in the disease progression of white matter pathology associated with APOE $\varepsilon 4$ genotype.

The abnormal axonal transport in AD observed in histological studies [170, 201, 326, 332] suggested a role of axon degeneration in Alzheimer's disease. We first observed decreased NDI in YOAD compared to controls in white matter that surrounds the grey matter and the hippocampus at the baseline. We then identified a faster annualised rate of decrease in NDI. These together suggest that the axonal loss might start from those that are close to the well-know AD atrophy in the cortex and the hippocampus but then progress to deep brain structures. It is biologically plausible to connect the reduction in NDI with the changes in axonal density. However, this reduction in NDI may also be because of the demyelination [107]. Although we observed decreased ODI in YOAD patients compared to controls, there were no group differences in the annualised rate of change in ODI between YOAD patients and controls. This suggests that there were alterations in the spatial organisation of axons within those fiber tracts but this alteration did not evolve over a year. Interestingly, we identified increased FISO around the corpus callosum and fornix in YOAD patients compared with controls at the baseline and YOAD patients had a faster annualised rate of increase in FISO in the temporal white matter, cerebellar white matter, fornix, and brainstem. Fornix and corpus callosum are adjacent to the ventricle and therefore can be affected by the enlarged ventricle that is often observed in AD patients [337]. This highlights another advantage of the NODDI model that the estimation of NODDI metrics - NDI and ODI is not contaminated by

the free water content. However, the mechanism of faster rate of FISO increase in cerebellar white matter and brainstem is still clear and worths further investigations.

As for the association between APOE $\varepsilon 4$ genotype and the pattern of longitudinal progression, our findings using NODDI suggest that with APOE $\varepsilon 4$, YOAD patients not only have damages in more white matter areas but also progress faster in more white matter areas. However, there were no significant group differences in the direct comparisons of NODDI metrics between APOE $\varepsilon 4$ genotype subgroups in the pattern of longitudinal progression. This is not surprising, given that the direct comparison in our cross-sectional study in Chapter 6 did not have any significant results either. More samples will be needed in future studies to confirm our findings.

One potential limitation of this study is that as simple biophysical model, NODDI may not capture the complete neurodegenerative process in biological tissue. Secondly, we are not clear if the assumption of the same intrinsic diffusivity of NODDI in patients and controls at the beginning and the end of one year is valid or not. However, there is so far no clear way how to validate this in biological tissue. Additionally, we only have relatively small cohorts of YOAD subgroups with different APOE $\varepsilon 4$ genotypes, and the reproducibility of our findings need further confirmation. Here, we only assessed the differences in the annualised rate of change in NODDI metrics between controls and YOAD. An interesting question we could explore in future is the relationship between the annualised rate of change in NODDI metrics and the annualised rate of change in cognitive and behavioural performances. Moreover, as described in earlier, DTI is a widely-used MRI technique to study the microstructural changes in clinical studies. It is of great interest to investigate in future on the advantage of NODDI over standard DTI in depicting the temporal evolution of white matter pathology in neurodegenerative diseases. Moreover, we did not acquire the genotype information of the normal controls, and our assumption that the distribution of APOE $\varepsilon 4$ status is similar in patients as the controls may not be valid for our cohort. As APOE $\varepsilon 4$ is a factor that has influence on brain microstructure in normal controls [206,324,325]. Therefore, our findings here need confirmations in future studies taking the APOE $\varepsilon 4$ status of normal controls

into consideration. Finally, it would be interesting to investigate the relationship of the grey matter and hippocampal atrophy and the temporal evolution of white matter microstructural abnormalities we observed here in future.

7.6 Conclusion

In this study, we established the feasibility of NODDI in tracking the disease progression in neurodegenerative diseases using YOAD as a disease model. And our findings suggest that NODDI can be a powerful technique of tracking disease progression in Alzheimer′s disease and other neurodegenerative diseases.

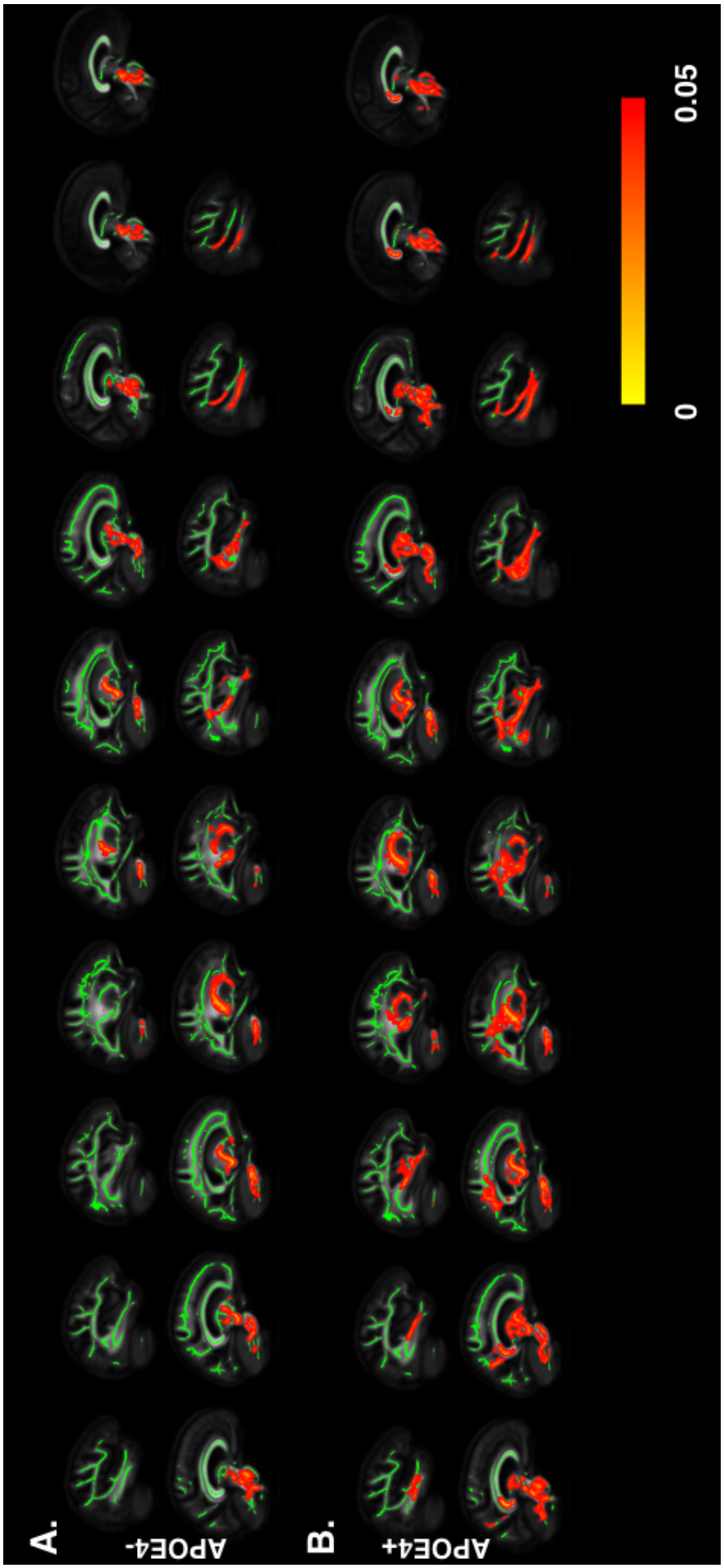

Figure 7.3: Group differences in annualised rate of change of NDI in YOAD genotypes on the white matter skeleton, tfce corrected p<0.05.

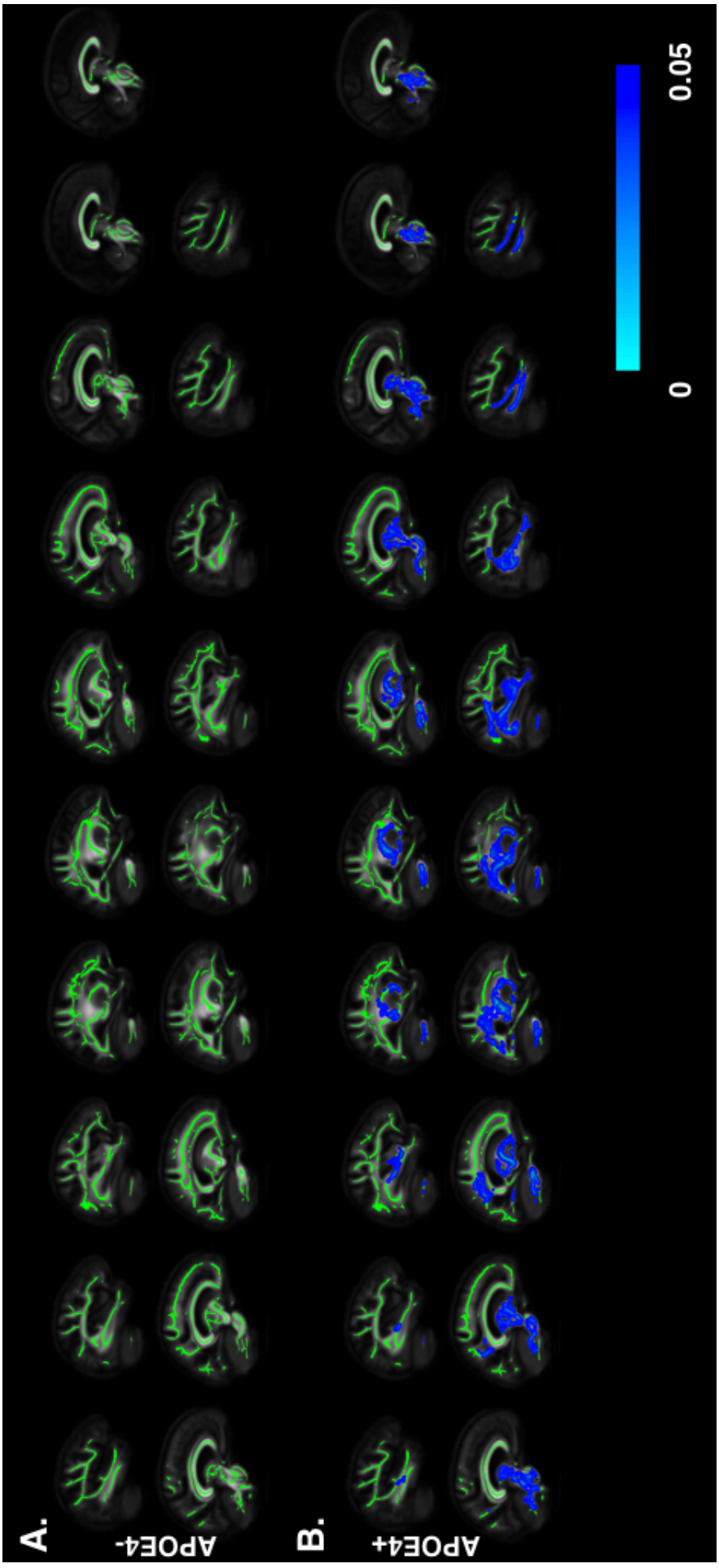

Figure 7.4: Group differences in annualised rate of change of FISO in YOAD genotypes on the white matter skeleton, tfce corrected $p<0.05$.

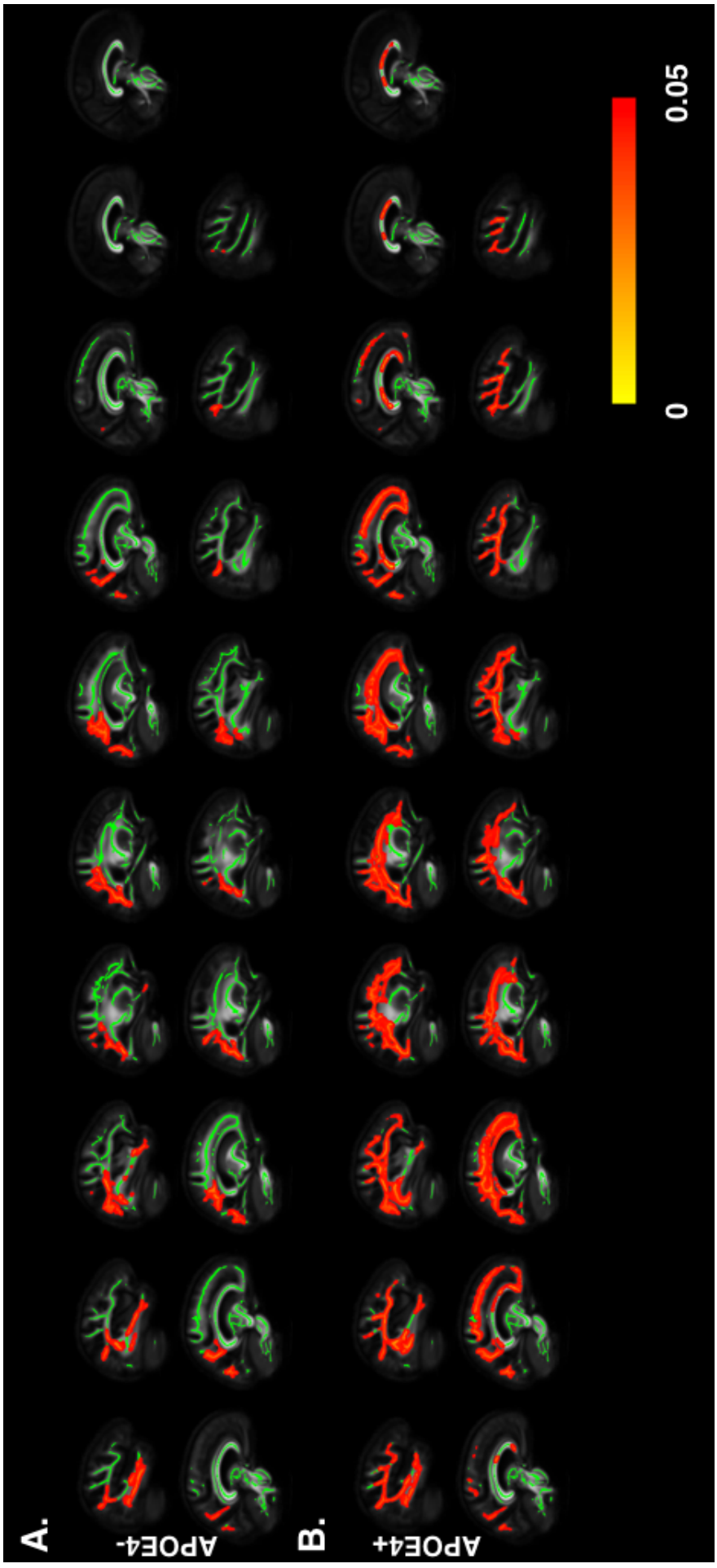

Figure 7.5: Group differences in NDI in YOAD genotypes at the baseline on the white matter skeleton, tfce corrected $p<0.05$.

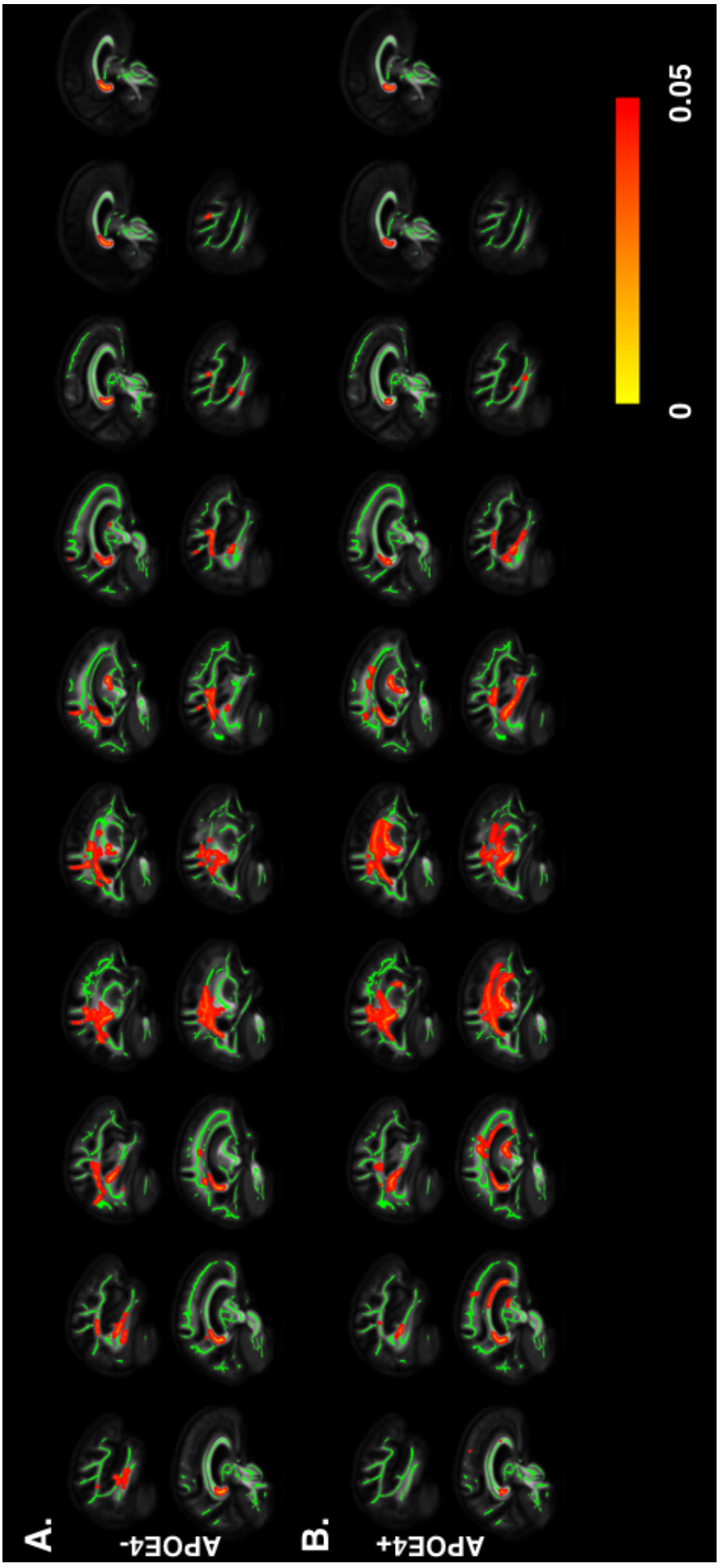

Figure 7.6: Group differences in ODI in YOAD genotypes at the baseline on the white matter skeleton, tfce corrected $p<0.05$.

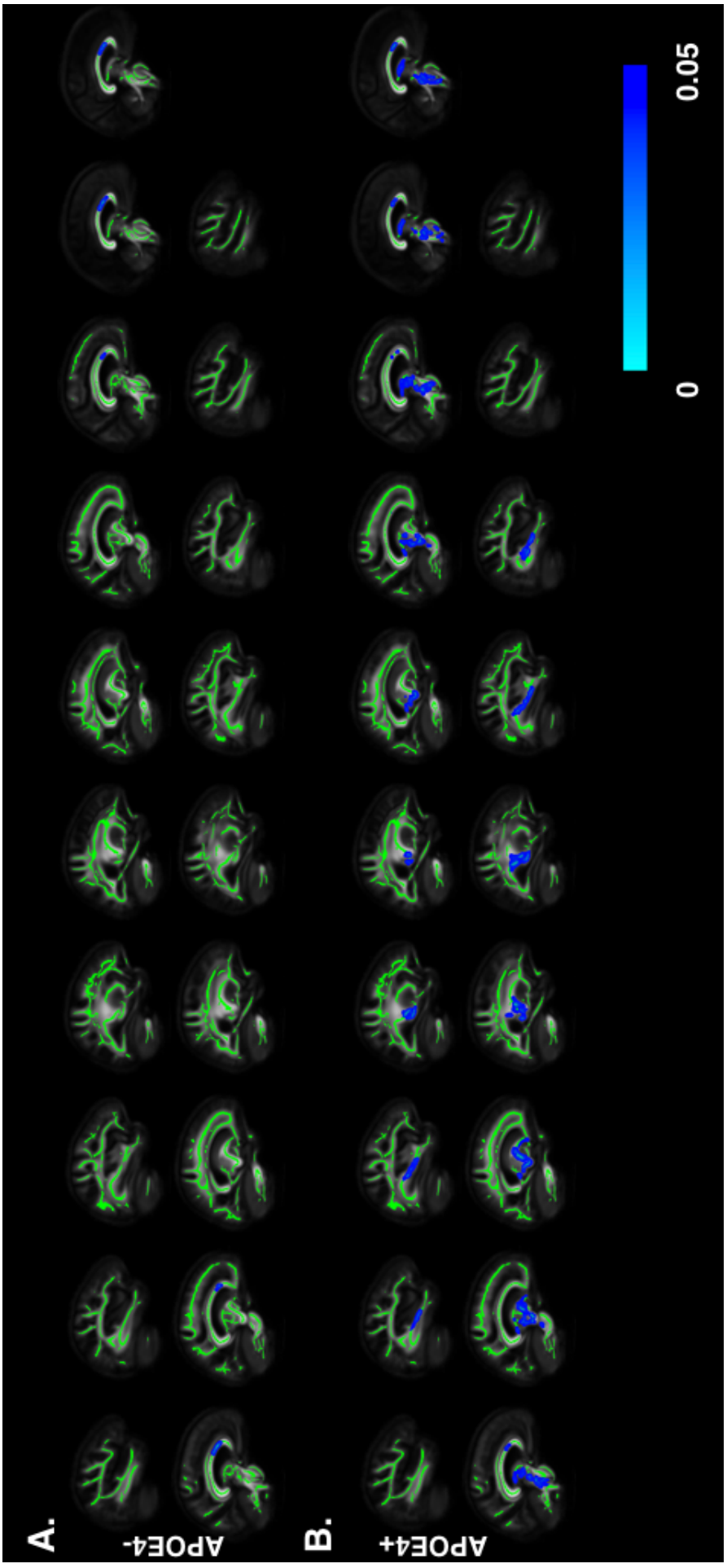

Figure 7.7: Group differences in FISO in YOAD genotypes at the baseline on the white matter skeleton, tfce corrected $p<0.05$.

Chapter 8

Conclusions and Discussions

8.1 The summary

This thesis aimed to evaluate the feasibility of translating advanced diffusion MRI technique - NODDI into characterizing the *in vivo* white matter pathology in neurodegenerative diseases. The tissue-specificity of NODDI allows us to have more plausible explanations of white matter abnormalities than using standard DTI both before and after the disease onset cross-sectionally.

In chapter 4, I discussed the key imaging aspects of designing and conducting a clinical study using NODDI and DTI, and described the image processing pipeline used in all my exploratory experiments.

In chapter 5, I demonstrated the feasibility of NODDI in depicting a detailed picture of the *in vivo* white matter pathology at the pre-manifest stage of neurodegenerative diseases. We applied both NODDI and DTI to study the white matter microstructural abnormalities in a cohort of the pre-manifest HD individuals and controls. With NODDI, we identified that compared with controls, pre-manifest HD individuals had a reduction of NDI in widespread white matter, and decreased ODI within white matter tracts that surround the characteristic atrophy in HD - the basal ganglia. And the NODDI metric - NDI of the corpus callosum correlated with the clinical scores of disease progression. In the same cohort, our DTI findings are consistent with previous studies that pre-manifest HD individuals had increased diffusivities and decreased FA in a large amount of white matter compared with nor-

mal controls. The survival of the significant group differences in NDI but none for DTI metrics at a much stricter threshold may suggest a better sensitivity of NODDI than DTI to the white matter microstructural abnormalities.

In chapter 6, I presented clear evidence of a successful translation of NODDI into studying the *in vivo* white matter pathology at the clinical stage of neurodegenerative diseases. We applied both NODDI and DTI to study the white matter microstructural impairments in young onset AD patients. NODDI revealed a reduction of NDI in widespread white matter in young onset AD patients, compared with controls. And NODDI has the potential to detect differences in the spatial distribution of impaired white matter between young onset AD patients with or without APOEε4. We also found NDI in the parieto-occipital white matter correlated with the performances of the test of visual object and spatial perception battery and the performance intelligence in WASI matrices.

In chapter 7, I established the feasibility of NODDI in tracking the longitudinal progression of the *in vivo* white matter pathology at the clinical stage of neurodegenerative diseases. We applied NODDI to study the progression of *in vivo* white matter pathology in young onset AD at the baseline and the one-year follow-up. We found that compared with controls, young onset AD patients had a faster annualised rate of reduction in NDI and a faster annualised rate of increase in FISO. In addition, And NODDI has the potential to detect differences in the temporal progression of impaired white matter between young onset AD patients with or without APOEε4. Our findings here demonstrate the value of NODDI in revealing the temporal evolution of *in vivo* white matter pathology at the clinical stage of neurodegenerative diseases.

In conclusion, our findings in the experiments of this thesis demonstrate the feasibility of applying this advanced diffusion MRI technique - NODDI in providing a unique window of assessing the *in vivo* white matter pathology and its progression in neurodegenerative diseases.

8.2 Discussions and future work

8.2.1 Image quality control

For MRI images, quality control using visual inspection is now considered to be the gold standard. But it demands a large amount of time, especially for diffusion MRI. In our case, for one subject, the standard DTI dataset has more than 70 volumes, and the NODDI dataset consists of over 100 volumes. The QC for these two datasets of one subject takes more than one hour. If the same applies to large studies such as UK Biobank [338] and Human Connectome Project (HCP) [339], manual checking demands massive amounts of work. In such cases, more than one inspectors have to be involved. This lends to another problem of manual QC - the bias of different inspectors on their subjective standards of image quality.

Recently, there have been advances in the development of automated tools for QC. One kind customises the selected features of a dataset as the criteria for QC [340, 341]. The other kind trains a classifier using the QC outcomes of a subset of the whole datasets as the input and predicts whether a certain diffusion MRI dataset has artefacts or not [342, 343]. Both kinds require a certain amount of preparations on QC and the experience of the inspector who does the preparation is very key. To avoid the manual checking in this preparation step and the potential bias from the inspector, an automated QC framework based on deep learning [344] and a diffusion MRI signal simulator [345] has been proposed [346] and it has been demonstrated to be sensitive to motion artefacts using dHCP datasets [347]. Therefore, it would be interesting to evaluate the value of this tool in such datasets, which might greatly reduce the amount of QC work for future studies.

8.2.2 The potential confounding impact of motion

In all the three experiments presented in this thesis, we have corrected motion using a strategy described in details in Chapter 4.2.2. After motion correction, we have manually checked the images and confirmed that the motion was minimal. However, as one of the neurodegenerative disease models used here - HD is a disease characterised by the disorders of movements, it is important to understand the

potential influence of motion on our results in the pre-manifest HD study.

There are two kinds of motion in MRI images - the translational and rotational motion, and we calculated both motions from the transformation matrix computed during the motion correction. Our findings showed that neither the translational motion or the rotational motion had significant group differences (for translational motion, t=-1.733, $p>0.05$; for rotational motion, t=-0.285, $p>0.05$). Therefore, we do not expect that motion would have any significant impact on our findings of group differences. As for the correlations, there were no significant correlations between the clinical measures (CPO and TMS) and neither of the translational and rotational motion ($p>0.05$). Additionally, there was no significant correlation between rotational motion and NDI in any region of the corpus callosum ($p>0.05$). However, the translational motion had a significant correlation with NDI in the splenium of corpus callosum ($p<0.05$). Therefore, we reanalysed this correlation and found it stayed as significant (r=-0.482, p=0.0039).

8.2.3 Strategies for correcting eddy-current distortion and motion

New post-processing tools such as "eddy" [348] has been demonstrated in realistic data simulated by a framework [345] based on POSSUM [349, 350] to perform better than the most commonly used "eddy_correct". This tool - "eddy" predicts the diffusion weighted signals within each volume without any pre-defined model. By registering all the DWI images acquired to its predictions, we could have a good estimation of the eddy-current distortion and motion artefacts. Even though we used a sequence that minimises the eddy-current distortion, it would be interesting to evaluate whether the choice in this image preprocessing step might have impact on our final conclusions.

8.2.4 Strategies for NODDI fitting

As described in Chapter 4.2.4, the NODDI fitting with the matlab toolbox takes a very long time. Thanks to the high performance cluster provided by the department of computer science at UCL, it did not take me a very long time to finish the NODDI

fitting for all my studies. However, a fast NODDI fitting might greatly benefit other researchers who do not have access to such powerful computing resources. To accelerate the NODDI fitting, a new framework called Accelerated Microstructure Imaging via Convex Optimization (AMICO) [351] was proposed.

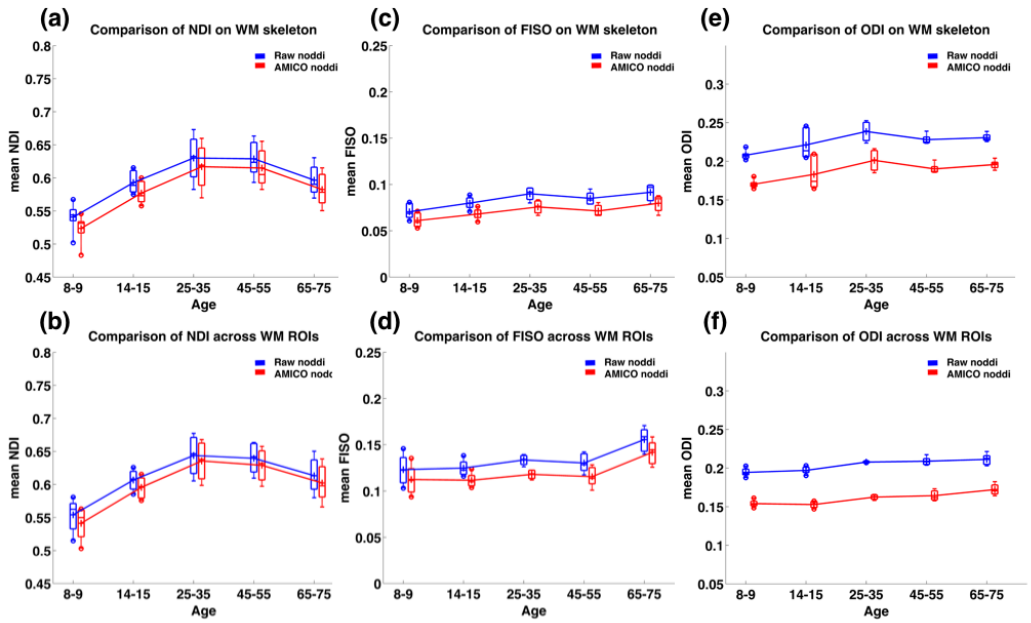

Figure 8.1: The lifespan trajectory of NODDI metrics in white matter with AMICO fitting and the standard fitting.

To test the feasibility of AMICO in a practical neuroimaging study, we explored whether AMICO fitting could provide the same lifespan trajectory of white matter microstructure using NODDI as the standard fitting using matlab toolbox, with a cohort from the Human Connectome Project (HCP) lifespan phase 1a dataset [352]. The details of this study design were described in our previous ISMRM abstract [353]. We extracted the mean NODDI metrics estimated by the AMICO fitting and the original fitting of the white matter skeleton created by TBSS [128] and the core white matter atlas [281]. We found that at both spatial levels, NODDI metrics estimated by AMICO fitting could produce the same lifespan trajectory as the standard fitting using the matlab toolbox (Figure 8.1). This suggests that NODDI

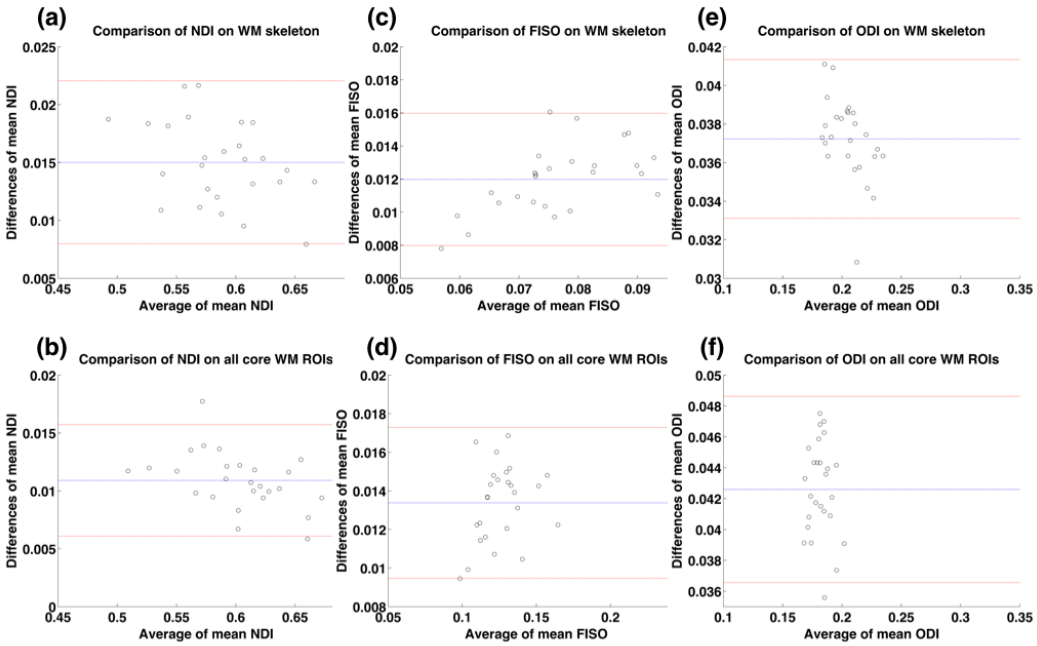

Figure 8.2: The Bland-Altman plots of NODDI metrics in white matter with AMICO fitting and the standard fitting.

metrics estimated by AMICO fitting are highly consistent with those estimated by the standard fitting, which was further confirmed by the high correlations between NODDI metrics estimated by AMICO fitting and those estimated by the standard fitting. For all the mean NODDI metrics of the white matter skeleton, the R^2 were all over 0.97. Meanwhile, for the mean NDI and FISO of the core white matter ROIs, both of the R^2 had a value of over 0.98 while for ODI, the R^2 was 0.88. However, in the Bland-Altman plots, we found that NODDI metrics estimated by AMICO fitting are consistently smaller than those estimated by the standard fitting (Figure 8.2). In terms of the time required to finish the NODDI fitting of a HCP lifespan dataset, the standard NODDI fitting takes about 230 hours while the AMICO fitting takes about one hour. This clearly demonstrates the advantage of AMICO over the standard fitting, especially for high-quality rich datasets and large studies with hundreds or thousands of participants. This time efficiency of AMICO might be the reason why a recent paper studying the ageing of white matter in 3513 UK Biobank

participants [354] has used AMICO fitting instead of the standard fitting.

Additionally, a machine-learning based framework - image quality transfer [355, 356] has been proposed to provide NODDI metric maps based on data acquired with a simple DTI protocol. This method is not only fast in terms of producing NODDI metric maps, but also save the trouble of acquiring multi-shell diffusion MRI datasets. Therefore, it would be of great interest to test whether, in our studies, the NODDI metric maps predicted by this framework could produce similar results as our findings.

8.2.5 The time-dependence of NODDI metrics

The time-dependence of diffusion MRI signals [357] has been studied in both normal and abnormal neural tissue [50, 358, 359]. Interestingly, people found that this time-dependence affects the behaviours of water diffusion in both intra-axonal and extra-axonal compartments [360–362]. Although a variety of diffusion MRI models including NODDI have been proposed to estimate the volume fractions of the intra-axonal and extra-axonal compartments, very few of them have taken the time-dependence of diffusion MRI signals into consideration.

Two recent studies showed that there is an impact of this time-dependence on the NODDI metrics of white matter in both brain and the spinal cord [363, 364]. Incorporating such time-dependence has been shown to improve the estimations of the axon diameter and neurite density in multi-compartment models in the white matter of the brain [361]. This time dependence highlights the importance of setting TE the same for the acquisition of multi-shell datasets. This will make sure the comparability of the NODDI findings across studies. Nevertheless, it would be interesting in future to evaluate this time-dependence of the NODDI metrics in our clinical cohort and identify a time scale that enables the estimated NODDI metrics to maximumly reflect the histological measures of compartment-specific volume fractions.

8.2.6 The limitations of NODDI model

As we described in chapter 2.3.2, there are a few assumptions in NODDI model. These assumptions were made to simplify the model and make it clinical feasible. However, this may bring up a few limitations. First, the single value of intrinsic diffusivity for *in vivo* and *ex vivo* neural tissue may not be plausible in abnormal conditions. This may also be one of the reasons that the estimation of FISO using NODDI seems to be a bit high, compared with the potential impact of *T2*-relaxometry effect [365]. Secondly, it may be questionable how valid the assumption of fast exchange in the extra-cellular compartment across all the orientations is used in NODDI model. Thirdly, NODDI uses a single Watson distribution, which may fail in areas with crossing fibres. Despite this, it has been showed that in white matter areas with crossing fibres, the ODI will decrease when one of the crossing fibres degenerates [103]. Moreover, there has been evidence that white matter in human brain is mostly dominated by dispersed fibres rather than crossing fibres [366]. Lastly, The decrease in NDI may be caused by demyelination in neurodegenerative diseases. The lack of signals contributed from the myelination makes it difficult to conclude that the decrease in NDI is merely caused by the axonal loss. Therefore, we did interpret our results carefully, based on the evidence of abnormal axonal transport in those two neurodegenerative diseases [195–197]. Nevertheless, it can be very meaningful to isolate the effect of demyelination on the reduction in NDI in future.

8.2.7 The reproducibility of NODDI metrics

The reproducibility of NODDI metrics is key for meta-analysis and multi-centre studies as well as longitudinal studies. It has been shown that NODDI metrics have relatively high reproducibility regardless of the external magnetic field strength [367]. And NODDI metrics have comparable reproducibility to those of DTI metrics [368]. Additionally, NODDI metrics were found to be affected by the choice of b value for the outer shell in a multi-shell acquisition scheme [369]. However, all of these studies are case studies, and further confirmations are required in population-based studies.

Bibliography

[1] Anne B Young. Four decades of neurodegenerative disease research: how far we have come! *Journal of Neuroscience*, 29(41):12722–12728, 2009.

[2] Peter J Basser, James Mattiello, and Denis LeBihan. Estimation of the effective self-diffusion tensor from the nmr spin echo. *Journal of Magnetic Resonance, Series B*, 103(3):247–254, 1994.

[3] Peter J Basser, James Mattiello, and Denis LeBihan. Mr diffusion tensor spectroscopy and imaging. *Biophysical journal*, 66(1):259–267, 1994.

[4] Joseph Goveas, Laurence ODwyer, Mario Mascalchi, Mirco Cosottini, Stefano Diciotti, Silvia De Santis, Luca Passamonti, Carlo Tessa, Nicola Toschi, and Marco Giannelli. Diffusion-mri in neurodegenerative disorders. *Magnetic resonance imaging*, 33(7):853–876, 2015.

[5] Yaniv Assaf. Can we use diffusion mri as a bio-marker of neurodegenerative processes? *Bioessays*, 30(11-12):1235–1245, 2008.

[6] Claudia Metzler-Baddeley, Derek K Jones, Michael J O'sullivan, et al. Csf contamination contributes to apparent microstructural alterations in mild cognitive impairment. *Neuroimage*, 92:27–35, 2014.

[7] Hui Zhang, Torben Schneider, Claudia A Wheeler-Kingshott, and Daniel C Alexander. Noddi: practical in vivo neurite orientation dispersion and density imaging of the human brain. *Neuroimage*, 61(4):1000–1016, 2012.

[8] Denis Le Bihan and Heidi Johansen-Berg. Diffusion mri at 25: exploring brain tissue structure and function. *Neuroimage*, 61(2):324–341, 2012.

[9] Robert Brown. Xxvii. a brief account of microscopical observations made in the months of june, july and august 1827, on the particles contained in the pollen of plants; and on the general existence of active molecules in organic and inorganic bodies. *The Philosophical Magazine*, 4(21):161–173, 1828.

[10] GJ Strijkers, MR Drost, and K Nicolay. Diffusion mri: Theory, methods, and applications. In *Diffusion imaging in muscle*. Oxford University Press, 2011.

[11] Albert Einstein. On the motion of small particles suspended in liquids at rest required by the molecular-kinetic theory of heat. *Annalen der physik*, 17:549–560, 1905.

[12] William S Price. Pulsed-field gradient nuclear magnetic resonance as a tool for studying translational diffusion: Part 1. basic theory. *Concepts in Magnetic Resonance Part A*, 9(5):299–336, 1997.

[13] Denis Le Bihan. Diffusion mri: what water tells us about the brain. *EMBO molecular medicine*, page e201404055, 2014.

[14] Daniel C Alexander, Tim B Dyrby, Markus Nilsson, and Hui Zhang. Imaging brain microstructure with diffusion mri: Practicality and applications. *NMR in Biomedicine*, 2017.

[15] I. I. Rabi, J. R. Zacharias, S. Millman, and P. Kusch. A new method of measuring nuclear magnetic moment. *Phys. Rev.*, 53:318–318, Feb 1938.

[16] Edward M Purcell, H Co Torrey, and Robert V Pound. Resonance absorption by nuclear magnetic moments in a solid. *Physical review*, 69(1-2):37, 1946.

[17] PC Lauterbur et al. Image formation by induced local interactions: examples employing nuclear magnetic resonance. 1973.

[18] Joseph Larmor. Lxiii. on the theory of the magnetic influence on spectra; and on the radiation from moving ions. *The London, Edinburgh, and Dublin Philosophical Magazine and Journal of Science*, 44(271):503–512, 1897.

[19] John S Rigden. Quantum states and precession: The two discoveries of nmr. *Reviews of modern physics*, 58(2):433, 1986.

[20] Jinghua Wang, Weihua Mao, Maolin Qiu, Michael B Smith, and R Todd Constable. Factors influencing flip angle mapping in mri: Rf pulse shape, slice-select gradients, off-resonance excitation, and b0 inhomogeneities. *Magnetic resonance in medicine*, 56(2):463–468, 2006.

[21] Felix Bloch. Nuclear induction. *Physical review*, 70(7-8):460, 1946.

[22] M Packard. The nuclear induction experiment. *Physical Review*, 70(7-8):474–485, 1946.

[23] Maurice Goldman. Formal theory of spin–lattice relaxation. *Journal of Magnetic Resonance*, 149(2):160–187, 2001.

[24] Polina Golland. Spatial encoding in mri and how to make it faster. *Massachusetts Institute of Technology, Boston*, 2000.

[25] Joseph P Hornak. The basics of mri. *http://www. cis. rit. edu/htbooks/mri*, 2006.

[26] Edward O Stejskal and John E Tanner. Spin diffusion measurements: spin echoes in the presence of a time-dependent field gradient. *The journal of chemical physics*, 42(1):288–292, 1965.

[27] Erwin L Hahn. Spin echoes. *Physical review*, 80(4):580, 1950.

[28] Erwin L Hahn. Free nuclear induction. *Physics Today*, 6(11):4–9, 1953.

[29] Herman Y Carr and Edward M Purcell. Effects of diffusion on free precession in nuclear magnetic resonance experiments. *Physical review*, 94(3):630, 1954.

[30] Reuben Mezrich. A perspective on k-space. *Radiology*, 195(2):297–315, 1995.

[31] Richard S Likes. Moving gradient zeugmatography, December 22 1981. US Patent 4,307,343.

[32] Stig Ljunggren. A simple graphical representation of fourier-based imaging methods. *Journal of Magnetic Resonance (1969)*, 54(2):338–343, 1983.

[33] Donald B Twieg. The k-trajectory formulation of the nmr imaging process with applications in analysis and synthesis of imaging methods. *Medical physics*, 10(5):610–621, 1983.

[34] Michael K Stehling, Robert Turner, and Peter Mansfield. Echo-planar imaging: magnetic resonance imaging in a fraction of a second. *Science*, 254(5028):43–50, 1991.

[35] P Mansfield and IL Pykett. Biological and medical imaging by nmr. *Journal of Magnetic Resonance (1969)*, 29(2):355–373, 1978.

[36] Denis Le Bihan and E Breton. Imagerie de diffusion in-vivo par résonance magnétique nucléaire. *Comptes-Rendus de l'Académie des Sciences*, 93(5):27–34, 1985.

[37] Denis Le Bihan, Eric Breton, Denis Lallemand, Philippe Grenier, Emmanuel Cabanis, and Maurice Laval-Jeantet. Mr imaging of intravoxel incoherent motions: application to diffusion and perfusion in neurologic disorders. *Radiology*, 161(2):401–407, 1986.

[38] P. T Callaghan. Physics of diffusion. diffusion mri: theory, methods, and applications, 2010.

[39] Denis Le Bihan, Cyril Poupon, Alexis Amadon, and Franck Lethimonnier. Artifacts and pitfalls in diffusion mri. *Journal of Magnetic Resonance Imaging: An Official Journal of the International Society for Magnetic Resonance in Medicine*, 24(3):478–488, 2006.

[40] Minjie Wu, Lin-Ching Chang, Lindsay Walker, Herve Lemaitre, Alan S Barnett, Stefano Marenco, and Carlo Pierpaoli. Comparison of epi distortion

correction methods in diffusion tensor mri using a novel framework. In *International Conference on Medical Image Computing and Computer-Assisted Intervention*, pages 321–329. Springer, 2008.

[41] M Okan Irfanoglu, Pooja Modi, Amritha Nayak, Elizabeth B Hutchinson, Joelle Sarlls, and Carlo Pierpaoli. Dr-buddi (diffeomorphic registration for blip-up blip-down diffusion imaging) method for correcting echo planar imaging distortions. *NeuroImage*, 106:284–299, 2015.

[42] Jesper LR Andersson, Stefan Skare, and John Ashburner. How to correct susceptibility distortions in spin-echo echo-planar images: application to diffusion tensor imaging. *Neuroimage*, 20(2):870–888, 2003.

[43] John N Morelli, Val M Runge, Fei Ai, Ulrike Attenberger, Lan Vu, Stuart H Schmeets, Wolfgang R Nitz, and John E Kirsch. An image-based approach to understanding the physics of mr artifacts. *Radiographics*, 31(3):849–866, 2011.

[44] Klaus-Dietmar Merboldt, Wolfgang Hanicke, and Jens Frahm. Self-diffusion nmr imaging using stimulated echoes. *Journal of Magnetic Resonance (1969)*, 64(3):479–486, 1985.

[45] DG Taylor and MC Bushell. The spatial mapping of translational diffusion coefficients by the nmr imaging technique. *Physics in Medicine & Biology*, 30(4):345, 1985.

[46] Lauren J O'Donnell, Alessandro Daducci, Demian Wassermann, and Christophe Lenglet. Advances in computational and statistical diffusion mri. *NMR in Biomedicine*, 2017.

[47] Uran Ferizi, Benoit Scherrer, Torben Schneider, Mohammad Alipoor, Odin Eufracio, Rutger HJ Fick, Rachid Deriche, Markus Nilsson, Ana K Loya-Olivas, Mariano Rivera, et al. Diffusion mri microstructure models with in vivo human brain connectome data: results from a multi-group comparison. *NMR in Biomedicine*, 30(9), 2017.

[48] Andrada Savickas. *Advanced diffusion MRI for microstructure imaging: theoretical developments*. PhD thesis, UCL (University College London), 2016.

[49] Eleftheria Panagiotaki, Torben Schneider, Bernard Siow, Matt G Hall, Mark F Lythgoe, and Daniel C Alexander. Compartment models of the diffusion mr signal in brain white matter: a taxonomy and comparison. *Neuroimage*, 59(3):2241–2254, 2012.

[50] Greg J Stanisz, Graham A Wright, R Mark Henkelman, and Aaron Szafer. An analytical model of restricted diffusion in bovine optic nerve. *Magnetic Resonance in Medicine*, 37(1):103–111, 1997.

[51] Markus Nilsson, Danielle van Westen, Freddy Ståhlberg, Pia C Sundgren, and Jimmy Lätt. The role of tissue microstructure and water exchange in biophysical modelling of diffusion in white matter. *Magnetic Resonance Materials in Physics, Biology and Medicine*, 26(4):345–370, 2013.

[52] Partha P Mitra, Pabitra N Sen, Lawrence M Schwartz, and Pierre Le Doussal. Diffusion propagator as a probe of the structure of porous media. *Physical review letters*, 68(24):3555, 1992.

[53] Timothy EJ Behrens, Mark W Woolrich, Mark Jenkinson, Heidi Johansen-Berg, Rita G Nunes, Stuart Clare, Paul M Matthews, J Michael Brady, and Stephen M Smith. Characterization and propagation of uncertainty in diffusion-weighted mr imaging. *Magnetic resonance in medicine*, 50(5):1077–1088, 2003.

[54] Yaniv Assaf and Peter J Basser. Composite hindered and restricted model of diffusion (charmed) mr imaging of the human brain. *Neuroimage*, 27(1):48–58, 2005.

[55] Sune N Jespersen, Christopher D Kroenke, Leif Østergaard, Joseph JH Ackerman, and Dmitriy A Yablonskiy. Modeling dendrite density from magnetic resonance diffusion measurements. *Neuroimage*, 34(4):1473–1486, 2007.

[56] Sune N Jespersen, Carsten R Bjarkam, Jens R Nyengaard, M Mallar Chakravarty, Brian Hansen, Thomas Vosegaard, Leif Østergaard, Dmitriy Yablonskiy, Niels Chr Nielsen, and Peter Vestergaard-Poulsen. Neurite density from magnetic resonance diffusion measurements at ultrahigh field: comparison with light microscopy and electron microscopy. *Neuroimage*, 49(1):205–216, 2010.

[57] Daniel C Alexander, Penny L Hubbard, Matt G Hall, Elizabeth A Moore, Maurice Ptito, Geoff JM Parker, and Tim B Dyrby. Orientationally invariant indices of axon diameter and density from diffusion mri. *Neuroimage*, 52(4):1374–1389, 2010.

[58] Tim B Dyrby, Matt G Hall, Maurice Ptito, Daniel Alexander, et al. Contrast and stability of the axon diameter index from microstructure imaging with diffusion mri. *Magnetic Resonance in Medicine*, 70(3):711–721, 2013.

[59] Stamatios N Sotiropoulos, Timothy EJ Behrens, and Saad Jbabdi. Ball and rackets: inferring fiber fanning from diffusion-weighted mri. *Neuroimage*, 60(2):1412–1425, 2012.

[60] Benoit Scherrer, Armin Schwartzman, Maxime Taquet, Mustafa Sahin, Sanjay P Prabhu, and Simon K Warfield. Characterizing brain tissue by assessment of the distribution of anisotropic microstructural environments in diffusion-compartment imaging (diamond). *Magnetic resonance in medicine*, 76(3):963–977, 2016.

[61] Enrico Kaden, Nathaniel D Kelm, Robert P Carson, Mark D Does, and Daniel C Alexander. Multi-compartment microscopic diffusion imaging. *NeuroImage*, 139:346–359, 2016.

[62] Chunlei Liu, Roland Bammer, and Michael E Moseley. Generalized diffusion tensor imaging (gdti): A method for characterizing and imaging diffusion anisotropy caused by non-gaussian diffusion. *Israel Journal of Chemistry*, 43(1-2):145–154, 2003.

[63] David S Tuch. Q-ball imaging. *Magnetic resonance in medicine*, 52(6):1358–1372, 2004.

[64] Jens H Jensen, Joseph A Helpern, Anita Ramani, Hanzhang Lu, and Kyle Kaczynski. Diffusional kurtosis imaging: The quantification of non-gaussian water diffusion by means of magnetic resonance imaging. *Magnetic resonance in medicine*, 53(6):1432–1440, 2005.

[65] Maxime Descoteaux, Elaine Angelino, Shaun Fitzgibbons, and Rachid Deriche. Regularized, fast, and robust analytical q-ball imaging. *Magnetic resonance in medicine*, 58(3):497–510, 2007.

[66] Haz-Edine Assemlal, David Tschumperlé, and Luc Brun. Efficient and robust computation of pdf features from diffusion mr signal. *Medical image analysis*, 13(5):715–729, 2009.

[67] Dmitriy A Yablonskiy and Alexander L Sukstanskii. Theoretical models of the diffusion weighted mr signal. *NMR in Biomedicine*, 23(7):661–681, 2010.

[68] Valerij G Kiselev. The cumulant expansion: an overarching mathematical framework for understanding diffusion nmr. *Diffusion MRI*, pages 152–168, 2010.

[69] E Özarslan, CG Koay, and PJ Basser. Simple harmonic oscillator based estimation and reconstruction for one-dimensional q-space mr. In *Proc. Intl. Soc. Mag. Reson. Med*, volume 16, page 35, 2008.

[70] Evren Özarslan, Cheng Guan Koay, Timothy M Shepherd, Michal E Komlosh, M Okan İrfanoğlu, Carlo Pierpaoli, and Peter J Basser. Mean apparent propagator (map) mri: a novel diffusion imaging method for mapping tissue microstructure. *NeuroImage*, 78:16–32, 2013.

[71] J-Donald Tournier, Fernando Calamante, David G Gadian, and Alan Connelly. Direct estimation of the fiber orientation density function from

diffusion-weighted mri data using spherical deconvolution. *NeuroImage*, 23(3):1176–1185, 2004.

[72] Daniel C Alexander. Maximum entropy spherical deconvolution for diffusion mri. In *Biennial International Conference on Information Processing in Medical Imaging*, pages 76–87. Springer, 2005.

[73] Adam W Anderson. Measurement of fiber orientation distributions using high angular resolution diffusion imaging. *Magnetic resonance in medicine*, 54(5):1194–1206, 2005.

[74] Bing Jian and Baba C Vemuri. Multi-fiber reconstruction from diffusion mri using mixture of wisharts and sparse deconvolution. In *Biennial International Conference on Information Processing in Medical Imaging*, pages 384–395. Springer, 2007.

[75] Bing Jian, Baba C Vemuri, Evren Özarslan, Paul R Carney, and Thomas H Mareci. A novel tensor distribution model for the diffusion-weighted mr signal. *NeuroImage*, 37(1):164–176, 2007.

[76] Ken E Sakaie and Mark J Lowe. An objective method for regularization of fiber orientation distributions derived from diffusion-weighted mri. *NeuroImage*, 34(1):169–176, 2007.

[77] Flavio Dell'Acqua, Giovanna Rizzo, Paola Scifo, Rafael Alonso Clarke, Giuseppe Scotti, and Ferruccio Fazio. A model-based deconvolution approach to solve fiber crossing in diffusion-weighted mr imaging. *IEEE Transactions on Biomedical Engineering*, 54(3):462–472, 2007.

[78] Saad Jbabdi, Stamatios N Sotiropoulos, Alexander M Savio, Manuel Graña, and Timothy EJ Behrens. Model-based analysis of multishell diffusion mr data for tractography: How to get over fitting problems. *Magnetic Resonance in Medicine*, 68(6):1846–1855, 2012.

[79] Yogesh Rathi, O Michailovich, F Laun, Kawin Setsompop, P Ellen Grant, and C-F Westin. Multi-shell diffusion signal recovery from sparse measurements. *Medical image analysis*, 18(7):1143–1156, 2014.

[80] Uran Ferizi, Torben Schneider, Eleftheria Panagiotaki, Gemma Nedjati-Gilani, Hui Zhang, Claudia AM Wheeler-Kingshott, and Daniel C Alexander. A ranking of diffusion mri compartment models with in vivo human brain data. *Magnetic resonance in medicine*, 72(6):1785–1792, 2014.

[81] Enrico Kaden, Frithjof Kruggel, and Daniel C Alexander. Quantitative mapping of the per-axon diffusion coefficients in brain white matter. *Magnetic resonance in medicine*, 75(4):1752–1763, 2016.

[82] Denis Le Bihan. Apparent diffusion coefficient and beyond: what diffusion mr imaging can tell us about tissue structure, 2013.

[83] Denis Le Bihan, Jean-François Mangin, Cyril Poupon, Chris A Clark, Sabina Pappata, Nicolas Molko, and Hughes Chabriat. Diffusion tensor imaging: concepts and applications. *Journal of magnetic resonance imaging*, 13(4):534–546, 2001.

[84] Terence C Chua, Wei Wen, Melissa J Slavin, and Perminder S Sachdev. Diffusion tensor imaging in mild cognitive impairment and alzheimer's disease: a review. *Current opinion in neurology*, 21(1):83–92, 2008.

[85] Adriaan RE Potgieser, Michiel Wagemakers, Arjen LJ van Hulzen, Bauke M de Jong, Eelco W Hoving, and Rob JM Groen. The role of diffusion tensor imaging in brain tumor surgery: a review of the literature. *Clinical neurology and neurosurgery*, 124:51–58, 2014.

[86] Cyril Atkinson-Clement, Serge Pinto, Alexandre Eusebio, and Olivier Coulon. Diffusion tensor imaging in parkinson's disease: Review and meta-analysis. *NeuroImage: Clinical*, 16:98–110, 2017.

[87] Breton Michael Asken, Steven T DeKosky, James R Clugston, Michael S Jaffee, and Russell M Bauer. Diffusion tensor imaging (dti) findings in adult civilian, military, and sport-related mild traumatic brain injury (mtbi): a systematic critical review. *Brain imaging and behavior*, pages 1–28, 2017.

[88] Cyrus Eierud, R Cameron Craddock, Sean Fletcher, Manek Aulakh, Brooks King-Casas, Damon Kuehl, and Stephen M LaConte. Neuroimaging after mild traumatic brain injury: review and meta-analysis. *NeuroImage: Clinical*, 4:283–294, 2014.

[89] Edrea Khong, Nicole Odenwald, Eyesha Hashim, and Michael D Cusimano. Diffusion tensor imaging findings in post-concussion syndrome patients after mild traumatic brain injury: a systematic review. *Frontiers in neurology*, 7:156, 2016.

[90] Derek K Jones, Thomas R Knösche, and Robert Turner. White matter integrity, fiber count, and other fallacies: the do's and don'ts of diffusion mri. *Neuroimage*, 73:239–254, 2013.

[91] Pawel J Winklewski, Agnieszka Sabisz, Patrycja Naumczyk, Krzysztof Jodzio, Edyta Szurowska, and Arkadiusz Szarmach. Understanding the physiopathology behind axial and radial diffusivity changeswhat do we know? *Frontiers in neurology*, 9:92, 2018.

[92] Claudia AM Wheeler-Kingshott and Mara Cercignani. About axial and radial diffusivities. *Magnetic resonance in medicine*, 61(5):1255–1260, 2009.

[93] Nan-Jie Gong, Chun-Sing Wong, Chun-Chung Chan, Lam-Ming Leung, and Yiu-Ching Chu. Aging in deep gray matter and white matter revealed by diffusional kurtosis imaging. *Neurobiology of aging*, 35(10):2203–2216, 2014.

[94] Jean-Philippe Coutu, J Jean Chen, H Diana Rosas, and David H Salat. Non-gaussian water diffusion in aging white matter. *Neurobiology of aging*, 35(6):1412–1421, 2014.

[95] C-Y Lee, Ali Tabesh, Maria V Spampinato, Joseph A Helpern, Jens H Jensen, and Leonardo Bonilha. Diffusional kurtosis imaging reveals a distinctive pattern of microstructural alternations in idiopathic generalized epilepsy. *Acta Neurologica Scandinavica*, 130(3):148–155, 2014.

[96] L Bonilha, C-Y Lee, JH Jensen, A Tabesh, MV Spampinato, JC Edwards, J Breedlove, and JA Helpern. Altered microstructure in temporal lobe epilepsy: a diffusional kurtosis imaging study. *American Journal of Neuroradiology*, 36(4):719–724, 2015.

[97] Peter Raab, Elke Hattingen, Kea Franz, Friedhelm E Zanella, and Heinrich Lanfermann. Cerebral gliomas: diffusional kurtosis imaging analysis of microstructural differences. *Radiology*, 254(3):876–881, 2010.

[98] Rifeng Jiang, Jingjing Jiang, Lingyun Zhao, Jiaxuan Zhang, Shun Zhang, Yihao Yao, Shiqi Yang, Jingjing Shi, Nanxi Shen, Changliang Su, et al. Diffusion kurtosis imaging can efficiently assess the glioma grade and cellular proliferation. *Oncotarget*, 6(39):42380, 2015.

[99] Yaniv Assaf, Raisa Z Freidlin, Gustavo K Rohde, and Peter J Basser. New modeling and experimental framework to characterize hindered and restricted water diffusion in brain white matter. *Magnetic Resonance in Medicine*, 52(5):965–978, 2004.

[100] Daniel Barazany, Peter J Basser, and Yaniv Assaf. In vivo measurement of axon diameter distribution in the corpus callosum of rat brain. *Brain*, 132(5):1210–1220, 2009.

[101] Yaniv Assaf, Tamar Blumenfeld-Katzir, Yossi Yovel, and Peter J Basser. Axcaliber: a method for measuring axon diameter distribution from diffusion mri. *Magnetic resonance in medicine*, 59(6):1347–1354, 2008.

[102] Daniel C Alexander. A general framework for experiment design in diffusion mri and its application in measuring direct tissue-microstructure features. *Magnetic Resonance in Medicine*, 60(2):439–448, 2008.

[103] Maira Tariq, Torben Schneider, Daniel C Alexander, Claudia A Gandini Wheeler-Kingshott, and Hui Zhang. Bingham–noddi: mapping anisotropic orientation dispersion of neurites using diffusion mri. *NeuroImage*, 133:207–223, 2016.

[104] JÖRG KÄRGER, Harry Pfeifer, and Wilfried Heink. Principles and application of self-diffusion measurements by nuclear magnetic resonance. In *Advances in Magnetic and optical resonance*, volume 12, pages 1–89. Elsevier, 1988.

[105] Samo Lasič, Markus Nilsson, Jimmy Lätt, Freddy Ståhlberg, and Daniel Topgaard. Apparent exchange rate mapping with diffusion mri. *Magnetic resonance in medicine*, 66(2):356–365, 2011.

[106] Gemma L Nedjati-Gilani, Torben Schneider, Matt G Hall, Niamh Cawley, Ioana Hill, Olga Ciccarelli, Ivana Drobnjak, Claudia AM Gandini Wheeler-Kingshott, and Daniel C Alexander. Machine learning based compartment models with permeability for white matter microstructure imaging. *NeuroImage*, 150:119–135, 2017.

[107] Francesco Grussu, Torben Schneider, Carmen Tur, Richard L Yates, Mohamed Tachrount, Andrada Ianuş, Marios C Yiannakas, Jia Newcombe, Hui Zhang, Daniel C Alexander, et al. Neurite dispersion: a new marker of multiple sclerosis spinal cord pathology? *Annals of clinical and translational neurology*, 4(9):663–679, 2017.

[108] Mark Jenkinson, Christian F Beckmann, Timothy EJ Behrens, Mark W Woolrich, and Stephen M Smith. Fsl. *Neuroimage*, 62(2):782–790, 2012.

[109] Hangyi Jiang, Peter CM Van Zijl, Jinsuh Kim, Godfrey D Pearlson, and Susumu Mori. Dtistudio: resource program for diffusion tensor computation and fiber bundle tracking. *Computer methods and programs in biomedicine*, 81(2):106–116, 2006.

[110] PA Cook, Y Bai, SKKS Nedjati-Gilani, KK Seunarine, MG Hall, GJ Parker, and DC Alexander. Camino: open-source diffusion-mri reconstruction and processing. In *14th scientific meeting of the international society for magnetic resonance in medicine*, volume 2759, page 2759. Seattle WA, USA, 2006.

[111] Hui Zhang, Penny L Hubbard, Geoff JM Parker, and Daniel C Alexander. Axon diameter mapping in the presence of orientation dispersion with diffusion mri. *Neuroimage*, 56(3):1301–1315, 2011.

[112] Catherine Lebel, Lindsay Walker, Alexander Leemans, Linda Phillips, and Christian Beaulieu. Microstructural maturation of the human brain from childhood to adulthood. *Neuroimage*, 40(3):1044–1055, 2008.

[113] Tony J Simon, Lijun Ding, Joel P Bish, Donna M McDonald-McGinn, Elaine H Zackai, and James Gee. Volumetric, connective, and morphologic changes in the brains of children with chromosome 22q11. 2 deletion syndrome: an integrative study. *Neuroimage*, 25(1):169–180, 2005.

[114] FJ Rugg-Gunn, SH Eriksson, MR Symms, GJ Barker, and JS Duncan. Diffusion tensor imaging of cryptogenic and acquired partial epilepsies. *Brain*, 124(3):627–636, 2001.

[115] SHm Eriksson, FJ Rugg-Gunn, MR Symms, GJ Barker, and JS Duncan. Diffusion tensor imaging in patients with epilepsy and malformations of cortical development. *Brain*, 124(3):617–626, 2001.

[116] Naama Barnea-Goraly, Stephan Eliez, Maj Hedeus, Vinod Menon, Christopher D White, Michael Moseley, and Allan L Reiss. White matter tract alterations in fragile x syndrome: preliminary evidence from diffusion tensor imaging. *American Journal of Medical Genetics Part B: Neuropsychiatric Genetics*, 118(1):81–88, 2003.

[117] C Büchel, T Raedler, M Sommer, M Sach, C Weiller, and MA Koch. White matter asymmetry in the human brain: a diffusion tensor mri study. *Cerebral cortex*, 14(9):945–951, 2004.

[118] John Ashburner and Karl J Friston. Voxel-based morphometrythe methods. *Neuroimage*, 11(6):805–821, 2000.

[119] Catriona D Good, Ingrid S Johnsrude, John Ashburner, Richard NA Henson, Karl J Friston, and Richard SJ Frackowiak. A voxel-based morphometric study of ageing in 465 normal adult human brains. *Neuroimage*, 14(1):21–36, 2001.

[120] Fred L Bookstein. voxel-based morphometry should not be used with imperfectly registered images. *Neuroimage*, 14(6):1454–1462, 2001.

[121] John Ashburner and Karl J Friston. Why voxel-based morphometry should be used. *Neuroimage*, 14(6):1238–1243, 2001.

[122] Christos Davatzikos. Why voxel-based morphometric analysis should be used with great caution when characterizing group differences. *Neuroimage*, 23(1):17–20, 2004.

[123] KJ Friston and J Ashburner. Generative and recognition models for neuroanatomy. *Neuroimage*, 23(1):21–24, 2004.

[124] Derek K Jones, Lewis D Griffin, Daniel C Alexander, Marco Catani, Mark A Horsfield, Robert Howard, and Steve CR Williams. Spatial normalization and averaging of diffusion tensor mri data sets. *Neuroimage*, 17(2):592–617, 2002.

[125] Hae-Jeong Park, Marek Kubicki, Martha E Shenton, Alexandre Guimond, Robert W McCarley, Stephan E Maier, Ron Kikinis, Ferenc A Jolesz, and Carl-Fredrik Westin. Spatial normalization of diffusion tensor mri using multiple channels. *Neuroimage*, 20(4):1995–2009, 2003.

[126] Hae-Jeong Park, Carl-Fredrik Westin, Marek Kubicki, Stephan E Maier, Margaret Niznikiewicz, Aaron Baer, Melissa Frumin, Ron Kikinis, Ferenc A Jolesz, Robert W McCarley, et al. White matter hemisphere asymmetries in healthy subjects and in schizophrenia: a diffusion tensor mri study. *Neuroimage*, 23(1):213–223, 2004.

[127] Derek K Jones, Mark R Symms, Mara Cercignani, and Robert J Howard. The effect of filter size on vbm analyses of dt-mri data. *Neuroimage*, 26(2):546–554, 2005.

[128] Stephen M Smith, Mark Jenkinson, Heidi Johansen-Berg, Daniel Rueckert, Thomas E Nichols, Clare E Mackay, Kate E Watkins, Olga Ciccarelli, M Zaheer Cader, Paul M Matthews, et al. Tract-based spatial statistics: voxelwise analysis of multi-subject diffusion data. *Neuroimage*, 31(4):1487–1505, 2006.

[129] Ben Jeurissen, Maxime Descoteaux, Susumu Mori, and Alexander Leemans. Diffusion mri fiber tractography of the brain. *NMR in Biomedicine*, 2017.

[130] Thomas E Conturo, Nicolas F Lori, Thomas S Cull, Erbil Akbudak, Abraham Z Snyder, Joshua S Shimony, Robert C McKinstry, Harold Burton, and Marcus E Raichle. Tracking neuronal fiber pathways in the living human brain. *Proceedings of the National Academy of Sciences*, 96(18):10422–10427, 1999.

[131] Susumu Mori, Barbara J Crain, Vadappuram P Chacko, and Peter CM Van Zijl. Three-dimensional tracking of axonal projections in the brain by magnetic resonance imaging. *Annals of Neurology: Official Journal of the American Neurological Association and the Child Neurology Society*, 45(2):265–269, 1999.

[132] Geoffrey JM Parker, Hamied A Haroon, and Claudia AM Wheeler-Kingshott. A framework for a streamline-based probabilistic index of con-

nectivity (pico) using a structural interpretation of mri diffusion measurements. *Journal of Magnetic Resonance Imaging*, 18(2):242–254, 2003.

[133] Andreia V Faria, Jiangyang Zhang, Kenichi Oishi, Xin Li, Hangyi Jiang, Kazi Akhter, Laurent Hermoye, Seung-Koo Lee, Alexander Hoon, Elaine Stashinko, et al. Atlas-based analysis of neurodevelopment from infancy to adulthood using diffusion tensor imaging and applications for automated abnormality detection. *Neuroimage*, 52(2):415–428, 2010.

[134] Derek K Jones. Challenges and limitations of quantifying brain connectivity in vivo with diffusion mri. *Imaging in Medicine*, 2(3):341, 2010.

[135] Saad Jbabdi and Heidi Johansen-Berg. Tractography: where do we go from here? *Brain connectivity*, 1(3):169–183, 2011.

[136] Types of glia. `https://qbi.uq.edu.au/brain-basics/brain/brain-physiology/types-glia`, 2017.

[137] Robin JM Franklin et al. Regenerating cns myelinfrom mechanisms to experimental medicines. *Nature Reviews Neuroscience*, 18(12):753, 2017.

[138] SG Waxman and MVL Bennett. Relative conduction velocities of small myelinated and non-myelinated fibres in the central nervous system. *Nature New Biology*, 238(85):217, 1972.

[139] János A Perge, Kristin Koch, Robert Miller, Peter Sterling, and Vijay Balasubramanian. How the optic nerve allocates space, energy capacity, and information. *Journal of Neuroscience*, 29(24):7917–7928, 2009.

[140] Almut Schüz and Valentino Braitenberg. The human cortical white matter: quantitative aspects of cortico-cortical long-range connectivity. *Cortical areas: Unity and diversity*, pages 377–385, 2002.

[141] Francisco Aboitiz, Arnold B Scheibel, Robin S Fisher, and Eran Zaidel. Fiber composition of the human corpus callosum. *Brain research*, 598(1-2):143–153, 1992.

[142] A-S LaMantia and P Rakic. Cytological and quantitative characteristics of four cerebral commissures in the rhesus monkey. *Journal of Comparative Neurology*, 291(4):520–537, 1990.

[143] Henry H Ong, Alex C Wright, Suzanne L Wehrli, Andre Souza, Eric D Schwartz, Scott N Hwang, and Felix W Wehrli. Indirect measurement of regional axon diameter in excised mouse spinal cord with q-space imaging: simulation and experimental studies. *Neuroimage*, 40(4):1619–1632, 2008.

[144] Roberto Caminiti, Hassan Ghaziri, Ralf Galuske, Patrick R Hof, and Giorgio M Innocenti. Evolution amplified processing with temporally dispersed slow neuronal connectivity in primates. *Proceedings of the National Academy of Sciences*, pages pnas–0907655106, 2009.

[145] Jesper Riise and Bente Pakkenberg. Stereological estimation of the total number of myelinated callosal fibers in human subjects. *Journal of anatomy*, 218(3):277–284, 2011.

[146] AK Stark and B Pakkenberg. Histological changes of the dopaminergic nigrostriatal system in aging. *Cell and tissue research*, 318(1):81–92, 2004.

[147] Bruce D Trapp, John Peterson, Richard M Ransohoff, Richard Rudick, Sverre Mörk, and Lars Bö. Axonal transection in the lesions of multiple sclerosis. *New England Journal of Medicine*, 338(5):278–285, 1998.

[148] Anette K Stark, Dorte P Pelvig, Anne-Marie B Jorgensen, Birgitte B Andersen, and Bente Pakkenberg. Measuring morphological and cellular changes in alzheimer's dementia: a review emphasizing stereology. *Current Alzheimer research*, 2(4):449–481, 2005.

[149] Mitesh Patel. Multiple sclerosis: Microstructural pathology imaged in ms. *Nature Reviews Neurology*, 13(10):578, 2017.

[150] Clare M OConnor, Jill U Adams, and Jennifer Fairman. Essentials of cell biology. *Cambridge: NPG Education*, 2010.

[151] Keiichiro Susuki. Myelin: a specialized membrane for cell communication. *Nature Education*, 3(9):59, 2010.

[152] George Jed Siegel. *Basic neurochemistry: molecular, cellular and medical aspects*. Number V360 SIEb. 1999.

[153] Bruce R Ranson, Aninda B Acharya, and Mark P Goldberg. Molecular pathophysiology of white matter anoxic-ischemic injury. In *Stroke (Fourth Edition)*, pages 867–881. Elsevier, 2004.

[154] Sarah Jäkel and Leda Dimou. Glial cells and their function in the adult brain: a journey through the history of their ablation. *Frontiers in cellular neuroscience*, 11:24, 2017.

[155] Alfonso Araque and Marta Navarrete. Glial cells in neuronal network function. *Philosophical Transactions of the Royal Society of London B: Biological Sciences*, 365(1551):2375–2381, 2010.

[156] Eva Syková and Charles Nicholson. Diffusion in brain extracellular space. *Physiological reviews*, 88(4):1277–1340, 2008.

[157] Jean-Christophe Houzel, Chantal Milleret, and Giorgio Innocenti. Morphology of callosal axons interconnecting areas 17 and 18 of the cat. *European Journal of Neuroscience*, 6(6):898–917, 1994.

[158] Denis Le Bihan, Eric Breton, Denis Lallemand, ML Aubin, J Vignaud, and M Laval-Jeantet. Separation of diffusion and perfusion in intravoxel incoherent motion mr imaging. *Radiology*, 168(2):497–505, 1988.

[159] M Catani. The functional anatomy of white matter: from postmortem dissections to in vivo virtual tractography. *Diffusion MRI: theory, methods and applications*, pages 5–18, 2010.

[160] T Meynert. Psychiatry: A clinical treatise on diseases of the fore-brain based upon a study of its structure, functions and nutrition, trans. *B. Sachs, New York: G. P. Putnams Sons*, 1885.

[161] Serge Przedborski, Miquel Vila, and Vernice Jackson-Lewis. Series introduction: Neurodegeneration: What is it and where are we? *The Journal of clinical investigation*, 111(1):3–10, 2003.

[162] Claudio Soto. Unfolding the role of protein misfolding in neurodegenerative diseases. *Nature Reviews Neuroscience*, 4(1):49, 2003.

[163] A summary of ad in europe. `http://www.neurodegenerationresearch.eu/about/`.

[164] Joseph B Martin. Molecular basis of the neurodegenerative disorders. *New England Journal of Medicine*, 340(25):1970–1980, 1999.

[165] Gerardo A Morfini, Matthew Burns, Lester I Binder, Nicholas M Kanaan, Nichole LaPointe, Daryl A Bosco, Robert H Brown, Hannah Brown, Ashutosh Tiwari, Lawrence Hayward, et al. Axonal transport defects in neurodegenerative diseases. *Journal of Neuroscience*, 29(41):12776–12786, 2009.

[166] Erica Chevalier-Larsen and Erika LF Holzbaur. Axonal transport and neurodegenerative disease. *Biochimica et Biophysica Acta (BBA)-Molecular Basis of Disease*, 1762(11-12):1094–1108, 2006.

[167] Christopher A Ross, Elizabeth H Aylward, Edward J Wild, Douglas R Langbehn, Jeffrey D Long, John H Warner, Rachael I Scahill, Blair R Leavitt, Julie C Stout, Jane S Paulsen, et al. Huntington disease: natural history, biomarkers and prospects for therapeutics. *Nature Reviews Neurology*, 10(4):204, 2014.

[168] R_ Sherrington, EI Rogaev, Y al Liang, EA Rogaeva, G Levesque, M Ikeda, H Chi, C Lin, G Li, K Holman, et al. Cloning of a gene bearing missense mutations in early-onset familial alzheimer's disease. *Nature*, 375(6534):754, 1995.

[169] Lars Bertram and Rudolph E Tanzi. Thirty years of alzheimer's disease genetics: the implications of systematic meta-analyses. *Nature Reviews Neuroscience*, 9(10):768, 2008.

[170] Robert W Mahley, Karl H Weisgraber, and Yadong Huang. Apolipoprotein e4: a causative factor and therapeutic target in neuropathology, including alzheimers disease. *Proceedings of the National Academy of Sciences*, 103(15):5644–5651, 2006.

[171] Thomas Gasser. Update on the genetics of parkinson's disease. *Movement disorders: official journal of the Movement Disorder Society*, 22(S17):S343–S350, 2007.

[172] Elisabeth Koss, S Edland, G Fillenbaum, R Mohs, C Clark, D Galasko, and JC Morris. Clinical and neuropsychological differences between patients with earlier and later onset of alzheimer's disease a cerad analysis, part xii. *Neurology*, 46(1):136–141, 1996.

[173] AE Van der Vlies, ELGE Koedam, YAL Pijnenburg, JWR Twisk, P Scheltens, and WM Van der Flier. Most rapid cognitive decline in apoe $\varepsilon 4$ negative alzheimer's disease with early onset. *Psychological medicine*, 39(11):1907–1911, 2009.

[174] Diane Jacobs, M Sano, K Marder, K Bell, F Bylsma, G Lafleche, M Albert, J Brandt, and Y Stern. Age at onset of alzheimer's disease relation to pattern of cognitive dysfunction and rate of decline. *Neurology*, 44(7):1215–1215, 1994.

[175] Peter McColgan and Sarah J Tabrizi. Huntington's disease: a clinical review. *European journal of neurology*, 25(1):24–34, 2018.

[176] David C Rubinsztein, Jayne Leggo, Rhian Coles, Elisabeth Almqvist, Valerie Biancalana, Jean-Jacques Cassiman, Kokila Chotai, Margaret Connarty, David Craufurd, Anne Curtis, et al. Phenotypic characterization of individuals with 30–40 cag repeats in the huntington disease (hd) gene reveals hd

cases with 36 repeats and apparently normal elderly individuals with 36–39 repeats. *American journal of human genetics*, 59(1):16, 1996.

[177] Marina Papoutsi, Izelle Labuschagne, Sarah J Tabrizi, and Julie C Stout. The cognitive burden in huntington's disease: pathology, phenotype, and mechanisms of compensation. *Movement Disorders*, 29(5):673–683, 2014.

[178] Sarah J Tabrizi, Rachael I Scahill, Alexandra Durr, Raymund AC Roos, Blair R Leavitt, Rebecca Jones, G Bernhard Landwehrmeyer, Nick C Fox, Hans Johnson, Stephen L Hicks, et al. Biological and clinical changes in premanifest and early stage huntington's disease in the track-hd study: the 12-month longitudinal analysis. *The Lancet Neurology*, 10(1):31–42, 2011.

[179] Julie C Stout, Rebecca Jones, Izelle Labuschagne, Alison M O'regan, Miranda J Say, Eve M Dumas, Sarah Queller, Damian Justo, Rachelle Dar Santos, Allison Coleman, et al. Evaluation of longitudinal 12 and 24 month cognitive outcomes in premanifest and early huntington's disease. *J Neurol Neurosurg Psychiatry*, 83(7):687–694, 2012.

[180] Sarah J Tabrizi, Rachael I Scahill, Gail Owen, Alexandra Durr, Blair R Leavitt, Raymund A Roos, Beth Borowsky, Bernhard Landwehrmeyer, Chris Frost, Hans Johnson, et al. Predictors of phenotypic progression and disease onset in premanifest and early-stage huntington's disease in the track-hd study: analysis of 36-month observational data. *The Lancet Neurology*, 12(7):637–649, 2013.

[181] David Craufurd, Jennifer C Thompson, and Julie S Snowden. Behavioral changes in huntington disease. *Cognitive and Behavioral Neurology*, 14(4):219–226, 2001.

[182] Sarah J Tabrizi, Douglas R Langbehn, Blair R Leavitt, Raymund AC Roos, Alexandra Durr, David Craufurd, Christopher Kennard, Stephen L Hicks, Nick C Fox, Rachael I Scahill, et al. Biological and clinical manifestations

of huntington's disease in the longitudinal track-hd study: cross-sectional analysis of baseline data. *The Lancet Neurology*, 8(9):791–801, 2009.

[183] Erik van Duijn, David Craufurd, Anna AM Hubers, Erik J Giltay, Raphael Bonelli, Hugh Rickards, Karen E Anderson, Marleen R van Walsem, Rose C van der Mast, Michael Orth, et al. Neuropsychiatric symptoms in a european huntington's disease cohort (registry). *J Neurol Neurosurg Psychiatry*, pages jnnp–2013, 2014.

[184] DL Bachman, Philip A Wolf, RT Linn, JE Knoefel, JL Cobb, AJ Belanger, LR White, and RB D'agostino. Incidence of dementia and probable alzheimer's disease in a general population the framingham study. *Neurology*, 43(3 Part 1):515–515, 1993.

[185] Liesi E Hebert, Paul A Scherr, Laurel A Beckett, Marilyn S Albert, David M Pilgrim, Marilyn J Chown, H Harris Funkenstein, and Denis A Evans. Age-specific incidence of alzheimer's disease in a community population. *Jama*, 273(17):1354–1359, 1995.

[186] Denis A Evans, David A Bennett, Robert S Wilson, Julia L Bienias, Martha Clare Morris, Paul A Scherr, Liesi E Hebert, Neelum Aggarwal, Laurel A Beckett, Rajiv Joglekar, et al. Incidence of alzheimer disease in a biracial urban community: relation to apolipoprotein e allele status. *Archives of neurology*, 60(2):185–189, 2003.

[187] Claudia Kawas, S Gray, R Brookmeyer, J Fozard, and A Zonderman. Age-specific incidence rates of alzheimers disease the baltimore longitudinal study of aging. *Neurology*, 54(11):2072–2077, 2000.

[188] Dennis J Selkoe. Alzheimer's disease: genes, proteins, and therapy. *Physiological reviews*, 81(2):741–766, 2001.

[189] Colin L. Masters, Randall Bateman, Kaj Blennow, Christopher C. Rowe, Reisa A. Sperling, and Jeffrey L. Cummings. Alzheimer's disease. *Nature Reviews. Disease Primers*, 1:15056, 2015.

[190] Martin N Rossor, Nick C Fox, Catherine J Mummery, Jonathan M Schott, and Jason D Warren. The diagnosis of young-onset dementia. *The Lancet Neurology*, 9(8):793–806, 2010.

[191] EH Bigio, LS Hynan, E Sontag, S Satumtira, and CL White III. Synapse loss is greater in presenile than senile onset alzheimer disease: implications for the cognitive reserve hypothesis. *Neuropathology and applied neurobiology*, 28(3):218–227, 2002.

[192] R Adalbert and MP Coleman. Axon pathology in age-related neurodegenerative disorders. *Neuropathology and applied neurobiology*, 39(2):90–108, 2013.

[193] Natalia Salvadores, Mario Sanhueza, Patricio Manque, et al. Axonal degeneration during aging and its functional role in neurodegenerative disorders. *Frontiers in neuroscience*, 11:451, 2017.

[194] G Pigino, G Morfini, Y Atagi, A Deshpande, C Yu, L Jungbauer, M LaDu, J Busciglio, and S Brady. Disruption of fast axonal transport is a pathogenic mechanism for intraneuronal amyloid beta. *Proceedings of the National Academy of Sciences*, 106(14):5907–5912, 2009.

[195] Gerardo Morfini, Györgyi Szebenyi, Ravindhra Elluru, Nancy Ratner, and Scott T Brady. Glycogen synthase kinase 3 phosphorylates kinesin light chains and negatively regulates kinesin-based motility. *The EMBO journal*, 21(3):281–293, 2002.

[196] Gustavo Pigino, Gerardo Morfini, Alejandra Pelsman, Mark P Mattson, Scott T Brady, and Jorge Busciglio. Alzheimer's presenilin 1 mutations impair kinesin-based axonal transport. *Journal of Neuroscience*, 23(11):4499–4508, 2003.

[197] Györgyi Szebenyi, Gerardo A Morfini, Alyssa Babcock, Milena Gould, Kimberly Selkoe, David L Stenoien, Maureen Young, Pieter W Faber, Marcy E

MacDonald, Michael J McPhaul, et al. Neuropathogenic forms of huntingtin and androgen receptor inhibit fast axonal transport. *Neuron*, 40(1):41–52, 2003.

[198] G Morfini, G Pigino, K Opalach, Y Serulle, JE Moreira, M Sugimori, RR Llinas, and ST Brady. 1-methyl-4-phenylpyridinium affects fast axonal transport by activation of caspase and protein kinase c. *Proceedings of the National Academy of Sciences*, 104(7):2442–2447, 2007.

[199] Scott Brady, George Siegel, R Wayne Albers, and Donald Price. *Basic neurochemistry: principles of molecular, cellular, and medical neurobiology*. Academic press, 2011.

[200] Shermali Gunawardena, Lu-Shiun Her, Richard G Brusch, Robert A Laymon, Ingrid R Niesman, Beth Gordesky-Gold, Louis Sintasath, Nancy M Bonini, and Lawrence SB Goldstein. Disruption of axonal transport by loss of huntingtin or expression of pathogenic polyq proteins in drosophila. *Neuron*, 40(1):25–40, 2003.

[201] Gorazd B Stokin, Concepción Lillo, Tomás L Falzone, Richard G Brusch, Edward Rockenstein, Stephanie L Mount, Rema Raman, Peter Davies, Eliezer Masliah, David S Williams, et al. Axonopathy and transport deficits early in the pathogenesis of alzheimer's disease. *Science*, 307(5713):1282–1288, 2005.

[202] Adeela Kamal and Lawrence SB Goldstein. Connecting vesicle transport to the cytoskeleton. *Current opinion in cell biology*, 12(4):503–508, 2000.

[203] Heidi Johansen-Berg and Timothy EJ Behrens. *Diffusion MRI: from quantitative measurement to in vivo neuroanatomy*. Academic Press, 2013.

[204] Marcia Radanovic, Fabrício Ramos Silvestre Pereira, Florindo Stella, Ivan Aprahamian, Luiz Kobuti Ferreira, Orestes Vicente Forlenza, and Geraldo F Busatto. White matter abnormalities associated with alzheimers disease and

mild cognitive impairment: a critical review of mri studies. *Expert review of neurotherapeutics*, 13(5):483–493, 2013.

[205] Mario Mascalchi, Francesco Lolli, Riccardo Della Nave, Carlo Tessa, Raffaele Petralli, Cinzia Gavazzi, Letterio S Politi, Marco Macucci, Massimo Filippi, and Silvia Piacentini. Huntington disease: volumetric, diffusion-weighted, and magnetization transfer mr imaging of brain. *Radiology*, 232(3):867–873, 2004.

[206] Brian T Gold, Nathan F Johnson, David K Powell, and Charles D Smith. White matter integrity and vulnerability to alzheimer's disease: preliminary findings and future directions. *Biochimica et Biophysica Acta (BBA)-Molecular Basis of Disease*, 1822(3):416–422, 2012.

[207] Stefan T Schwarz, Maryam Abaei, Vamsi Gontu, Paul S Morgan, Nin Bajaj, and Dorothee P Auer. Diffusion tensor imaging of nigral degeneration in parkinson's disease: a region-of-interest and voxel-based study at 3t and systematic review with meta-analysis. *NeuroImage: Clinical*, 3:481–488, 2013.

[208] Julie M Hall, Kaylena A Ehgoetz Martens, Courtney C Walton, Claire O'Callaghan, Peter E Keller, Simon JG Lewis, and Ahmed A Moustafa. Diffusion alterations associated with parkinson's disease symptomatology: a review of the literature. *Parkinsonism & related disorders*, 33:12–26, 2016.

[209] Michela Pievani, Nicola Filippini, Martijn P Van Den Heuvel, Stefano F Cappa, and Giovanni B Frisoni. Brain connectivity in neurodegenerative diseasesfrom phenotype to proteinopathy. *Nature Reviews Neurology*, 10(11):620, 2014.

[210] Olga Ciccarelli, Marco Catani, Heidi Johansen-Berg, Chris Clark, and Alan Thompson. Diffusion-based tractography in neurological disorders: concepts, applications, and future developments. *The Lancet Neurology*, 7(8):715–727, 2008.

[211] Alex Fornito, Andrew Zalesky, and Michael Breakspear. The connectomics of brain disorders. *Nature Reviews Neuroscience*, 16(3):159, 2015.

[212] Yong He, Zhang Chen, Gaolang Gong, and Alan Evans. Neuronal networks in alzheimer's disease. *The Neuroscientist*, 15(4):333–350, 2009.

[213] Cornelis J Stam. Modern network science of neurological disorders. *Nature Reviews Neuroscience*, 15(10):683, 2014.

[214] Betty M Tijms, Alle Meije Wink, Willem de Haan, Wiesje M van der Flier, Cornelis J Stam, Philip Scheltens, and Frederik Barkhof. Alzheimer's disease: connecting findings from graph theoretical studies of brain networks. *Neurobiology of aging*, 34(8):2023–2036, 2013.

[215] Claire J Cochrane and Klaus P Ebmeier. Diffusion tensor imaging in parkinsonian syndromes: a systematic review and meta-analysis. *Neurology*, 80(9):857–864, 2013.

[216] Frederick JA Meijer, Bastiaan R Bloem, Philipp Mahlknecht, Klaus Seppi, and Bozena Goraj. Update on diffusion mri in parkinson's disease and atypical parkinsonism. *Journal of the neurological sciences*, 332(1-2):21–29, 2013.

[217] Klaus Seppi and Werner Poewe. Brain magnetic resonance imaging techniques in the diagnosis of parkinsonian syndromes. *Neuroimaging Clinics*, 20(1):29–55, 2010.

[218] Lilia Mesrob, Marie Sarazin, Valerie Hahn-Barma, Leonardo Cruz de Souza, Bruno Dubois, Patrick Gallinari, and Serge Kinkingnéhun. Dti and structural mri classification in alzheimers disease. *Advances in molecular imaging*, 2(02):12, 2012.

[219] Wook Lee, Byungkyu Park, and Kyungsook Han. Classification of diffusion tensor images for the early detection of alzheimer's disease. *Computers in Biology and Medicine*, 43(10):1313–1320, 2013.

[220] Graziella Orru, William Pettersson-Yeo, Andre F Marquand, Giuseppe Sartori, and Andrea Mechelli. Using support vector machine to identify imaging biomarkers of neurological and psychiatric disease: a critical review. *Neuroscience & Biobehavioral Reviews*, 36(4):1140–1152, 2012.

[221] Stefan Klöppel, Bogdan Draganski, Charlotte V Golding, Carlton Chu, Zoltan Nagy, Philip A Cook, Stephen L Hicks, Christopher Kennard, Daniel C Alexander, Geoff JM Parker, et al. White matter connections reflect changes in voluntary-guided saccades in pre-symptomatic huntington's disease. *Brain*, 131(1):196–204, 2007.

[222] Nellie Georgiou-Karistianis, Anusha Sritharan, Hamed Asadi, Leigh Johnston, Andrew Churchyard, and Gary Egan. Diffusion tensor imaging in huntingtons disease reveals distinct patterns of white matter degeneration associated with motor and cognitive deficits. *Brain imaging and behavior*, 5(3):171–180, 2011.

[223] Peter McColgan, Kiran K Seunarine, Sarah Gregory, Adeel Razi, Marina Papoutsi, Jeffrey D Long, James A Mills, Eileanoir Johnson, Alexandra Durr, Raymund AC Roos, et al. Topological length of white matter connections predicts their rate of atrophy in premanifest huntingtons disease. *JCI insight*, 2(8), 2017.

[224] Helen E Crawford, Nicola Z Hobbs, Ruth Keogh, Douglas R Langbehn, Chris Frost, Hans Johnson, Bernhard Landwehrmeyer, Ralf Reilmann, David Craufurd, Julie C Stout, et al. Corpus callosal atrophy in premanifest and early huntington's disease. *Journal of Huntington's disease*, 2(4):517–526, 2013.

[225] Marianne JU Novak, Kiran K Seunarine, Clare R Gibbard, Nicola Z Hobbs, Rachael I Scahill, Chris A Clark, and Sarah J Tabrizi. White matter integrity in premanifest and early huntington's disease is related to caudate loss and disease progression. *Cortex*, 52:98–112, 2014.

[226] Federica Agosta, Michela Pievani, Stefania Sala, Cristina Geroldi, Samantha Galluzzi, Giovanni B Frisoni, and Massimo Filippi. White matter damage in alzheimer disease and its relationship to gray matter atrophy. *Radiology*, 258(3):853–863, 2011.

[227] IK Amlien and AM Fjell. Diffusion tensor imaging of white matter degeneration in alzheimers disease and mild cognitive impairment. *Neuroscience*, 276:206–215, 2014.

[228] Claire E Sexton, Ukwuori G Kalu, Nicola Filippini, Clare E Mackay, and Klaus P Ebmeier. A meta-analysis of diffusion tensor imaging in mild cognitive impairment and alzheimer's disease. *Neurobiology of aging*, 32(12):2322–e5, 2011.

[229] GT Stebbins and CM Murphy. Diffusion tensor imaging in alzheimer's disease and mild cognitive impairment. *Behavioural neurology*, 21(1, 2):39–49, 2009.

[230] Travis R Stoub, Bradford C Dickerson, et al. Parahippocampal white matter volume predicts alzheimer's disease risk in cognitively normal old adults. *Neurobiology of aging*, 35(8):1855–1861, 2014.

[231] Soichiro Kitamura, Kuniaki Kiuchi, Toshiaki Taoka, Kazumichi Hashimoto, Shotaro Ueda, Fumihiko Yasuno, Masayuki Morikawa, Kimihiko Kichikawa, and Toshifumi Kishimoto. Longitudinal white matter changes in alzheimer's disease: a tractography-based analysis study. *Brain research*, 1515:12–18, 2013.

[232] Sila Genc, Christopher E Steward, Charles B Malpas, Dennis Velakoulis, Terence J O'brien, and Patricia M Desmond. Short-term white matter alterations in alzheimer's disease characterized by diffusion tensor imaging. *Journal of Magnetic Resonance Imaging*, 43(3):627–634, 2016.

[233] Milap A Nowrangi, Constantine G Lyketsos, Jeannie-Marie S Leoutsakos, Kenichi Oishi, Marilyn Albert, Susumu Mori, and Michelle M Mielke. Lon-

gitudinal, region-specific course of diffusion tensor imaging measures in mild cognitive impairment and alzheimers disease. *Alzheimer's & Dementia*, 9(5):519–528, 2013.

[234] Chantel D Mayo, Erin L Mazerolle, Lesley Ritchie, John D Fisk, Jodie R Gawryluk, Alzheimer's Disease Neuroimaging Initiative, et al. Longitudinal changes in microstructural white matter metrics in alzheimer's disease. *NeuroImage: Clinical*, 13:330–338, 2017.

[235] P Mukherjee, SW Chung, JI Berman, CP Hess, and RG Henry. Diffusion tensor mr imaging and fiber tractography: technical considerations. *American Journal of Neuroradiology*, 29(5):843–852, 2008.

[236] Khader M Hasan, Dennis L Parker, and Andrew L Alexander. Comparison of gradient encoding schemes for diffusion-tensor mri. *Journal of Magnetic Resonance Imaging: An Official Journal of the International Society for Magnetic Resonance in Medicine*, 13(5):769–780, 2001.

[237] Lin-Ching Chang, Cheng Guan Koay, Carlo Pierpaoli, and Peter J Basser. Variance of estimated dti-derived parameters via first-order perturbation methods. *Magnetic Resonance in Medicine: An Official Journal of the International Society for Magnetic Resonance in Medicine*, 57(1):141–149, 2007.

[238] Derek K Jones, Mark A Horsfield, and Andrew Simmons. Optimal strategies for measuring diffusion in anisotropic systems by magnetic resonance imaging. *Magnetic Resonance in Medicine: An Official Journal of the International Society for Magnetic Resonance in Medicine*, 42(3):515–525, 1999.

[239] Derek K Jones. The effect of gradient sampling schemes on measures derived from diffusion tensor mri: a monte carlo study. *Magnetic Resonance in Medicine: An Official Journal of the International Society for Magnetic Resonance in Medicine*, 51(4):807–815, 2004.

[240] Nikolaos G Papadakis, Chris D Murrills, Laurance D Hall, Christopher L-H Huang, and T Adrian Carpenter. Minimal gradient encoding for robust

estimation of diffusion anisotropy. *Magnetic resonance imaging*, 18(6):671–679, 2000.

[241] Nikolaos G Papadakis, Da Xing, Christopher L-H Huang, Laurance D Hall, and T Adrian Carpenter. A comparative study of acquisition schemes for diffusion tensor imaging using mri. *Journal of Magnetic Resonance*, 137(1):67–82, 1999.

[242] Stefan Skare, Maj Hedehus, Michael E Moseley, and Tie-Qiang Li. Condition number as a measure of noise performance of diffusion tensor data acquisition schemes with mri. *Journal of Magnetic Resonance*, 147(2):340–352, 2000.

[243] PG Batchelor, D Atkinson, DLG Hill, F Calamante, and A Connelly. Anisotropic noise propagation in diffusion tensor mri sampling schemes. *Magnetic Resonance in Medicine: An Official Journal of the International Society for Magnetic Resonance in Medicine*, 49(6):1143–1151, 2003.

[244] Aziz Hatim Poonawalla and Xiaohong Joe Zhou. Analytical error propagation in diffusion anisotropy calculations. *Journal of Magnetic Resonance Imaging*, 19(4):489–498, 2004.

[245] Catherine Lebel, Thomas Benner, and Christian Beaulieu. Six is enough? comparison of diffusion parameters measured using six or more diffusion-encoding gradient directions with deterministic tractography. *Magnetic resonance in medicine*, 68(2):474–483, 2012.

[246] Jose Soares, Paulo Marques, Victor Alves, and Nuno Sousa. A hitchhiker's guide to diffusion tensor imaging. *Frontiers in neuroscience*, 7:31, 2013.

[247] Moti Freiman, Stephan D Voss, Robert V Mulkern, Jeannette M Perez-Rossello, Michael J Callahan, and Simon K Warfield. In vivo assessment of optimal b-value range for perfusion-insensitive apparent diffusion coefficient imaging. *Medical physics*, 39(8):4832–4839, 2012.

[248] Christopher Kelly, Max Pietsch, Serena Counsell, and J-Donald Tournier. Transfer learning and convolutional neural net fusion for motion artefact detection. In *Proc. Intl. Soc. Mag. Reson. Med.*, pages 1–2, 2016.

[249] H. Zhang. Noddi matlab toolbox. `https://www.nitrc.org/frs/download.php/10193/Explore_DWI_Data_with_FSLview.pdf`, 2017.

[250] Mark Jenkinson and Stephen Smith. A global optimisation method for robust affine registration of brain images. *Medical image analysis*, 5(2):143–156, 2001.

[251] Douglas N Greve and Bruce Fischl. Accurate and robust brain image alignment using boundary-based registration. *Neuroimage*, 48(1):63–72, 2009.

[252] Mark Jenkinson, Peter Bannister, Michael Brady, and Stephen Smith. Improved optimization for the robust and accurate linear registration and motion correction of brain images. *Neuroimage*, 17(2):825–841, 2002.

[253] Francesco Grussu, Torben Schneider, Hui Zhang, Daniel C Alexander, and Claudia AM Wheeler-Kingshott. Neurite orientation dispersion and density imaging of the healthy cervical spinal cord in vivo. *Neuroimage*, 111:590–601, 2015.

[254] Siawoosh Mohammadi, Patrick Freund, Thorsten Feiweier, Armin Curt, and Nikolaus Weiskopf. The impact of post-processing on spinal cord diffusion tensor imaging. *Neuroimage*, 70:377–385, 2013.

[255] Stephen M Smith. Fast robust automated brain extraction. *Human brain mapping*, 17(3):143–155, 2002.

[256] H. Zhang. Noddi matlab toolbox. `http://mig.cs.ucl.ac.uk/index.php?n=Tutorial.NODDImatlab`, 2012.

[257] Alan C Evans, Andrew L Janke, D Louis Collins, and Sylvain Baillet. Brain templates and atlases. *Neuroimage*, 62(2):911–922, 2012.

[258] Vladimir Fonov, Alan C Evans, Kelly Botteron, C Robert Almli, Robert C McKinstry, D Louis Collins, Brain Development Cooperative Group, et al. Unbiased average age-appropriate atlases for pediatric studies. *Neuroimage*, 54(1):313–327, 2011.

[259] Uicheul Yoon, Vladimir S Fonov, Daniel Perusse, Alan C Evans, Brain Development Cooperative Group, et al. The effect of template choice on morphometric analysis of pediatric brain data. *Neuroimage*, 45(3):769–777, 2009.

[260] David Raffelt, J-Donald Tournier, Jurgen Fripp, Stuart Crozier, Alan Connelly, and Olivier Salvado. Symmetric diffeomorphic registration of fibre orientation distributions. *NeuroImage*, 56(3):1171–1180, 2011.

[261] Christopher G Schwarz, Robert I Reid, Jeffrey L Gunter, Matthew L Senjem, Scott A Przybelski, Samantha M Zuk, Jennifer L Whitwell, Prashanthi Vemuri, Keith A Josephs, Kejal Kantarci, et al. Improved dti registration allows voxel-based analysis that outperforms tract-based spatial statistics. *Neuroimage*, 94:65–78, 2014.

[262] Shiva Keihaninejad, Hui Zhang, Natalie S Ryan, Ian B Malone, Marc Modat, M Jorge Cardoso, David M Cash, Nick C Fox, and Sebastien Ourselin. An unbiased longitudinal analysis framework for tracking white matter changes using diffusion tensor imaging with application to alzheimer's disease. *Neuroimage*, 72:153–163, 2013.

[263] Hui Zhang, Paul A Yushkevich, Daniel C Alexander, and James C Gee. Deformable registration of diffusion tensor mr images with explicit orientation optimization. *Medical image analysis*, 10(5):764–785, 2006.

[264] Hui Zhang, Brian B Avants, Paul A Yushkevich, John H Woo, Sumei Wang, Leo F McCluskey, Lauren B Elman, Elias R Melhem, and James C Gee. High-dimensional spatial normalization of diffusion tensor images

improves the detection of white matter differences: an example study using amyotrophic lateral sclerosis. *IEEE transactions on medical imaging*, 26(11):1585–1597, 2007.

[265] Hui Zhang, Paul A Yushkevich, Daniel Rueckert, and James C Gee. A computational white matter atlas for aging with surface-based representation of fasciculi. In *International Workshop on Biomedical Image Registration*, pages 83–90. Springer, 2010.

[266] Christopher A Ross and Sarah J Tabrizi. Huntington's disease: from molecular pathogenesis to clinical treatment. *The Lancet Neurology*, 10(1):83–98, 2011.

[267] Elizabeth H Aylward, Peggy C Nopoulos, Christopher A Ross, Douglas R Langbehn, Ronald K Pierson, James A Mills, Hans J Johnson, Vincent A Magnotta, Andrew R Juhl, Jane S Paulsen, et al. Longitudinal change in regional brain volumes in prodromal huntington disease. *Journal of Neurology, Neurosurgery & Psychiatry*, 82(4):405–410, 2011.

[268] Nellie Georgiou-Karistianis, Rachael Scahill, Sarah J Tabrizi, Ferdinando Squitieri, and Elizabeth Aylward. Structural mri in huntington's disease and recommendations for its potential use in clinical trials. *Neuroscience & Biobehavioral Reviews*, 37(3):480–490, 2013.

[269] Sarah J Tabrizi, Ralf Reilmann, Raymund AC Roos, Alexandra Durr, Blair Leavitt, Gail Owen, Rebecca Jones, Hans Johnson, David Craufurd, Stephen L Hicks, et al. Potential endpoints for clinical trials in premanifest and early huntington's disease in the track-hd study: analysis of 24 month observational data. *The Lancet Neurology*, 11(1):42–53, 2012.

[270] Gavin P Winston, Caroline Micallef, Mark R Symms, Daniel C Alexander, John S Duncan, and Hui Zhang. Advanced diffusion imaging sequences could aid assessing patients with focal cortical dysplasia and epilepsy. *Epilepsy research*, 108(2):336–339, 2014.

[271] Catherine F Slattery, Jiaying Zhang, Ross W Paterson, Alexander JM Foulkes, Amelia Carton, Kirsty Macpherson, Laura Mancini, David L Thomas, Marc Modat, Nicolas Toussaint, et al. Apoe influences regional white-matter axonal density loss in alzheimer's disease. *Neurobiology of aging*, 57:8–17, 2017.

[272] Charlotte L Rae, Geoff Davies, Sarah N Garfinkel, Matt C Gabel, Nicholas G Dowell, Mara Cercignani, Anil K Seth, Kathryn E Greenwood, Nick Medford, and Hugo D Critchley. Deficits in neurite density underlie white matter structure abnormalities in first-episode psychosis. *Biological psychiatry*, 82(10):716–725, 2017.

[273] Koji Kamagata, Taku Hatano, Ayami Okuzumi, Yumiko Motoi, Osamu Abe, Keigo Shimoji, Kouhei Kamiya, Michimasa Suzuki, Masaaki Hori, Kanako K Kumamaru, et al. Neurite orientation dispersion and density imaging in the substantia nigra in idiopathic parkinson disease. *European radiology*, 26(8):2567–2577, 2016.

[274] Stefan Klöppel, Sarah Gregory, Elisa Scheller, Lora Minkova, Adeel Razi, Alexandra Durr, Raymund AC Roos, Blair R Leavitt, Marina Papoutsi, G Bernhard Landwehrmeyer, et al. Compensation in preclinical huntington's disease: evidence from the track-on hd study. *EBioMedicine*, 2(10):1420–1429, 2015.

[275] Karl Kieburtz, John B Penney, Peter Corno, Neal Ranen, Ira Shoulson, Andrew Feigin, Davi Abwender, J Timothy Greenarnyre, Donald Higgins, Frederick J Marshall, et al. Unified huntingtons disease rating scale: reliability and consistency. *Neurology*, 11(2):136–142, 2001.

[276] John B Penney, Jean-Paul Vonsattel, Marcy E Macdonald, James F Gusella, and Richard H Myers. Cag repeat number governs the development rate of pathology in huntington's disease. *Annals of neurology*, 41(5):689–692, 1997.

[277] Douglas R Langbehn, Ryan R Brinkman, Daniel Falush, Jane S Paulsen, and MR Hayden. A new model for prediction of the age of onset and penetrance for huntington's disease based on cag length. *Clinical genetics*, 65(4):267–277, 2004.

[278] Anderson M Winkler, Gerard R Ridgway, Matthew A Webster, Stephen M Smith, and Thomas E Nichols. Permutation inference for the general linear model. *Neuroimage*, 92:381–397, 2014.

[279] Stephen M Smith and Thomas E Nichols. Threshold-free cluster enhancement: addressing problems of smoothing, threshold dependence and localisation in cluster inference. *Neuroimage*, 44(1):83–98, 2009.

[280] Sarah Gregory, James H Cole, Ruth E Farmer, Elin M Rees, Raymund AC Roos, Reiner Sprengelmeyer, Alexandra Durr, Bernhard Landwehrmeyer, Hui Zhang, Rachael I Scahill, et al. Longitudinal diffusion tensor imaging shows progressive changes in white matter in huntingtons disease. *Journal of Huntington's disease*, 4(4):333–346, 2015.

[281] Susumu Mori, Kenichi Oishi, Hangyi Jiang, Li Jiang, Xin Li, Kazi Akhter, Kegang Hua, Andreia V Faria, Asif Mahmood, Roger Woods, et al. Stereotaxic white matter atlas based on diffusion tensor imaging in an icbm template. *Neuroimage*, 40(2):570–582, 2008.

[282] Marc Modat, Gerard R Ridgway, Zeike A Taylor, Manja Lehmann, Josephine Barnes, David J Hawkes, Nick C Fox, and Sébastien Ourselin. Fast free-form deformation using graphics processing units. *Computer methods and programs in biomedicine*, 98(3):278–284, 2010.

[283] Laurent R Gauthier, Bénédicte C Charrin, Maria Borrell-Pagès, Jim P Dompierre, Hélène Rangone, Fabrice P Cordelières, Jan De Mey, Marcy E MacDonald, Volkmar Leßmann, Sandrine Humbert, et al. Huntingtin controls neurotrophic support and survival of neurons by enhancing bdnf vesicular transport along microtubules. *Cell*, 118(1):127–138, 2004.

[284] Eugenia Trushina, Roy B Dyer, John D Badger, Daren Ure, Lars Eide, David D Tran, Brent T Vrieze, Valerie Legendre-Guillemin, Peter S McPherson, Bhaskar S Mandavilli, et al. Mutant huntingtin impairs axonal trafficking in mammalian neurons in vivo and in vitro. *Molecular and cellular biology*, 24(18):8195–8209, 2004.

[285] Hans-Peter Müller, Martin Gorges, Georg Grön, Jan Kassubek, G Bernhard Landwehrmeyer, Sigurd D Süßmuth, Robert Christian Wolf, and Michael Orth. Motor network structure and function are associated with motor performance in huntingtons disease. *Journal of neurology*, 263(3):539–549, 2016.

[286] Flor A Espinoza, Jessica A Turner, Victor M Vergara, Robyn L Miller, Eva Mennigen, Jingyu Liu, Maria B Misiura, Jennifer Ciarochi, Hans J Johnson, Jeffrey D Long, et al. Whole-brain connectivity in a large study of huntington's disease gene mutation carriers and healthy controls. *Brain connectivity*, 8(3):166–178, 2018.

[287] Peter McColgan, Adeel Razi, Sarah Gregory, Kiran K Seunarine, Alexandra Durr, Raymund AC Roos, Blair R Leavitt, Rachael I Scahill, Chris A Clark, Doug R Langbehn, et al. Structural and functional brain network correlates of depressive symptoms in premanifest huntington's disease. *Human brain mapping*, 38(6):2819–2829, 2017.

[288] Sarah Gregory, Jeffrey D Long, Stefan Klöppel, Adeel Razi, Elisa Scheller, Lora Minkova, Marina Papoutsi, James A Mills, Alexandra Durr, Blair R Leavitt, et al. Operationalizing compensation over time in neurodegenerative disease. *Brain*, 140(4):1158–1165, 2017.

[289] Dirk HJ Poot, J Arnold, Eric Achten, Marleen Verhoye, and Jan Sijbers. Optimal experimental design for diffusion kurtosis imaging. *IEEE transactions on medical imaging*, 29(3):819–829, 2010.

[290] J.H. Byrne and N. Dafny. Neuroanatomy online: An electronic laboratory for the neurosciences. `http://nba.uth.tmc.edu/neuroanatomy/`, 2014.

[291] Kaoru Okuizumi, Osamu Onodera, Hajime Tanaka, Hisashi Kobayashi, Shoji Tsuji, Hitoshi Takahashi, Kiyomitsu Oyanagi, Koji Seki, Masaharu Tanaka, Satoshi Naruse, et al. Apoe–ε4 and early–onset alzheimer's. *Nature genetics*, 7(1):10, 1994.

[292] Rik Ossenkoppele, Yolande AL Pijnenburg, David C Perry, Brendan I Cohn-Sheehy, Nienke ME Scheltens, Jacob W Vogel, Joel H Kramer, Annelies E van der Vlies, Renaud La Joie, Howard J Rosen, et al. The behavioural/dysexecutive variant of alzheimers disease: clinical, neuroimaging and pathological features. *Brain*, 138(9):2732–2749, 2015.

[293] Maria Luisa Gorno-Tempini, Argye E Hillis, Sandra Weintraub, Andrew Kertesz, Mario Mendez, SF et al Cappa, JM Ogar, JD Rohrer, S Black, BF Boeve, et al. Classification of primary progressive aphasia and its variants. *Neurology*, pages WNL–0b013e31821103e6, 2011.

[294] David F Tang-Wai, NR Graff-Radford, BF Boeve, DW Dickson, JE Parisi, R Crook, RJ Caselli, DS Knopman, and RC Petersen. Clinical, genetic, and neuropathologic characteristics of posterior cortical atrophy. *Neurology*, 63(7):1168–1174, 2004.

[295] Manja Lehmann, Pia M Ghosh, Cindee Madison, Robert Laforce Jr, Chiara Corbetta-Rastelli, Michael W Weiner, Michael D Greicius, William W Seeley, Maria L Gorno-Tempini, Howard J Rosen, et al. Diverging patterns of amyloid deposition and hypometabolism in clinical variants of probable alzheimers disease. *Brain*, 136(3):844–858, 2013.

[296] Rik Ossenkoppele, Brendan I Cohn-Sheehy, Renaud La Joie, Jacob W Vogel, Christiane Möller, Manja Lehmann, Bart NM van Berckel, William W Seeley, Yolande A Pijnenburg, Maria L Gorno-Tempini, et al. Atrophy patterns

in early clinical stages across distinct phenotypes of a lzheimer's disease. *Human brain mapping*, 36(11):4421–4437, 2015.

[297] Rik Ossenkoppele, Daniel R Schonhaut, Michael Schöll, Samuel N Lockhart, Nagehan Ayakta, Suzanne L Baker, James P ONeil, Mustafa Janabi, Andreas Lazaris, Averill Cantwell, et al. Tau pet patterns mirror clinical and neuroanatomical variability in alzheimers disease. *Brain*, 139(5):1551–1567, 2016.

[298] H Braak, E Braak, D Yilmazer, RAI De Vos, ENH Jansen, and J Bohl. Pattern of brain destruction in parkinson's and alzheimer's diseases. *Journal of neural transmission*, 103(4):455–490, 1996.

[299] Stephen E Rose, Fang Chen, Jonathan B Chalk, Fernando O Zelaya, Wendy E Strugnell, Mark Benson, James Semple, and David M Doddrell. Loss of connectivity in alzheimer's disease: an evaluation of white matter tract integrity with colour coded mr diffusion tensor imaging. *Journal of Neurology, Neurosurgery & Psychiatry*, 69(4):528–530, 2000.

[300] William W Seeley, Richard K Crawford, Juan Zhou, Bruce L Miller, and Michael D Greicius. Neurodegenerative diseases target large-scale human brain networks. *Neuron*, 62(1):42–52, 2009.

[301] Jason D Warren, Jonathan D Rohrer, Jonathan M Schott, Nick C Fox, John Hardy, and Martin N Rossor. Molecular nexopathies: a new paradigm of neurodegenerative disease. *Trends in neurosciences*, 36(10):561–569, 2013.

[302] Francesca Caso, Federica Agosta, Daniele Mattavelli, Raffaella Migliaccio, Elisa Canu, Giuseppe Magnani, Alessandra Marcone, Massimiliano Copetti, Monica Falautano, Giancarlo Comi, et al. White matter degeneration in atypical alzheimer disease. *Radiology*, 277(1):162–172, 2015.

[303] Chiara Cerami, Chiara Crespi, Pasquale Anthony Della Rosa, Alessandra Dodich, Alessandra Marcone, Giuseppe Magnani, Elisabetta Coppi, Andrea

Falini, Stefano F Cappa, and Daniela Perani. Brain changes within the visuo-spatial attentional network in posterior cortical atrophy. *Journal of Alzheimer's Disease*, 43(2):385–395, 2015.

[304] Ajay Madhavan, Christopher G Schwarz, Joseph R Duffy, Edythe A Strand, Mary M Machulda, Daniel A Drubach, Kejal Kantarci, Scott A Przybelski, Robert I Reid, Matthew L Senjem, et al. Characterizing white matter tract degeneration in syndromic variants of alzheimers disease: a diffusion tensor imaging study. *Journal of Alzheimer's Disease*, 49(3):633–643, 2016.

[305] V Heise, N Filippini, KP Ebmeier, and CE Mackay. The apoe 4 allele modulates brain white matter integrity in healthy adults. *Molecular psychiatry*, 16(9):908, 2011.

[306] Ian J Deary, Martha C Whiteman, Alison Pattie, John M Starr, Caroline Hayward, Alan F Wright, Andrew Carothers, and Lawrence J Whalley. Ageing: Cognitive change and the apoe 4 allele. *Nature*, 418(6901):932, 2002.

[307] Robert W Mahley, Karl H Weisgraber, and Yadong Huang. Apolipoprotein e: structure determines function, from atherosclerosis to alzheimer's disease to aids. *Journal of lipid research*, 50(Supplement):S183–S188, 2009.

[308] Robert W Mahley and Stanley C Rall Jr. Apolipoprotein e: far more than a lipid transport protein. *Annual review of genomics and human genetics*, 1(1):507–537, 2000.

[309] Guojun Bu. Apolipoprotein e and its receptors in alzheimer's disease: pathways, pathogenesis and therapy. *Nature Reviews Neuroscience*, 10(5):333, 2009.

[310] Robert W Mahley. Apolipoprotein e: cholesterol transport protein with expanding role in cell biology. *Science*, 240(4852):622–630, 1988.

[311] G Jackson Snipes and Ueli Suter. Cholesterol and myelin. In *Cholesterol*, pages 173–204. Springer, 1997.

[312] Xianlin Han. Potential mechanisms contributing to sulfatide depletion at the earliest clinically recognizable stage of alzheimers disease: a tale of shotgun lipidomics. *Journal of neurochemistry*, 103:171–179, 2007.

[313] Guy M McKhann, David S Knopman, Howard Chertkow, Bradley T Hyman, Clifford R Jack Jr, Claudia H Kawas, William E Klunk, Walter J Koroshetz, Jennifer J Manly, Richard Mayeux, et al. The diagnosis of dementia due to alzheimers disease: Recommendations from the national institute on aging-alzheimers association workgroups on diagnostic guidelines for alzheimer's disease. *Alzheimer's & dementia*, 7(3):263–269, 2011.

[314] Marshal F Folstein, Susan E Folstein, and Paul R McHugh. mini-mental state: a practical method for grading the cognitive state of patients for the clinician. *Journal of psychiatric research*, 12(3):189–198, 1975.

[315] JT Moroney, E Bagiella, DW Desmond, Vladimir C Hachinski, PK Mölsä, L Gustafson, A Brun, P Fischer, Timo Erkinjuntti, W Rosen, et al. Meta-analysis of the hachinski ischemic score in pathologically verified dementias. *Neurology*, 49(4):1096–1105, 1997.

[316] Psychological Corporation. Wechsler abbreviated scale of intelligence, 1999.

[317] Marianne Jackson and Elizabeth K Warrington. Arithmetic skills in patients with unilateral cerebral lesions. *Cortex*, 22(4):611–620, 1986.

[318] EK Warrington. Manual for the recognition memory test for words and faces. *Windsor, UK: NFER-Nelson*, 1984.

[319] EK Warrington and M James. The visual object and space perception battery. bury st edmunds: Thames valley test company.; 1991.

[320] DM Baxter and EK Warrington. Measuring dysgraphia: a graded-difficulty spelling test. *Behavioural Neurology*, 7(3-4):107–116, 1994.

[321] A Smith. The symbol-digit modalities test: a neuropsychologic test of learning and other cerebral disorders. learning disorders. edited by: Helmuth j. 1968.

[322] Ida Sue Baron. Delis-kaplan executive function system. *Child Neuropsychology*, 10(2):147–152, 2004.

[323] Susana Muñoz Maniega, Maria C Valdés Hernández, Jonathan D Clayden, Natalie A Royle, Catherine Murray, Zoe Morris, Benjamin S Aribisala, Alan J Gow, John M Starr, Mark E Bastin, et al. White matter hyperintensities and normal-appearing white matter integrity in the aging brain. *Neurobiology of aging*, 36(2):909–918, 2015.

[324] Robyn A Honea, Eric Vidoni, Amith Harsha, and Jeffrey M Burns. Impact of apoe on the healthy aging brain: a voxel-based mri and dti study. *Journal of Alzheimer's disease*, 18(3):553–564, 2009.

[325] Lars T Westlye, Ivar Reinvang, Helge Rootwelt, and Thomas Espeseth. Effects of apoe on brain white matter microstructure in healthy adults. *Neurology*, 79(19):1961–1969, 2012.

[326] Michael T Maloney, Laurie S Minamide, Andrew W Kinley, Judith A Boyle, and James R Bamburg. β-secretase-cleaved amyloid precursor protein accumulates at actin inclusions induced in neurons by stress or amyloid β: a feedforward mechanism for alzheimer's disease. *Journal of Neuroscience*, 25(49):11313–11321, 2005.

[327] Thomas G Beach, Sarah E Monsell, Leslie E Phillips, and Walter Kukull. Accuracy of the clinical diagnosis of alzheimer disease at national institute on aging alzheimer disease centers, 2005–2010. *Journal of neuropathology and experimental neurology*, 71(4):266–273, 2012.

[328] Lester I Binder, Anthony Frankfurter, and Lionel I Rebhun. The distribution of tau in the mammalian central nervous system. *The Journal of cell biology*, 101(4):1371–1378, 1985.

[329] Cyril Laurent, Luc Buée, and David Blum. Tau and neuroinflammation: What impact for alzheimer's disease and tauopathies? *Biomedical journal*, 2018.

[330] David N Drechsel, AA Hyman, Melanie H Cobb, and MW Kirschner. Modulation of the dynamic instability of tubulin assembly by the microtubule-associated protein tau. *Molecular biology of the cell*, 3(10):1141–1154, 1992.

[331] Murray D Weingarten, Arthur H Lockwood, Shu-Ying Hwo, and Marc W Kirschner. A protein factor essential for microtubule assembly. *Proceedings of the National Academy of Sciences*, 72(5):1858–1862, 1975.

[332] E-M Mandelkow, K Stamer, R Vogel, E Thies, and E Mandelkow. Clogging of axons by tau, inhibition of axonal traffic and starvation of synapses. *Neurobiology of aging*, 24(8):1079–1085, 2003.

[333] Julia Tsai, Jaime Grutzendler, Karen Duff, and Wen-Biao Gan. Fibrillar amyloid deposition leads to local synaptic abnormalities and breakage of neuronal branches. *Nature neuroscience*, 7(11):1181, 2004.

[334] Ina Tesseur, Jo Van Dorpe, Koen Bruynseels, Francisca Bronfman, Raf Sciot, Alfons Van Lommel, and Fred Van Leuven. Prominent axonopathy and disruption of axonal transport in transgenic mice expressing human apolipoprotein e4 in neurons of brain and spinal cord. *The American journal of pathology*, 157(5):1495–1510, 2000.

[335] Kurt Spittaels, Chris Van den Haute, JO Van Dorpe, Koen Bruynseels, Kris Vandezande, Isabelle Laenen, Hugo Geerts, Marc Mercken, Raf Sciot, Alfons Van Lommel, et al. Prominent axonopathy in the brain and spinal cord of transgenic mice overexpressing four-repeat human tau protein. *The American journal of pathology*, 155(6):2153–2165, 1999.

[336] Dennis J Selkoe. Alzheimer's disease is a synaptic failure. *Science*, 298(5594):789–791, 2002.

[337] Xiaoying Tang, Dominic Holland, Anders M Dale, Laurent Younes, Michael I Miller, and Alzheimer's Disease Neuroimaging Initiative. Shape abnormalities of subcortical and ventricular structures in mild cognitive impairment and alzheimer's disease: detecting, quantifying, and predicting. *Human brain mapping*, 35(8):3701–3725, 2014.

[338] Karla L Miller, Fidel Alfaro-Almagro, Neal K Bangerter, David L Thomas, Essa Yacoub, Junqian Xu, Andreas J Bartsch, Saad Jbabdi, Stamatios N Sotiropoulos, Jesper LR Andersson, et al. Multimodal population brain imaging in the uk biobank prospective epidemiological study. *Nature neuroscience*, 19(11):1523, 2016.

[339] David C Van Essen, Kamil Ugurbil, E Auerbach, D Barch, TEJ Behrens, R Bucholz, Acer Chang, Liyong Chen, Maurizio Corbetta, Sandra W Curtiss, et al. The human connectome project: a data acquisition perspective. *Neuroimage*, 62(4):2222–2231, 2012.

[340] Zhexing Liu, Yi Wang, Guido Gerig, Sylvain Gouttard, Ran Tao, Thomas Fletcher, and Martin Styner. Quality control of diffusion weighted images. In *Medical Imaging 2010: Advanced PACS-based Imaging Informatics and Therapeutic Applications*, volume 7628, page 76280J. International Society for Optics and Photonics, 2010.

[341] Ipek Oguz, Mahshid Farzinfar, Joy Matsui, Francois Budin, Zhexing Liu, Guido Gerig, Hans J Johnson, and Martin Andreas Styner. Dtiprep: quality control of diffusion-weighted images. *Frontiers in neuroinformatics*, 8:4, 2014.

[342] O Esteban, D Birman, M Schaer, OO Koyejo, RA Poldrack, and KJ Gorgolewski. Mriqc: Predicting quality in manual mri assessment protocols using no-reference image quality measures. biorxiv. *Retrieved February*, 27:2017, 2017.

[343] Fidel Alfaro-Almagro, Mark Jenkinson, Neal K Bangerter, Jesper LR Andersson, Ludovica Griffanti, Gwenaëlle Douaud, Stamatios N Sotiropoulos, Saad Jbabdi, Moises Hernandez-Fernandez, Emmanuel Vallee, et al. Image processing and quality control for the first 10,000 brain imaging datasets from uk biobank. *Neuroimage*, 166:400–424, 2018.

[344] Yann LeCun, Yoshua Bengio, and Geoffrey Hinton. Deep learning. *nature*, 521(7553):436, 2015.

[345] Mark S Graham, Ivana Drobnjak, and Hui Zhang. Realistic simulation of artefacts in diffusion mri for validating post-processing correction techniques. *NeuroImage*, 125:1079–1094, 2016.

[346] Mark S Graham, Ivana Drobnjak, and Hui Zhang. A supervised learning approach for diffusion mri quality control with minimal training data. *NeuroImage*, 2018.

[347] Emer J Hughes, Tobias Winchman, Francesco Padormo, Rui Teixeira, Julia Wurie, Maryanne Sharma, Matthew Fox, Jana Hutter, Lucilio Cordero-Grande, Anthony N Price, et al. A dedicated neonatal brain imaging system. *Magnetic resonance in medicine*, 78(2):794–804, 2017.

[348] Jesper LR Andersson and Stamatios N Sotiropoulos. An integrated approach to correction for off-resonance effects and subject movement in diffusion mr imaging. *Neuroimage*, 125:1063–1078, 2016.

[349] Ivana Drobnjak, David Gavaghan, Endre Süli, Joe Pitt-Francis, and Mark Jenkinson. Development of a functional magnetic resonance imaging simulator for modeling realistic rigid-body motion artifacts. *Magnetic Resonance in Medicine: An Official Journal of the International Society for Magnetic Resonance in Medicine*, 56(2):364–380, 2006.

[350] Ivana Drobnjak, Gaby S Pell, and Mark Jenkinson. Simulating the effects of time-varying magnetic fields with a realistic simulated scanner. *Magnetic resonance imaging*, 28(7):1014–1021, 2010.

[351] Alessandro Daducci, Erick J Canales-Rodríguez, Hui Zhang, Tim B Dyrby, Daniel C Alexander, and Jean-Philippe Thiran. Accelerated microstructure imaging via convex optimization (amico) from diffusion mri data. *NeuroImage*, 105:32–44, 2015.

[352] Hcp lifespan. `http://lifespan.humanconnectome.org/data/phase1a-pilot-parameters.html`, 2015.

[353] J Zhang, AUROBRATA Ghosh, DANIEL Alexander, and HUI Zhang. The lifespan trajectory of white matter microstructure detected by noddi. In *International Society for Magnetic Resonance in Medicine (ISMRM) 24th Scientific Meeting and Exhibition*, 2016.

[354] Simon R Cox, Stuart J Ritchie, Elliot M Tucker-Drob, David C Liewald, Saskia P Hagenaars, Gail Davies, Joanna M Wardlaw, Catharine R Gale, Mark E Bastin, and Ian J Deary. Ageing and brain white matter structure in 3,513 uk biobank participants. *Nature communications*, 7:13629, 2016.

[355] Daniel C Alexander, Darko Zikic, Jiaying Zhang, Hui Zhang, and Antonio Criminisi. Image quality transfer via random forest regression: applications in diffusion mri. In *International Conference on Medical Image Computing and Computer-Assisted Intervention*, pages 225–232. Springer, 2014.

[356] Daniel C Alexander, Darko Zikic, Aurobrata Ghosh, Ryutaro Tanno, Viktor Wottschel, Jiaying Zhang, Enrico Kaden, Tim B Dyrby, Stamatios N Sotiropoulos, Hui Zhang, et al. Image quality transfer and applications in diffusion mri. *Neuroimage*, 152:283–298, 2017.

[357] Dmitry S Novikov, Jens H Jensen, Joseph A Helpern, and Els Fieremans. Revealing mesoscopic structural universality with diffusion. *Proceedings of the National Academy of Sciences*, page 201316944, 2014.

[358] Yaniv Assaf and Yoram Cohen. Non-mono-exponential attenuation of water and n-acetyl aspartate signals due to diffusion in brain tissue. *Journal of Magnetic Resonance*, 131(1):69–85, 1998.

[359] Chris A Clark, Maj Hedehus, and Michael E Moseley. Diffusion time dependence of the apparent diffusion tensor in healthy human brain and white matter disease. *Magnetic Resonance in Medicine: An Official Journal of the International Society for Magnetic Resonance in Medicine*, 45(6):1126–1129, 2001.

[360] Lauren M Burcaw, Els Fieremans, and Dmitry S Novikov. Mesoscopic structure of neuronal tracts from time-dependent diffusion. *NeuroImage*, 114:18–37, 2015.

[361] Silvia De Santis, Derek K Jones, and Alard Roebroeck. Including diffusion time dependence in the extra-axonal space improves in vivo estimates of axonal diameter and density in human white matter. *NeuroImage*, 130:91–103, 2016.

[362] Els Fieremans, Lauren M Burcaw, Hong-Hsi Lee, Gregory Lemberskiy, Jelle Veraart, and Dmitry S Novikov. In vivo observation and biophysical interpretation of time-dependent diffusion in human white matter. *NeuroImage*, 129:414–427, 2016.

[363] Katsutoshi Murata Thorsten Feiweier Issei Fukunaga Akifumi Hagiwara Ryusuke Irie Christina Andica Tomoko Maekawa Saori Koshino Koji Kamagata Kanako Kunishima Kumamaru Michimasa Suzuki Akihiko Wada Masaaki Hori, Kouhei Kamiya and Shigeki Aoki. (ISMRM 2018) diffusion time dependence of NODDI in in vivo human white matter.

[364] Francesco Grussu, Andrada Ianuş, Carmen Tur, Ferran Prados, Torben Schneider, Enrico Kaden, Sébastien Ourselin, Ivana Drobnjak, Hui Zhang, Daniel C Alexander, et al. Relevance of time-dependence for clinically viable diffusion imaging of the spinal cord. *Magnetic Resonance in Medicine*.

[365] Alex Mackay, Kenneth Whittall, Julian Adler, David Li, Donald Paty, and Douglas Graeb. In vivo visualization of myelin water in brain by magnetic resonance. *Magnetic resonance in medicine*, 31(6):673–677, 1994.

[366] Aurobrata Ghosh, Daniel Alexander, and Hui Zhang. Crossing versus fanning: Model comparison using hcp data. In *Computational Diffusion MRI*, pages 159–169. Springer, 2016.

[367] Ai Wern Chung, Kiran K Seunarine, and Chris A Clark. Noddi reproducibility and variability with magnetic field strength: A comparison between 1.5 t and 3 t. *Human brain mapping*, 37(12):4550–4565, 2016.

[368] Maira Tariq, Torben Schneider, Daniel C Alexander, C Wheeler-Kingshot, and Hui Zhang. Scan-rescan reproducibility of neurite microstructure estimates using noddi. The British Machine Vision Association and Society for Pattern Recognition, 2012.

[369] Prasanna Parvathaneni, Vishwesh Nath, Justin A Blaber, Kurt G Schilling, Allison E Hainline, Ed Mojahed, Adam W Anderson, and Bennett A Landman. Empirical reproducibility, sensitivity, and optimization of acquisition protocol, for neurite orientation dispersion and density imaging using amico. *Magnetic resonance imaging*, 50:96–109, 2018.